# MINIMIZATION OF THE EFFECTS OF SECONDARY REACTIONS ON

# TURBINE FILM COOLING IN A FUEL RICH ENVIRONMENT

THESIS
JUNE 2014

Andrew T. Shewhart

AFIT-ENY-14-J-37

**DEPARTMENT OF THE AIR FORCE**
**AIR UNIVERSITY**

# AIR FORCE INSTITUTE OF TECHNOLOGY

**Wright-Patterson Air Force Base, Ohio**

AFIT-ENY-14-J-37

Minimization of the Effects of Secondary Reactions on Turbine Film Cooling in a Fuel

Rich Environment

THESIS

Presented to the Faculty

Department of Aeronautics and Astronautics

Graduate School of Engineering and Management

Air Force Institute of Technology

Air University

Air Education and Training Command

In Partial Fulfillment of the Requirements for the

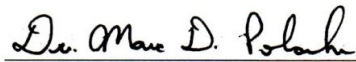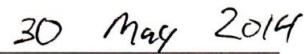Degree of Master of Science in Aeronautical Engineering

Andrew T. Shewhart, BS

June 2014

Minimization of the Effects of Secondary Reactions on Turbine Film Cooling in a Fuel
Rich Environment

Andrew T. Shewhart, BS

Approved:
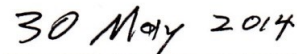
_____          _____
Dr. Marc D. Polanka (Chairman)                              30 May 2014
                                                                                    Date

_____          _____
Maj James Rutledge (Member)                                30 May 2014
                                                                                    Date

_____          _____
Capt David Liu (Member)                                      30 May 2014
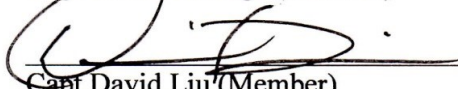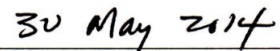                                                                                    Date

AFIT-ENY-14-J-37

## Abstract

The demand for increased thrust, higher engine efficiency, and reduced fuel consumption has increased the turbine inlet temperature and pressure in modern gas turbine engines. The outcome of these higher temperatures and pressures is the potential for unconsumed radical species to enter the turbine. Because modern cooling schemes for turbine blades involve injecting cool, oxygen rich air adjacent to the surface, the potential for reaction with radicals in the mainstream flow and augmented heat transfer to the blade arises. This study evaluated various configurations of multiple cylindrical rows of cooling holes in terms of both heat release and effective downstream cooling. It confirmed that a build-up of rows of coolant could be used to effectively protect the wall in a fuel-rich environment. It demonstrated slot and trench configurations to be effective in reducing the heat flux to the wall. Also, the Swirler and Two Row Upstream configurations were shown to highly increase radical consumption. Finally, this research developed infrared imaging as a technique for evaluating the wall temperature of the film cooled surface.

**Acknowledgments**

**Table of Contents**

# List of Figures

x

**List of Tables**

# List of Symbols

**English symbols**

| | | |
|---|---|---|
| $A$ | = | area ($m^2$) |
| $c_p$ | = | specific heat at constant pressure (J/kg K) |
| $d$ | = | diameter (m) |
| $Da$ | = | Damkohler number |
| $h$ | = | heat transfer coefficient ($W/m^2$ K) |
| $I$ | = | Momentum Ratio |
| $k$ | = | thermal conductivity ($W/m^2$ K); trip height (m) |
| $L$ | = | total length (m) |
| $M$ | = | blowing ratio |
| $\dot{m}$ | = | mass flow rate (g/min; g/s) |
| $MW$ | = | molecular weight (g/mol) |
| $Nu$ | = | Nusselt number |
| $P$ | = | pressure ($N/m^2$) |
| $q$ | = | heat transfer rate (W) |
| $q''$ | = | heat flux ($W/m^2$) |
| $R$ | = | universal gas constant (J/mol K) |
| $Re$ | = | Reynolds number |
| $t$ | = | thickness (m) |
| $T$ | = | temperature (K) |
| $U$ | = | velocity (m/s) |
| $X$ | = | streamwise location; distance (m) |
| $Y$ | = | direction normal to film cooled wall; distance (m) |
| $Z$ | = | spanwise location; distance (m) |

**Greek symbols**

| | | |
|---|---|---|
| $\alpha$ | = | injection angle (°) |
| $\varepsilon$ | = | emissivity |
| $\eta$ | = | film effectiveness |
| $\rho$ | = | density ($kg/m^3$) |
| $\sigma$ | = | Boltzmann constant (J/K) |
| $\tau_{chem}$ | = | characteristic chemical time (s) |
| $\tau_{flow}$ | = | characteristic flow time (s) |
| $\Phi$ | = | equivalence ratio |
| $\varphi$ | = | overall effectiveness |

**Subscripts**

| | | |
|---|---|---|
| *0* | = | *reference* |
| *∞* | = | *freestream; reactor exhaust stream* |
| *aw* | = | *adiabatic wall* |
| *c* | = | *coolant; convection* |
| *d* | = | *diameter* |
| *f* | = | *film* |
| *L* | = | *body length* |
| *r* | = | *radiation* |
| *ref* | = | *reference* |
| *s* | = | *surface* |
| *tr* | = | *transition* |
| *x* | = | *specific location* |

*Abbreviations*

| | | |
|---|---|---|
| *AFRL* | = | *Air Force Research Laboratory* |
| *SLPM* | = | *Standard Liters per Minute* |
| *UCC* | = | *Ultra-Compact Combustor* |
| *WA* | = | *Wall Absorption* |
| *WSR* | = | *Well Stirred Reactor* |

**Minimization of the Effects of Secondary Reactions on Turbine Film Cooling in a**

**Fuel Rich Environment**

## I. Introduction

### 1.1    Turbine Film Cooling

The demand for increased thrust, higher engine efficiency, and reduced fuel consumption has increased the turbine inlet temperature, $T_4$. Early on in the history of turbojet engines, the maximum allowed turbine inlet temperature, $T_{4max}$, was limited by the temperature where the turbine material would fail.  However, starting in 1960, cooling methods were introduced to turbine airfoils allowing for an increase in $T_{4max}$ above the failure temperature of the turbine material.  Early on these cooling methods were simple convective cooling schemes that cooled the internal side of the turbine airfoils with high-pressure air bled from the compressor.  In 1970, a new cooling technology was introduced where air was bled from the internal passages and exhausted it onto the surface of the airfoil through small holes drilled into the surface.  This technology was called film cooling and is still a subject of research today and implemented in modern turbine engines [1].  A representation of the history of the difference between turbine inlet temperature and blade material limits is shown in Figure 0.1.
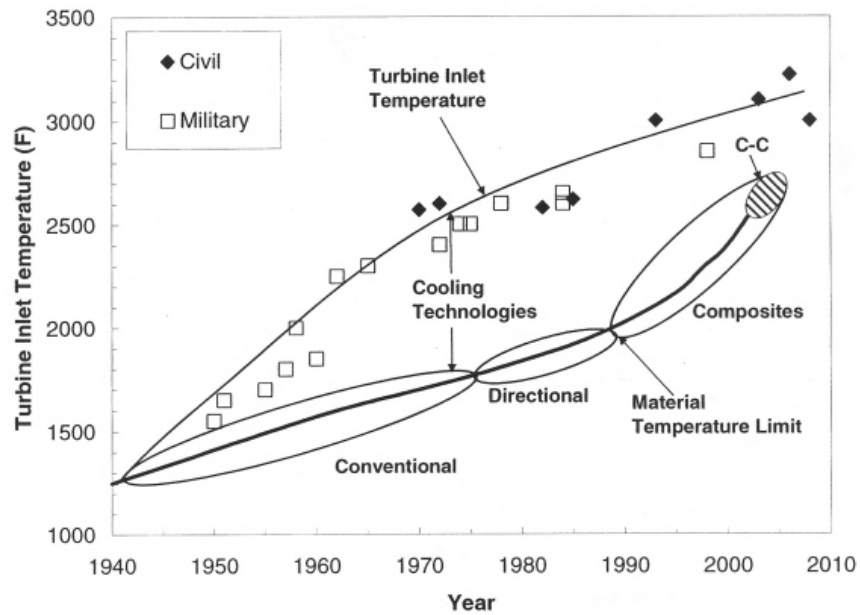
**Figure 0.1:** History of turbine inlet temperature and blade material limits [2]

A typical modern turbine blade with film cooling implemented is pictured in Figure 0.2. The film cooling injection holes are positioned along the surface of the blade and are arranged in rows and are angled to ensure an even spreading of attached film. A large number of cooling holes are typically clustered around the leading edge of the turbine blade. The clustering of film cooling holes at the leading edge is designed counteract the high heat transfer experienced due to the stagnation region. The desired result of film cooling is the reduction of heat flux to the wall through the creation of a thin layer of air attached to the surface.

**Figure 0.2:** Typical Modern Turbine Blade [6]

## 1.2     Potential for Heat Release in Film Cooling

Historically, gas turbine engines have operated at fuel-to-air ratios much less than stoichiometric. However, desire to increase thrust, engine efficiency, and reduce fuel consumption have pushed the turbine inlet temperature up as previous discussed. In order to obtain the higher temperatures required for increased specific thrust, engines are being operated at higher fuel-to-air ratios. As fuel-to-air ratio increases there is a greater risk of fuel-rich streaks and incomplete radicals entering the turbine and reacting with the film-cooling air. As a result, the air meant to cool the turbine may increase the heat flux to the airfoil due to the reactions.

Another challenge to turbine cooling comes from the increased turbine inlet temperatures. As temperatures and pressures increase, equilibrium concentrations of CO, OH, $H_2$, O, and other dissociated species are elevated [3][4]. Lukachko et al. [5] showed the overall combustor efficiency decreases and a greater portion of the potential fuel energy enters the turbine as temperature is increased at a constant pressure. Lukachko also estimated a maximum of 10% of fuel energy is available for secondary heat release

for a stoichiometric mixture. The energy stored in these highly energetic disassociated species has the potential to be released in the turbine where the cooler temperatures promote recombination. Reactions may also occur at coolant holes where the enhanced turbulence coupled with the additional, cool air promotes mixing and reactions to occur. This phenomenon is known as "Burning in the Turbine" and results in the reduction of the effectiveness of the cooling scheme and elevates the heat loads to the turbine components [6]. Additional heat loading on turbine components would severely reduce the part life or result in a catastrophic material failure.

## 1.3    Thesis Objectives

The main objective of this thesis was to evaluate various film cooling hole configuration downstream effectiveness with the goal of creating a film cooling scheme to efficiently operate in a fuel rich, turbine environment. To achieve this objective, film cooling configurations with varying goals were created. The first set of configurations tested aimed to reduce the heat flux to the wall through the build-up of a layer of attached coolant beneath a burning layer of coolant. The second set of configurations aimed to control the consumption of radicals with the aim at either concentrating the heat release to a known area or to displacing the flame away from the film cooled wall. Overall, a film cooling scheme with the ability to protect the wall in a fuel-rich environment or to reduce the freestream radicals so the wall could be protected further downstream was desired.

4

## II. Literature Review

Trends in current combustor designs continue to push towards stoichiometric operations for maximizing power and thermal efficiency. A subsequent problem that has arisen with this trend is the possibility of fuel rich species entering the turbine. This has led to the problem known as "Turbine Burning" as these species release energy when they react with the oxygen rich film cooling flow. This situation is further exasperated in the Ultra Compact Combustor design where the combustion process is fuel rich by design. This chapter will review the relevant background literature and nomenclature pertinent to this problem of secondary reactions in the turbine in a fuel rich environment with the goal of minimizing heat transfer to the wall. First, a discussion of traditional film cooling and heat transfer will be presented. This discussion will expand into techniques for measuring turbine cooling performance and the effects of various film cooling parameters and film cooling geometries on cooling performance. Then, the fundamentals of hydrocarbon combustion will be presented. Next, an overview of combustor liner design is presented. Finally, the background of film cooling in fuel rich environments and current evaluation metrics will be discussed.

### 2.1 Traditional Film Cooling

The overall goal of film cooling is to maintain the turbine blade temperature below its melting point through the expulsion of coolant air through discrete film cooling holes along the turbine blade. The coolant forms a thin protective layer of cool air between the

turbine blade and the hot freestream gases that exit the combustor. An effective cooling scheme will result in a lower wall temperature, $T_w$, and lower heat flux to the wall, $q''$.

In order to understand the physics of film cooling, knowledge of heat transfer is required. Heat transfer examines the exchange of thermal energy between physical systems and can be classified into three types; conduction, convection, and radiation. Convective heat transfer is the exchange of heat from one place to another due to fluid motion and is the primary form of heat transfer of this research. Convective heat transfer can be modeled by Newton's Law of Cooling defined as [7]

$$q'' = h(T_{ref} - T_w) \qquad (2.1)$$

where $h$ is the convective heat transfer coefficient, $T_w$ is the wall temperature, and $T_{ref}$ is the appropriately selected reference temperature.

Selecting the appropriate reference temperature in Equation 2.1 is not obvious because the film cooling process involves two temperatures, the coolant temperature $T_c$ and the freestream temperature $T_\infty$. The injected coolant air mixes with the hot freestream fluid to form a film of temperature, $T_f$, which varies with distance downstream, $z$, and has a value between the freestream temperature, $T_\infty$, and the coolant temperature, $T_c$. For the case of a film cooled surface, Equation 2.1 can be modified to represent the heat transfer with film cooling as [1]

$$q'' = h_f(T_f - T_w) \qquad (2.2)$$

where $h_f$ is the heat transfer coefficient with film cooling and $T_f$ is the temperature of the film.

Conductive heat transfer is the transfer of heat within a solid or between solid objects in thermal contact and occurs due to the interaction between hot, rapidly moving atoms or molecules with their neighboring atoms or molecules. For the 1-dimensional case, Fourier's Law of Conduction, seen in Equation 2.2, can be used to determine the value of heat flux, $q''$, and wall temperature

$$q'' = -k\frac{dT}{dx} \tag{2.3}$$

where $k$ is the thermal conductivity of the conducting material and $\frac{dT}{dx}$ is the temperature gradient [7].

Radiative heat transfer is the transfer of energy to or from a body through the means of emission or absorption of electromagnetic radiation. The heat flux emitted by a real surface is given by [7]

$$q''_{rad} = \sigma\varepsilon T_s^4 \tag{2.4}$$

where $\sigma$ is the Stefan-Boltzmann constant ($\sigma = 5.67 \times 10^{-8}$ W/m$^2 \times$ K$^4$), $T_s$ is the absolute temperature ($K$) of the surface, and $\varepsilon$ is the emissivity of the surface. Emissivity values range $0 \leq \varepsilon \leq 1$ and provides a measure of how efficiently a surface emits energy relative to a black body. A black body is an ideal surface that absorbs all incident radiation and emits the maximum possible energy for a specific temperature and thus it has an emissivity of one. The net heat flux from an opaque surface can be expressed as

$$q''_{rad,net} = \sigma\varepsilon T_s^4 - \sigma\alpha T_{sur}^4 \tag{2.5}$$

where α is the absorptivity and $T_{sur}$ is the absolute temperature of the surroundings (K). This expression provides the difference between thermal energy released and absorbed due to radiation.

### 2.1.1    Film Cooling Effectiveness Parameters

One important driving variable for predicting the temperature of an airfoil is the adiabatic wall temperature, $T_{aw}$, which is representative of the wall temperature when the wall is adiabatic. $T_o$ generalize the adiabatic wall temperature for comparison between experiments, the value of $T_{aw}$ is reported through a non-dimensional film effectiveness or adiabatic effectiveness defined [1] as

$$\eta = \frac{T_\infty - T_{aw}}{T_\infty - T_{c,e}} \tag{2.6}$$

where $T_{c,e}$ is the temperature of the coolant at the exit of the cooling hole. As the adiabatic wall temperature approaches the film coolant temperature, the adiabatic effectiveness approaches unity which indicates a more effective cooling scheme. Most literature that characterizes the performance of film cooling use adiabatic effectiveness but there are some challenges in accurately measuring this parameter. The measurement of $T_{aw}$ is difficult because many experiments are unable achieve a perfectly adiabatic wall. This is particularly problematic for measurements at high temperatures as metals have high conductivities resulting in highly non-adiabatic surfaces.

The overall goal of cooling turbine blades is to keep the wall temperature of the blades below a critical temperature required to maintain the integrity of the turbine blade.

8

By non-dimensionalizing $T_w$, another effectiveness parameter called the overall effectiveness can be defined as [1]

$$\phi = \frac{T_\infty - T_w}{T_\infty - T_{c,i}} \tag{2.7}$$

where $T_{c,i}$ is the coolant temperature before the coolant enters the film-cooling holes. This parameter takes into account both film cooling and internal cooling as $T_w$ is a function of both.

Reducing the heat flux to the turbine walls is essential to maintaining the turbine wall temperature below its critical value. Quantification of Net Heat Flux Reduction (NHFR) achieved can give insight to the effectiveness of the film cooling scheme. NHFR is defined as:

$$\Delta q_r'' = 1 - \frac{q_f''}{q_0''} \tag{2.8}$$

where $q_f''$ and $q_0''$ represent the heat flux to the wall with and without film cooling. This parameter describes the difference between the heat flux with and without film cooling and indicates whether or not the cooling scheme is protecting the surface. A positive value indicates the filmed cooled surface has reduced heat flux compared to the surface with no cooling. Conversely, a negative value indicates that the film cooling adversely impacted the heat flux to the wall and that it would be more beneficial to not apply film cooling at all.

### 2.1.2 Cooling Characterization Parameters

Many factors affect the cooling effectiveness including mass flux ratio, density ratio, and momentum flux ratio. These scaling parameters can be used to match engine-like conditions. Film cooling in gas turbine engines is characterized by high freestream to coolant temperature differences. This results in a coolant-to-freestream density ratio of approximately two. Density ratio is defined as

$$DR = \frac{\rho_c}{\rho_\infty} \tag{2.9}$$

where $\rho_c$ is the density of the coolant and $\rho_\infty$ is the density of the freestream. Density ratio is a key parameter to match when trying to model engine conditions. However, density ratio is difficult to simulate in many experimental facilities.

Matching performance results to engine conditions can be done by matching the blowing ratio, $M$, or the momentum flux ratio $I$ as well. The mass flux ratio or blowing ratio, defined in Equation 2.10, is a commonly used relationship that describes the properties of the coolant fluid relative to the freestream fluid.

$$M = \frac{\rho_c u_c}{\rho_\infty u_\infty} = \frac{A_\infty \dot{m}_c}{A_c \dot{m}_\infty} \tag{2.10}$$

In Equation 2.10, $A_c$ and $A_\infty$ are the areas through which the coolant and freestream flow, $\dot{m}_\infty$ is the freestream mass flow rate, and $\dot{m}_c$ is the coolant mass flow rate. Thus, $M$ only requires knowledge of the mass flow and areas of the freestream and coolant flows making the calculation of $M$ simple.

The momentum flux ratio scales the interaction of the mainstream with the exiting coolant jets. The mainstream impacts the cooling flow jet causing the coolant jet to turn towards the wall. If the coolant jet is not sufficiently turned the coolant flow will separate from the wall and provide very little cooling to the surface. So momentum ratio scales the jet separation or penetration depth of the jet. Momentum ratio, $I$, is defined as

$$I = \frac{\rho_c u_c^2}{\rho_\infty u_\infty^2} \tag{2.11}$$

Baldauf et al. [8] confirmed that the momentum ratio scaled the adiabatic effectiveness profile in near hole regions following a row of cylindrical holes.

### 2.1.3 Effect of Film Cooling Geometry

Over the long history of film cooling, researchers have investigated various methods to maximize film cooling effectiveness while minimizing coolant requirements. While the flow characterization parameters have an effect on the effectiveness of a cooling scheme, the parameters themselves are meaningless with defining a film cooling geometry. This section will review the benefits and disadvantages of cylindrical hole, fan-shaped hole, slot, and trench cooling geometries.

#### 2.1.3.1 Cylindrical Holes

Bogard and Thole [1] discuss the effects of hole spacing or pitch on the performance of a film cooling scheme. They conclude that as the hole spacing is decreased, there is a greater coverage of the coolant. For a given mass flow rate per hole, a decreasing hole spacing results in increased mass flow per unit span. As a result, the largest hole spacing that still fulfills the cooling requirements is desired to minimize the

11

amount of mass flow required. Typical hole spacing is within the range of 3-8 cooling hole diameters.

Baldauf et al. [8]examined the effects of blowing ratio on adiabatic effectiveness downstream of a cooling hole at incident angle of 30°, shown in Figure 0.1. For low values of M, η peaks very close to the hole and decays with downstream distance. As blowing ratio increases, the maximum value of η moves farther downstream and the effect of the coolant can be seen further downstream. Also as blowing ratio increases, the magnitude of η immediately downstream of the hole decrease and can be attributed to the jet separating from the surface immediately downstream of the hole and reattaching further downstream.
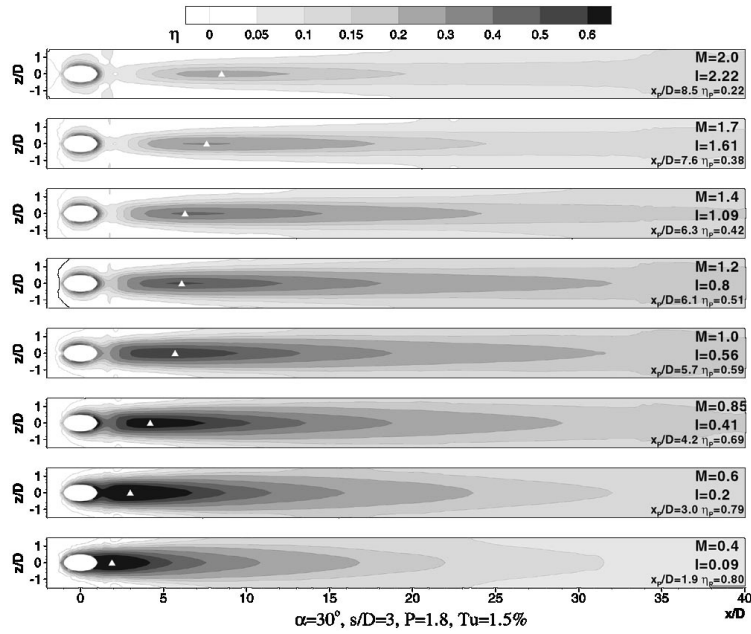


**Figure 0.1:** Effect of blowing ratio on local film cooling effectiveness [8]

Baldauf et al. also examined the effects of injection angle on downstream effectiveness. They compared the downstream effectiveness of a 30˚ injection angle from the streamwise coordinate with a normal set of coolant holes. Their results are shown in Figure 0.2 with the injection angle of 30˚ at the top and the normal coolant holes at the bottom. At low blowing ratios, it was shown that the angled holes achieved higher adiabatic effectiveness across a larger area than the normal holes. At high blowing ratios, however, both injection angles showed minimal downstream effectiveness. The angled holes also showed no effectiveness in the region next to the hole but a region of higher effectiveness further downstream indicating the flow separating from the wall.
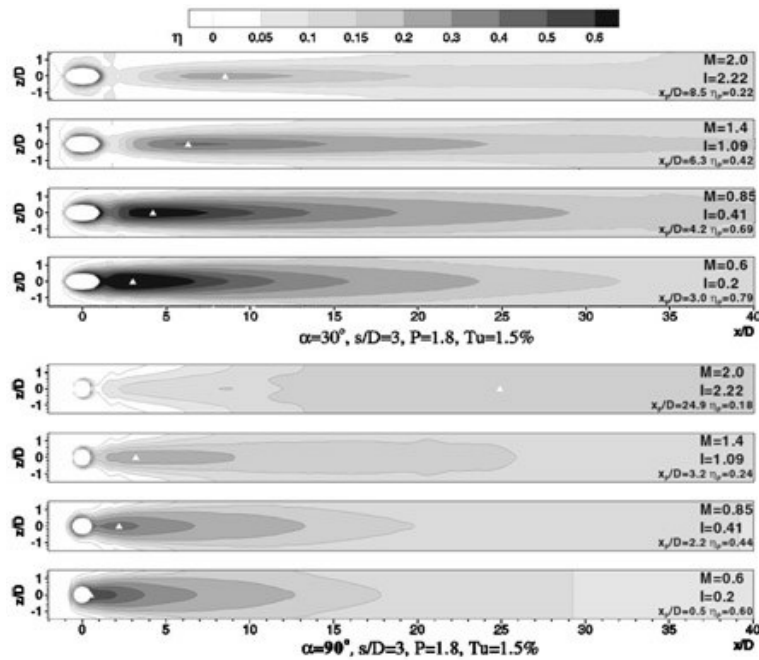


**Figure 0.2:** Effect of Injection Angle on adiabatic effectiveness [8]

13

A study by Oguntade et al. [9] analytically examined the effects of varying injection angle on adiabatic effectiveness for effusion cooling schemes. The paper examined injection angles of 30˚ (co-flow), 90˚ (normal), and 150˚ (counter-flow) from the streamwise direction. Their results on the effect of injection angle on the adiabatic effectiveness can be seen in Figure 0.3. The normal holes are labeled E, the co-flow holes are labeled E*, and the counter-flow holes are labeled E**. From the figure it can be seen the counter-flow holes displays significantly better adiabatic effectiveness and jet spreading than the normal and co-flow cases. As mass flow rate increased, the counter-flow showed increased η. Increasing mass flow rate on the normal and co-flow configurations, however, caused separation and a decreased η.
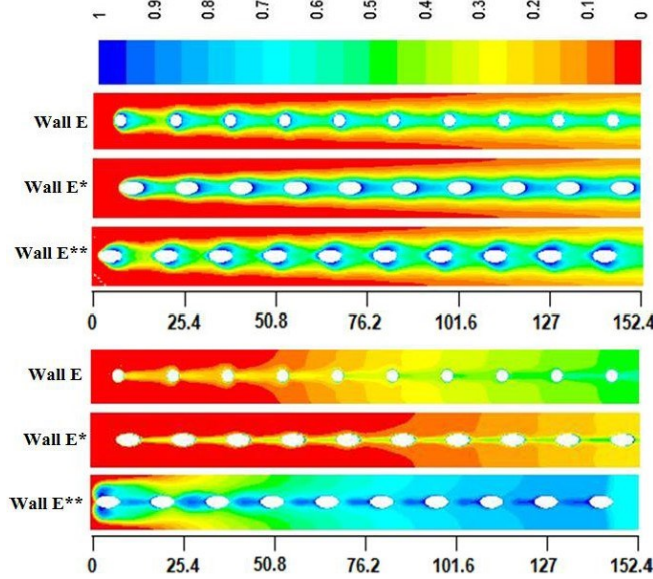


**Figure 0.3:** Contours of η for cylindrical holes at various injection angles: E – normal, E* - co-flow, E** - Counter-flow; M = 0.49, M = 2.47 [9]

14

Another result found by Oguntade et al. was the formation of counter rotating vortex pairs (CRVP) on the normal and co-flow cases that are similar to the vortex pairs that would shed from a cylinder in crossflow. Figure 0.4 shows the downstream vortex structures of all three cases. The CRVPs from the normal and co-flow cases have the undesired effect of sweeping hot core flow toward the wall. This results in the reduced spreading and adiabatic effectiveness in the normal and co-flow cases as shown in Figure 2.3.
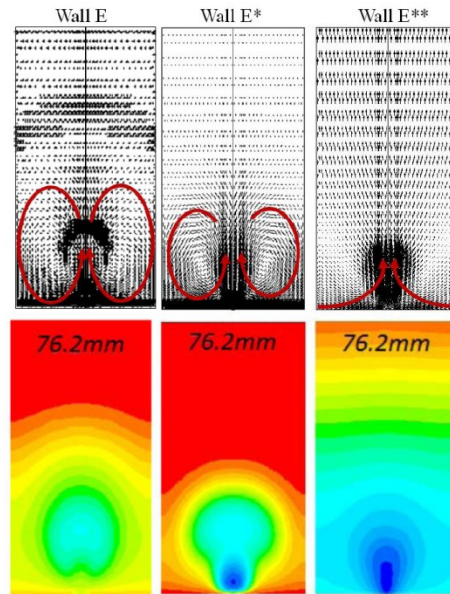


**Figure 0.4:** Oguntade downstream vortex structure and temperature penetration: E – normal, E* - co-flow, E**- counter-flow [9]

Conversely to the normal and co-flow, the counter-flow prevented the formation of the CRVPs. As seen from Figure 0.4, the upstream injection has a high degree of mixing and flow penetration. The high mixing, penetration, and spread rate of the

counter-flow injection angle make the counter-flow case a promising configuration for

local consumption of radicals.

### 2.1.3.2 Shaped Holes

Shaped coolant holes offer improved film cooling performance compared to

cylindrical holes. Shaped holes improve on the deficiencies of cylindrical holes by

expanding the ejection area and decreasing the exit velocity of the fluid.  This allows for

more mass flow to be passed through the hole while avoiding separation.   Two examples

of shaped holes are shown Figure 0.5[10].
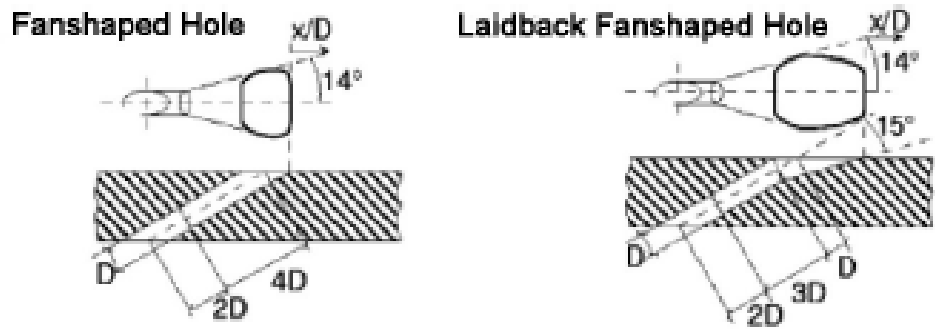


**Figure 0.5:** Schematic of typical shaped hole schemes [10]

Saumweber et al. [10] examined the effectiveness of the fan shaped hole

compared to that of a cylindrical hole.  Saumweber examined streamwise oriented holes

with an injection angle of 30˚ and a hole spacing of 4D.  His results are presented in

Figure 0.6 and show spatially averaged adiabatic effectiveness (averaged from $X/D = 2$ to

22) plotted against blowing ratio ranging from M = 0.5 to 2.5.  For the entire range of

blowing ratios, the fan shaped holes showed greater film effectiveness than the

16

cylindrical holes. With increasing blowing ratio, the shaped holes showed increasing film effectiveness, whereas the cylindrical holes show a drop in averaged adiabatic effectiveness. This decreasing effectiveness of the cylindrical holes is due to the coolant jet separating from the wall. This indicates that the fan shaped hole is effective in preventing coolant jet separation. Saumweber also examined the laidback fan shaped holes and found similar results to the fan shaped holes indicating the additional streamwise expansion of the hole provided no additional benefit.
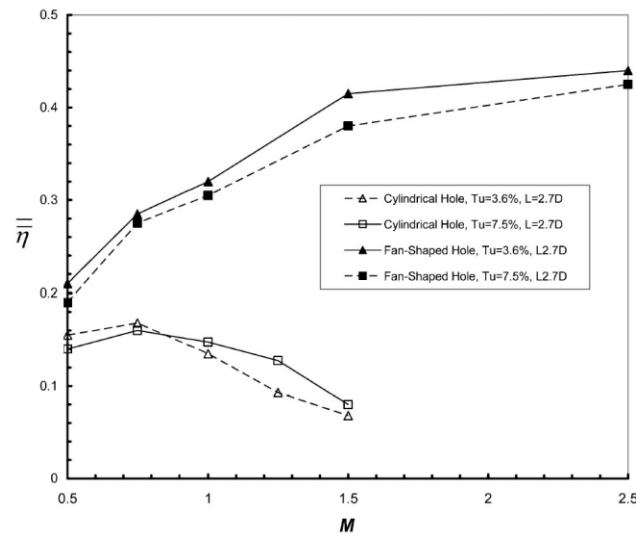


**Figure 0.6:** Comparison of spatially averaged film effectiveness of shaped holes and cylindrical holes for and varied blowing ratios [10]

### 2.1.3.3 Slot

A major challenge to discrete film cooling is achieving a well distributed layer of coolant that protects the entire surface. Slot cooling is considered to be the optimal configuration for providing a laterally even distribution of coolant. Hartnett et. al. [11]

examined the slot and showed that for nearly all cases a large continuous slot yields higher film cooling effectiveness levels over a larger area than that achieved by discrete cooling holes. Additionally, slot cooling was shown to not be prone to separation due to its large ejection area and low exit velocity.

One of the major drawbacks to slot cooling lies with the size of the slot itself. The large slot geometry leaves the component to be cooled structurally unstable. Under modern engine temperatures and pressures, the structurally instabilities of the slot could cause it to fail and ingest hot gases instead of expelling coolant. Another drawback of the large slot area is the large mass flow required for a given pressure drop through the channel. These drawbacks make the slot impractical for use in modern gas turbine engines.

### 2.1.3.4 Trench

The trench geometry was proposed as a means to benefit from the advantages of a slot configuration while minimizing its downsides. The geometry consists of discrete, angled cylindrical holes embedded in a trench. The height of the trench and angle of the cylindrical hole is designed such that a portion of the flow exiting the cylindrical hole impacts the trench wall. Bunker [12] postulated that the flow impacting the downstream trench wall acted to spread the coolant spanwise within the trench before exiting onto the surface as depicted in Figure 2.7. It was also suggested that the vortices created through this lateral spreading process may help counteract the vortices created by typical discrete film cooling in cross flow.

18
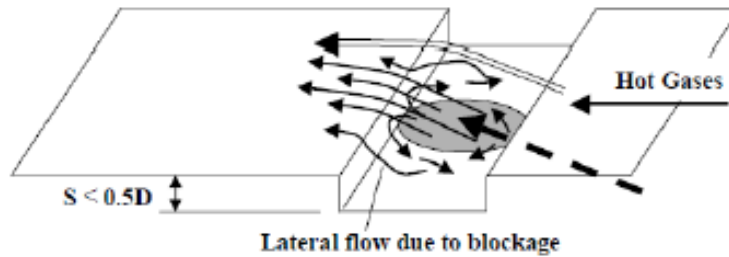
**Figure 0.7:** Lateral spreading of trench cooling [12]

Bunker [12] examined the effect of trenches streamwise length on cooling effectiveness. His data showed that cooling effectiveness was optimized when the width was as small as possible to maximum the lateral spreading of the cooling. Bunker [12] also examined the effects of blowing ratio on the performance of the trench. He varied blowing ratio from 1 to 4 and notice only small increases in adiabatic effectiveness with increasing blowing ratio. This indicates that the trench was not sensitive to blowing ratio and likely the coolant remained attached to the wall for this range of blowing ratios.

## 2.2    Combustor Liners

As turbines begin to experience reacting flows, a study of combustor liners that operate in a similar environment is beneficial. Mellor et al. [13] examined the heat transfer for a typical combustor liner as shown in Figure 2.8. They show that a combustor liner must mitigate both convective heat transfer to the wall and radiative heating from the flame. A turbine exposed to reacting flows would be required to mitigate both of these heat sources as well. To reduce the convective heat transfer to the

wall, modern combustors employ effusion cooling to produce a film of cool air above the

wall.  To remove heat from the walls, combustor liners utilize cold side convective

cooling and cold-side radiative cooling to the engine case.
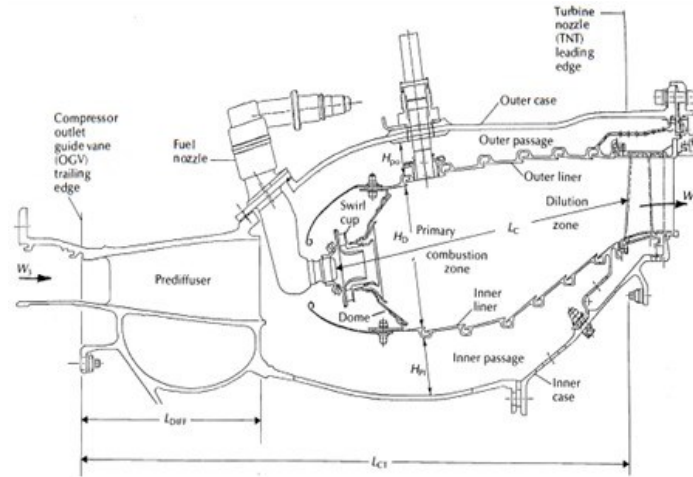


**Figure 0.8:** Typical Combustor: GE CF6-80C [13]

Mongia [14] discussed several forms of cooling commonly used in combustor

liners.  Combustor liners consist of an axial stack of joined panels with an offset at the

end of each panel where coolant is injected through a slot.  Coolant is injected through

this slot to protect the wall further downstream.   Typically, the slot injection impinged

on the upstream panel creating a stagnation point.  The stagnation point creates a very

high convective heat transfer coefficient providing additional cooling to the wall.

Mongia illustrates two different impingement cooling designs in Figure 2.9.
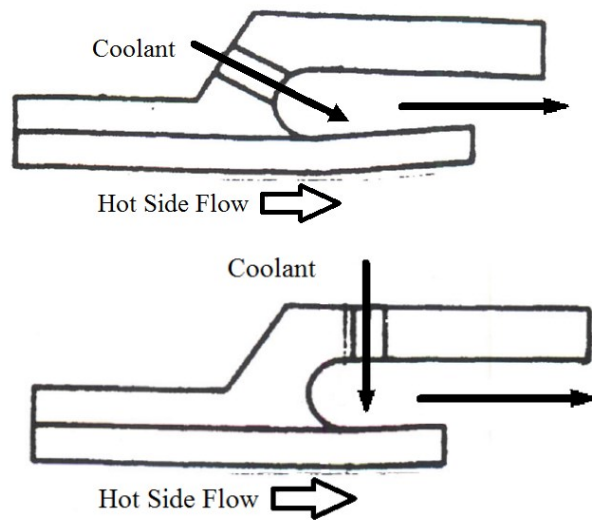
**Figure 0.9:** Impingent Cooling Arrangements [14]

More recent combustor liner research has focused on full coverage film cooling, or effusion cooling, which implements a large number of holes along the combustor liner. In this design, the wall temperature is lowered through film cooling and heat is removed by the passage of the coolant through the holes. Studies such as Andrews et al. [15] and Kakade et al. [16] examined the overall effectiveness for full coverage discrete hole cooling. Andrews found that increasing the number of holes increased the cooling effectiveness by creating a full film of coolant along the wall. This film would serve to buffer the reactions occurring in the combustor core away from the wall. With this in mind, various configurations of multiple rows of cylindrical holes were developed and tested as discussed in Section 3.4.

In their study, Kakade et al. [16] focused on experimentally characterizing the effects of freestream turbulence on the adiabatic effectiveness of an effusion cooling scheme subjected to different freestream turbulence levels. Their research examined cylindrical holes angled at 20˚ for blowing ratios ranging from 0.47 to 2.0 and turbulence intensities of 4% and 22%. The center of the first row of holes was taken as the origin (*X/D* = 0) and the last row is at *X/D* ~35. Figure 2.10 shows theirs results of spanwise average adiabatic effectiveness as a function of axial distance. For all blowing ratios, the general trend was increasing adiabatic effectiveness in the streamwise direction. For M = 0.47, the freestream turbulence showed little effect on the adiabatic effectiveness with the region of the effusion cooling holes. However, downstream of the last row of cooling the effectiveness of the high freestream turbulence case decayed more rapidly. For M = 0.7 to 1.5, the average adiabatic effectiveness decreased with increasing blowing ratio and the higher turbulence intensity results in higher averaged effectiveness.
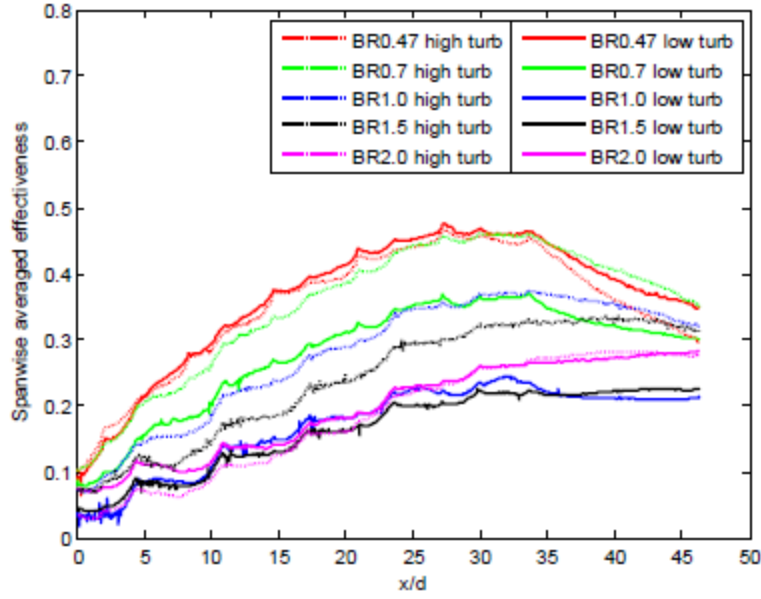
**Figure 0.10:** Kakade effusion cooling adiabatic effectiveness [16]

## 2.3   Hydrocarbon Combustion

The combustion of hydrocarbons is used to produce the energy required within turbine engines.  The understanding of the fundamentals of hydrocarbon combustion will allow for evaluation of the expected freestream temperatures and equilibrium species that enter into the turbine.  The ideal global reaction for the stoichiometric combustion of a general hydrocarbon in the form $C_xH_y$ can be defined as [17]

$$C_X H_Y + \left(x + \frac{y}{4}\right)O_2 + 3.76\left(x + \frac{y}{4}\right)N_2 \rightarrow xCO_2 + \frac{Y}{2}H_2O + 3.76\left(x + \frac{y}{4}\right)N_2 \quad (2.11)$$
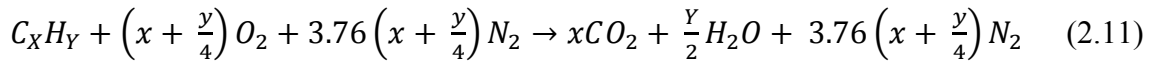
This model does not replicate the true combustion process or the equilibrium products.  For a closed, isothermal system, the equilibrium products can be determined by the minimization of Gibbs Free Energy.  Computational tools like CHEMKIN can be

23

used to calculate combustion products and heat release based on carious flow conditions,

fuel type, and equivalence ratio. The fuel-to-air ratio at stoichiometric conditions can be

determined from the moles of fuel and air. As an example, the stoichiometric fuel-to-air

ratio for propane was calculated below:

$$\frac{\dot{m}_{fuel}}{\dot{m}_{air}} = \frac{1 \times MW_{C_3H_8}}{5 \times (4.76 \times MW_{air})} = 0.06395 \tag{2.12}$$

The equivalence ratio, defined in Equation 2.13, is the ratio between the fuel-to-

air ratio at a specific condition with the fuel-to-air ratio at the stoichiometric condition.

This defines an equivalence ratio less than one as lean, greater than one as rich, and equal

to one as stoichiometric. Equivalence ratio highly influences the freestream temperature,

species composition, heat release, and much more of a flow making it an important

parameter to keep to track.

$$\Phi = \frac{\left(\dot{m}_{fuel}/\dot{m}_{air}\right)}{\left(\dot{m}_{fuel}/\dot{m}_{air}\right)_{stoich}} \tag{2.13}$$

## 2.4    Reactive Film Cooling

Maximizing the thrust-to-weight ratio in turbine engines has been a major design

challenge of past and current turbine research. Typically, this challenge was

accomplished through reduction of system losses and by use of thrust improving

24

techniques. However, recent research has pushed to increase the thrust-to-weight ratio by decreasing the weight of engine components. The high-g Ultra Compact Combustor (UCC) is one method to reduce the weight of the engine. The UCC utilizes the circumferential direction to obtain the necessary residence time thus shorting the axial distance compared to a typical axial combustor setup [18], as shown in Figure 2.11.
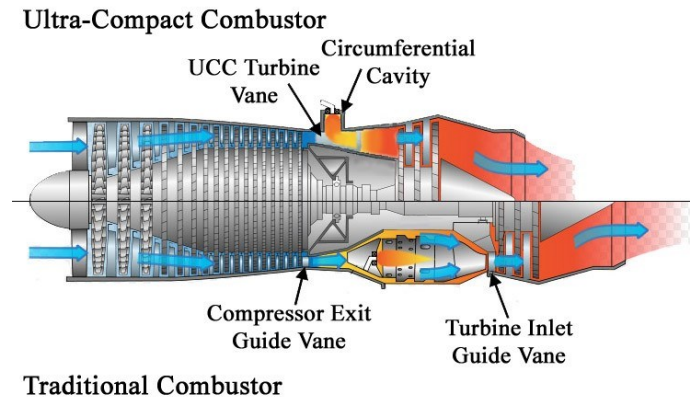


**Figure 0.11:** UCC setup (above) compared to traditional combustor setup (below) [19]

Fuel and air are brought into the cavity at an angle, creating a tangential velocity that drives the fuel rich, high-g combustion around the cavity in the circumferential direction around the core flow. As combustion progresses, a density gradient is formed in the cavity which allows the lighter combustion components to migrate inward to the core flow. Since the UCC burns rich, unconsumed energetic radicals leave the UCC section and proceed into the turbine. At turbine conditions with energetic radicals present, the oxygen-rich film coolant reacts quickly with the unconsumed radicals which results in increased heat transfer to the turbine blade. This increased heat transfer to the turbine

blades can cause shorter turbine blade life or complete component failure. In order to practically implement the UCC, a solution to the problem of reactive film cooling must be found.

Besides applications such as the UCC, there are scenarios where fuel radicals could enter the turbine in current turbine engine technologies. Lukachko et al. [5] examined the effects of pressure and temperature on the equilibrium concentrations of various common species. As temperatures and pressures increase, equilibrium concentrations of CO, OH, $H_2$, O, and other dissociated species are elevated [5][19]. Lukachko et al. showed that as temperature increased at a constant pressure, the overall combustor efficiency decreases and a greater portion of the potential fuel energy enters the turbine, as shown in Figure 2.12. As fuel-air ratios increase and efficiency decreases, the probability of finding fuel-rich streaks in the turbine in attrition to the additional concentration of energetic species increases. They also estimated that a maximum of 10% of fuel energy may be available for secondary heat release for a stoichiometric mixture of fuel and air. The energy stored in these highly energetic disassociated species has the potential to be released in the turbine where the cooler temperatures promote recombination.

26
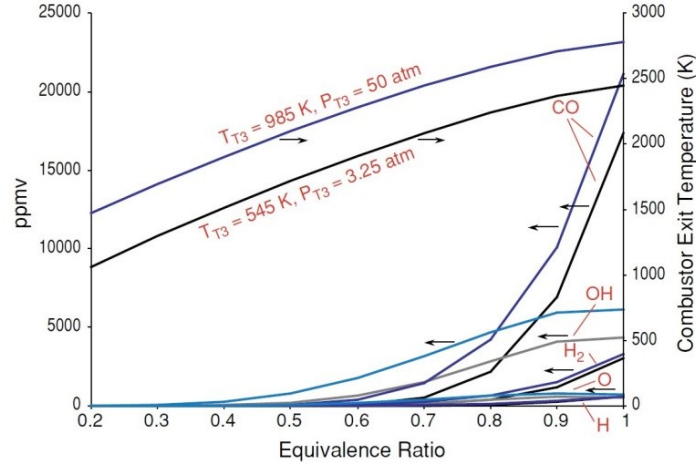
**Figure 0.12:** Equilibrium composition with increasing pressure and Φ

Early study of the effects of reactive film cooling began with Kirk et al. [4] and
their shock tube experiment which examined two sets of 35° film cooling holes that could
be supplied either air or nitrogen. They examined the effects of blowing ratio and
Damköhler number on the increase in surface heat flux due to secondary reactions.
Damköhler number describes the interaction between combustion and turbulent processes
and is defined as

$$Da = \frac{\tau_{flow}}{\tau_{chem}} = \frac{l_0/u'_{rms}}{\delta_L/S_L} \tag{2.14}$$

where $\tau_{flow}$ and $\tau_{chem}$ are characteristic flow and chemical times respectively. The integral
length scale, $l_0$, is the characteristic length of the largest eddies in the flow and the $u'_{rms}$ is
the root mean square of the turbulent component of velocity. $S_L$ and $\delta_L$ represent the
flame speed and thickness of a flame in a premixed laminar flow. For larger Da, the

27

turbulent process dominates and can influence the flame structure and increase the rate of reaction. This makes Da a good parameter to characterize reactive film cooling. Kirk et al. concluded that the impact of secondary reactions was a function of *Da*, heat release potential, and blowing ratio. The highest increase in heat flux augmentation they found occurred at the highest Da and potential heat release which resulted in a 30% increase in heat flux over the non-reactive cooling case. In summary, Kirk et al. identified the potential of film cooling to create secondary reactions when radicals are present and they presented a method for exploring and scaling the impacts of these secondary reactions on a film cooled flat plate.

Kirk et al. also performed a CFD simulation on reactive film cooling [4]. Their results are shown in Figure 2.13 and show a comparison between reactive and non-reactive film cooling for an attached and for a separated jet. Case 1a and 1b show the results for an attached jet. In the reacting case, the cooling jet produces a layer of relatively cool flow underneath a layer high temperature reacting flow for a short distance. As the coolant proceeds further downstream the high temperature reacting flow reattaches to the wall. This creates higher temperatures next to the wall than would be seen without film cooling. Case 2a and b show the same contrast as 1a and 1b but for a detached jet. For the detached jet, the effects of secondary reactions are seen immediately by an increased temperature directly next to the wall. However, the detached jet provides a lower temperature in regions past approximately 30 diameters downstream. The detached jet also displaces the high temperature reacting layer further

28

away from the wall than the attached jet.   A possible strategy emerges from this information; if a detached layer could be used to separate the flame and reduce the local equivalence ratio and then be following by an attached jet, greater film effectiveness might be achieved.
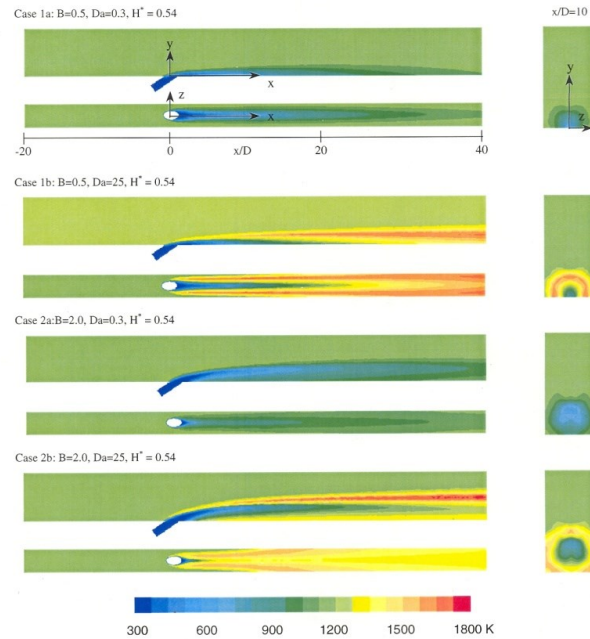


**Figure 0.13:** Kirk et al. numerical computation of temperature profiles for reacting and non-reacting jets

The first studies that attempted to mitigate the effects of reactive film cooling investigated the effects of hole shape and injection angle on the downstream cooling effectiveness.  Anderson et al. [20] examined the effects of secondary reactions experimentally by comparing fan shaped holes with normal cylindrical holes and co-flow cylindrical holes.  Anderson's co-author Evans developed a test setup, shown in Figure

2.14, to quantify the effect of secondary reactions. The test section was supplied with a controlled equivalence ratio of reacted fuel-to-air mixture from a well-stirred reactor similar to the one described later in Section 3.1. The test rig was cooled via water cooling channels imbedded into the back of the testing rig. Two modular film cooling configurations could be inserted into the rig at a time allowing for an upstream and downstream single row configuration. Four thermocouple gauges were imbedded into the test rig; two located at the 25D downstream of the first film cooling insert and two at the 100D downstream.
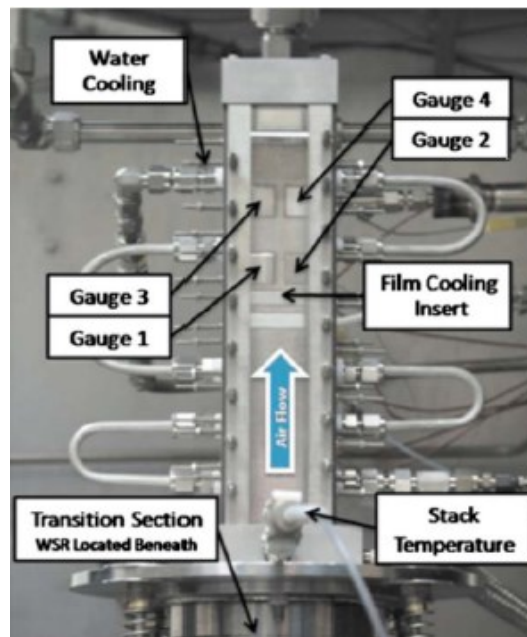


**Figure 0.14: Anderson et al.[20] test rig**

The film cooling inserts were supplied with both $N_2$ and air cooling to allow for comparison between reactive and non-reactive film cooling. The $N_2$ cooling cases approximated the heat flux resulting from an air cooled surface with no secondary

30

reactions and the air case provided the heat flux from a film cooled surface with secondary reactions. Anderson et al. examined blowing ratios varying from 0.5 to 2.0 and equivalence ratios up to $\Phi = 1.6$.

Anderson et al. [20] showed that reactions do occur downstream of the introduction of film cooling in the presence of unburnt radicals and that these reactions result in an augmented heat transfer to the metal for equivalence ratios above stoichiometric. To compare the overall performance of these configurations, an effective convective heat transfer coefficient, $h_{eff}$, was formed. This effective heat transfer coefficient allowed for takes into account the radiative heat flux along with the convective heat flux. Equation 2.2 was modified to the form of an effective convective heat flux, defined as

$$q'' = h_{eff}(T_\infty - T_w) \qquad (2.13)$$

where $h_{eff}$ is effective heat transfer coefficient governing all heat transfer into the instrumentation block and the reference temperature was changed from $T_f$ to $T_\infty$. A comparison of $h_{eff}$ between cooling geometries tested by Anderson et al. [20] is shown in Figure 2.15.

31
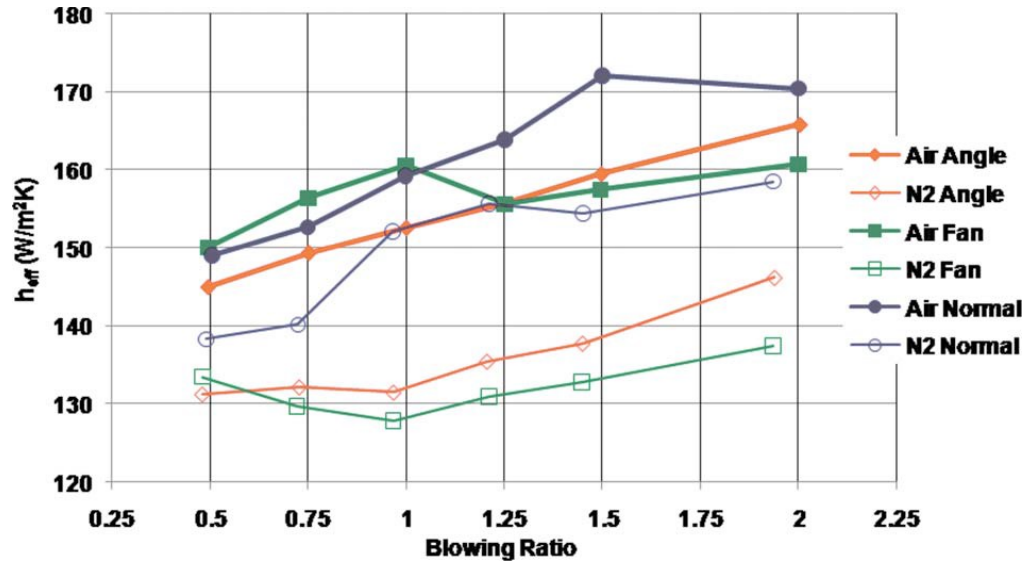
**Figure 0.15:** Comparison of cooling hole geometries: dependence on $h_{eff}$ on M, $\Phi = 1.5$,

*X/D* = 20.

The normal hole produced the lowest degradation of performance and was attributed to the high amount of separation of the coolant holes naturally resulting in the reactions occurring at a higher standoff distance from the wall. The fan-shaped hole showed the greatest reduction of performance since it produces a layer of well attached, spread coolant which resulted in secondary flames in close proximity to the wall. Thus, the fan-shaped holes had the highest overall heat load and the greatest difference between air and nitrogen injection.

Lin et al. [21] performed a computation study on the shaped hole configuration. They compared the results of nitrogen cooling and air cooling for a various range equivalence ratios and blowing ratios. Figure 2.16 shows the mid-plane temperature profile of both nitro and air cooling at M = 2.0 and $\Phi = 1.5$. In both cases, the fluid

leaving the shaped-hole is well attached to the surface. The air case shows a similar trend

of the nitrogen cooling initially but then the temperature dramatically increased

indicating reactions occurring. These reactions are located next to the wall and would

substantially increase the heat flux to the wall. The trends of these results match those of

Anderson et al [20], confirming the shaped hole configuration performs poorly in a fuel-

rich environment.



(a) Air Injection, $M = 2.0$

(b) $N_2$ Injection, $M = 2.0$
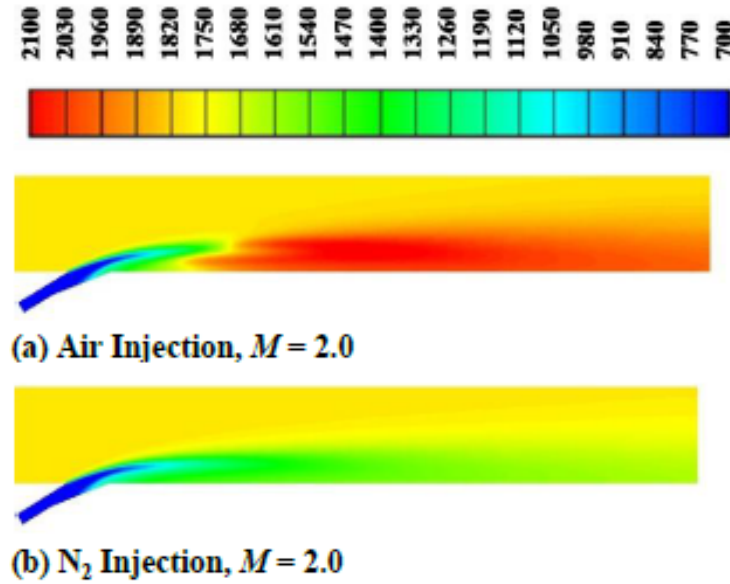
**Figure 0.16:** Midplane Temperature (K) contours; $\Phi = 1.5$, $M = 2.0$ [21]

Bohan et al. [3] examined the effect of having a slot upstream of the fan-shaped

holes used by Anderson. Their study found that an upstream slot could be used to reduce

the heat flux to the wall compared to the fan-shaped holes alone. For the case of $\Phi = 1.5$

and $M = 2.0$, they found the difference between the heat flux in nitrogen cooled case and

the air cooled case to be nearly zero. They concluded that the slot could provide

33

sufficient oxygen to complete the near wall reactions. This resulted in completely reacted flow encountering the downstream fan-shaped holes and as a result negligible heat release due to secondary reaction. Bohan also examined two staggered rows of normal holes in place of the slot and found that it failed to create a protective layer and did not provide enough oxygen to complete secondary reactions away from the wall.

DeLallo [22] continued the research of Bohan et al. by examining a blank plate, normal cylindrical holes, and slot configurations in the upstream row and a trench, fan-shaped, and ramp configurations in the downstream row of coolant. DeLallo confirmed Bohan's results and concluded that a slot followed by a low momentum ratio cooling scheme (e.g. fan-shaped holes or trench) resulted in near zero augmentation of heat flux between reactive and non-reactive cases and was an effective strategy for mitigating secondary reactions downstream.

Since the traditional evaluation metrics of adiabatic effectiveness and overall effectiveness cannot be evaluated with the current studies test rig, another means of evaluation and comparison of the downstream effectiveness is necessary. DeLallo [22] proposed using a parameter coined heat flux augmentation. Heat flux augmentation is defined as the percentage change in heat flux between a reacting and non-reacting case with otherwise similar flow conditions. Augmentation is defined symbolically as

$$\sigma = \frac{q''_{reacting} - q''_{non-reacting}}{q''_{non-reacting}} \tag{2.14}$$

This allows for easy comparison of the degradation of performance due to secondary reactions between cooling schemes. However, this metric fails to account for the

34

difference in mass flows and chemical potentials due to the variety of holes in each configuration. This makes augmentation a poor comparison between cooling schemes with differing numbers of holes.

Anderson et al. [20], DeLallo et al. [6], and Bohan et al. [3] conducted their experiments on the same flat plate test rig. Heat flux measurements in this rig were only available at 25 diameters and 100 diameters downstream of the cooling injection. Bohan et al. took measurements with Planar Laser Induced Fluorescence (PLIF) to identify flow regions where reactions were occurring. The results from this experiment are shown in Figure 2.17 where the reacting case is on the left and the non-reacting case is on the right. The PLIF results revealed that reactions were occurring upstream of the 25 diameter downstream heat flux measurement. This meant that previous studies were missing the effects due to secondary reactions in regions immediately downstream of the coolant injection.
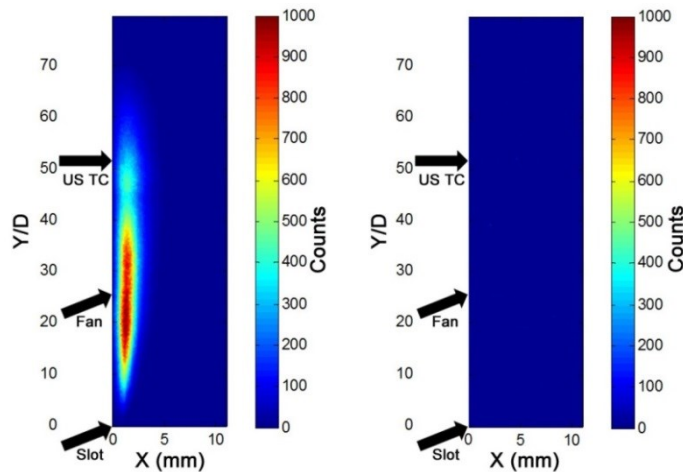


**Figure 0.17:** PLIF measurements showing reaction-indicative OH radical presence [3]

35

In response to the finding of Bohan et al. [3], Robertson [23]constructed a new rig in conjunction with the Air Force Research Laboratory (AFRL) that allowed for heat flux measurements between 10 and 30 diameters downstream. The rig modified by Robertson is used in the current study and further details can be found in Chapter 3. Robertson developed a method for evaluating the flame length based on visible spectrum imagery. These flame images also allowed for evaluation of the starting location of the flame which helped to visualize the trends seen in the heat flux data.

Robertson also developed a new parameter coined the Wall Absorption (WA) parameter which takes into account the differences in mass flow and heat release potential between various cooling schemes. WA is defined as

$$Wall\ Absorption = \frac{q''_{differential} * w_{flame} * L_{flame}}{Q_{potential}} \qquad (2.15)$$

where $q''_{differential}$ is the difference in heat flux between reacting and non-reacting cases, $w_{flame}$ is the width of the flame, $L_{flame}$ is the length of the flame, and $Q_{potential}$ is the maximum potential heat release based on freestream and coolant conditions. The width of the flame was assumed to be the width of a row of cooling holes. The flame length was determined through measurement in visible spectrum images. The maximum potential heat release is determined through the use of CHEMKIN and assumes that all potential reactions occur with the available unconsumed fuel radicals and the injected coolant air. This parameter allows for evaluation of what percentage of the total available heat release is being absorbed by the wall. This parameter is independent of coolant mass flow allowing for comparison between arbitrary cooling geometries.

Robertson [23] preformed a study on the effects of a build-up of rows of cooling holes on the downstream effectiveness. Robertson evaluated the Single Row, Three Row, and Five Row cooling configurations described in Section 3.4.1. The purpose of these designs was to evaluate the feasibility of building a substantial layer of attached coolant beneath a burning layer of coolant. To evaluate these configurations, heat flux measurements of both air and nitrogen cooling were collected. Robertson found his heat flux measurements to be erroneous due to errors in thermocouple location caused by various design flaws with the instrumentation block used. Therefore he focused on the trends in augmentation because augmentation is only a function of the temperature difference between thermocouples at each location and not the actual difference in thermocouple location.

Robertson [23] preformed two different studies on the configurations stated above. The first study was a blowing ratio sweep where the blowing ratio was varied between 0.5 and 4.0 at a constant $\Phi = 1.175$. The results of the blowing ratio sweep test at $X/D = 20$ is shown in Figure 2.18. This study showed that augmentation decreased with increasing blowing ratio.
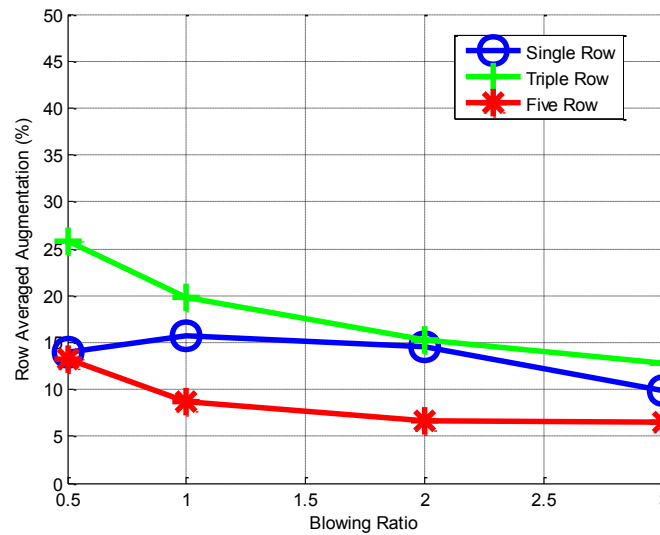
**Figure 0.18:** Robertson: Augmentation vs. Blowing Ratio, $X/D = 20$, $\Phi = 1.175$

The second study was an equivalence ratio sweep where the blowing ratio was held constant at 2.0 and the equivalence ratio was varied from 1.1 to 1.4. The results of the equivalence ratio sweep test at $X/D = 20$ is shown in Figure 2.19.   As equivalence ratio was increased, more radicals were present in the freestream and as a result the augmentation in the local region tested increased due to higher consumption of radicals. The data showed the Five Row performing the most optimally at this location across all equivalence ratio by as much as 10% less augmentation.
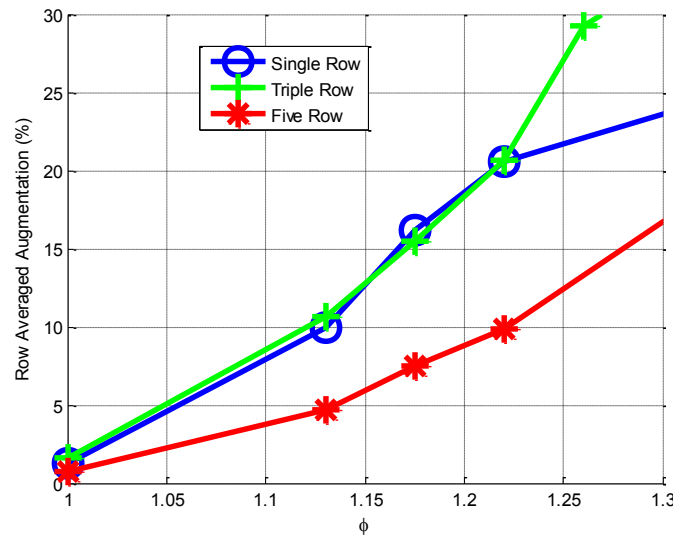
**Figure 0.19:** Robertson: Augmentation vs. Equivalence Ratio, $X/D = 20$, M = 2.0

After evaluation of WA and augmentation, Robertson concluded that an attached coolant layer injected into a fuel-rich flow could protect the wall with the use of five rows of closely spaced injection holes. The Five Row configuration created a non-reacting layer of coolant adjacent that protected the wall from the burning layer of coolant thus reducing the increase in heat flux to the wall. This configuration was able to protect the wall from the effects of secondary reactions with the freestream radicals for some distance downstream of injection.

## III. Experimental Setup

This experiment utilized the reactive film cooling rig constructed by Robertson [23] in conjunction with the Air Force Research Laboratory (AFRL). The rig was designed to achieve a fuel-rich freestream coupled with a typical film cooling flow to enable the study of secondary reactions along a combustor liner or within a turbine. The rig accommodated a larger cooling insert then previous investigations enabling multiple cooling row configurations to be tightly packed. This enabled research into the impacts of multiple cooling rows on the mitigation of these secondary reactions. Furthermore, this rig focused on the capability to take heat flux measurements from 10 to 30 injection hole diameters downstream where the reactions typically initiate. These measurements coupled with infrared imagery of the film cooled wall and visible spectrum imagery of the reactions above the wall provided for a more detailed understanding of the reaction front and the heat release to the wall over a range of equivalence ratios and blowing ratios. This chapter will discuss the major features of this rig. This will include the existing rig components as configured by Robertson such as the Well Stirred Reactor (WSR), the instrumentation and film cooling blocks, and the flow controller systems. Furthermore, this chapter will introduce some new techniques such as the addition of an improved emission measurement system, the implementation of an infrared camera system, and several additional cooling schemes. A second test rig was designed and constructed at the Air Force Institute of Technology (AFIT) and is discussed in Appendix

A. The purpose of this test rig was to examine the effects of surface curvature and Mach number on the effectiveness of film cooling schemes.

### 3.1    Well Stirred Reactor

To simulate turbine entry conditions, the test rig was supplied with a controlled equivalence ratio of reacted fuel-to-air mixture supplied from a Well Stirred Reactor (WSR) as developed by Nenniger et al. [24] and improved by Stouffer [25]. In the WSR, a high rate of mixing of products and incoming reactants was induced, resulting in a nearly uniform distribution of temperature and species at the exit.  This uniformity at the exit allows for the assumption of a uniform distribution of temperature and species within the test section.
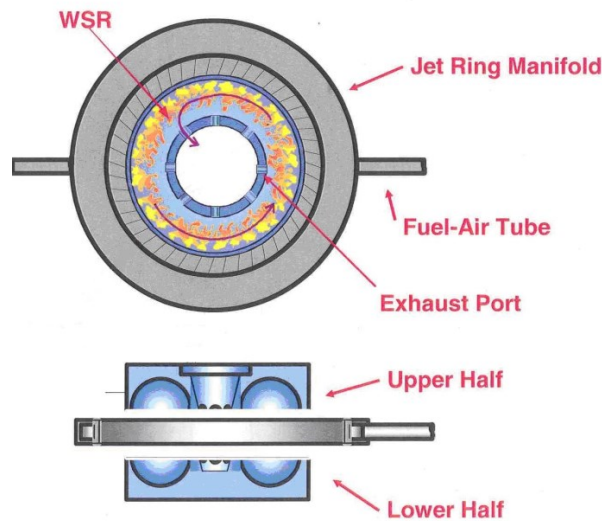


**Figure 0.1:** WSR Schematic

The reactor consists of two Inconel toroidal half sections and an Inconel jet ring, pictured in Figure 3.1. The two toroidal half sections have a thermal barrier coating of Yttria Stabilized Zirconia and fit together on the top and bottom of the jet ring to form a 250 ml internal volume. Premixed fuel and air is supplied to the jet ring which proceeds through 48 fuel-air jets into the reactor. Inside the reactor, the fuel-to-air mixture is ignited. Once the reaction is complete, the combustion products leave through the eight exit ports upwards to the straightener and transition sections.

The lower half-section of the reactor and the jet ring are shown in Figure 3.2. Four ports through the bottom of the reactor allowed for instrumentation of the WSR. A type-B thermocouple, mounted on a stepper motor, allowed for temperature measurements at various locations within the reactor. For the purpose of this experiment, the thermocouple was set at the location were the largest temperature occurred and was monitored to ensure reactor temperature was below 650 K. A ceramic pressure tap, igniter, and an oil-cooled emissions sampling probe were placed in the remaining three ports.
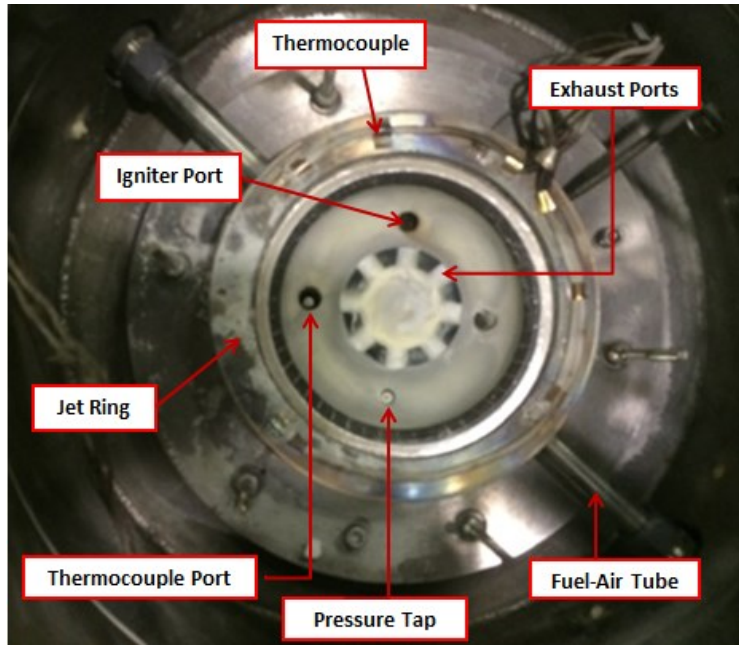
**Figure 0.2:** Lower Toroid Half-Section of WSR in Housing

Coolant channels were machined into both the lower and upper toroid half-section. These cooling channels were designed to produce an even temperature distribution throughout the reactor. The cooling channels were supplied between 0.3 and 0.6 gallons per minute of water. The flow rate was controlled to maintain the temperature of the WSR toroids below 650 K and to ensure the exit temperature of the water was below boiling. Figure 3.3 shows the water inlet and outlet paths along with the cooling paths of the upper toroid.
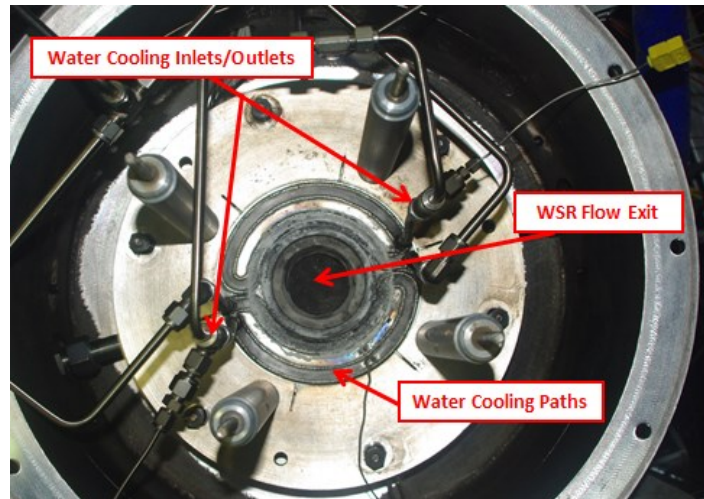
**Figure 0.3:** Fully Assembled WSR in Housing

## 3.2　Straightener and Transition Section

The flow exits the top of the WSR and proceeds into the straightener and transition section. The purpose of the straightener and transition section is to remove the swirl from the flow exiting the WSR and to smoothly transition the reactor exit flow from a circular geometry to the test section geometry. The straightener and transition section is composed of a Hastelloy-X pipe, zirconia type ZYC ceramic outer cylinder, machined zirconia type FBD ceramic transition disks, alignment rods, and a castable alumina ceramic straightener. The components of the transition section are shown in Figure 3.4 and the full assembly of the straightener and transition section is shown in Figure 3.5. The Hastelloy-X pipe acts as the housing for the ceramic outer cylinder, ceramic transition disks, and the ceramic straightener and was positioned concentrically around the WSR exit. The ceramic straightener was then placed downstream of the WSR exit.

44

The outer ceramic cylinder was then placed down around the straightener and held the straightener in place.  The ceramic transition disks were then stacked above the straightener in the proper order and alignment was maintained with the alignment rods.
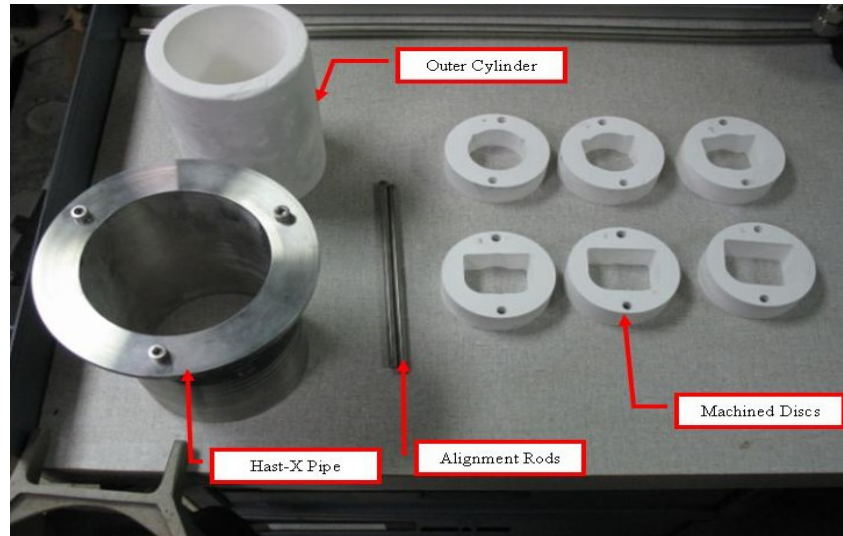


**Figure 0.4:** Transition components [29]

The machined zirconia type FBD ceramic disks transitioned the flow from a circular area of 1464 mm$^2$ to a rectangular area of 863 mm$^2$.  The width of the rectangle was 50.7 mm and its height was 17.78 mm.  Two of the corners were rounded off with a radius of 25.4 mm and served to match the transition section with the support columns of the testing rig.  The hydraulic diameter of the transition section and the test rig is 26.4 mm.  The shape of the final area of the transition section was designed to create a flat wall on one face for the flat plate film cooling.  The remaining geometry features of the transition area were designed to smoothly transition to the features of the testing rig.

45

**Figure 0.5:** Fully Assembled Straightener and Transition Section

The ceramic straightener, shown in Figure 3.6, is a single eight spoke flow straightener that was first implemented by Bohan [19]. Bohan reported an improvement in spanwise uniformity after implementation of the flow straightener. To further improve spanwise uniformity, two flow straighteners were combined using ceramic adhesive. Even with this improvement, some non-uniformity still exists in the flow. A discussion of the uniformity of the temperature distribution across the instrumentation block can be found in Section 4.2.
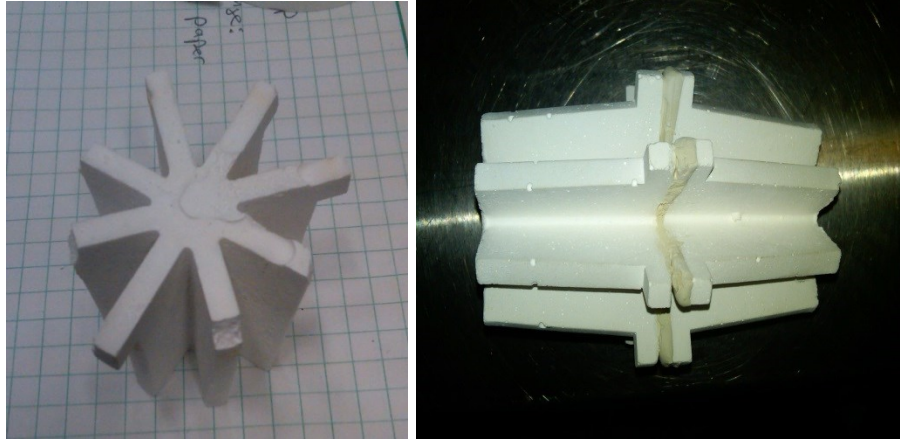
**Figure 0.6:** Single Flow Straightener (Left), Double Flow Straightener (Right)

In order to provide a stable platform to secure the test rig, a mounting plate made of Hastelloy-X was designed. The mounting plate was secured to the Hastelloy-X pipe via three ¼''-20 screws. To provide further support to the testing rig, four support columns were installed connecting the mounting plate to the WSR. The support columns compressed the transition section in place between the WSR housing and the mounting plate ensuring the transition section and test section remained aligned. Figure 3.7 shows how the mounting plate secures the testing rig to the WSR and the transition section.
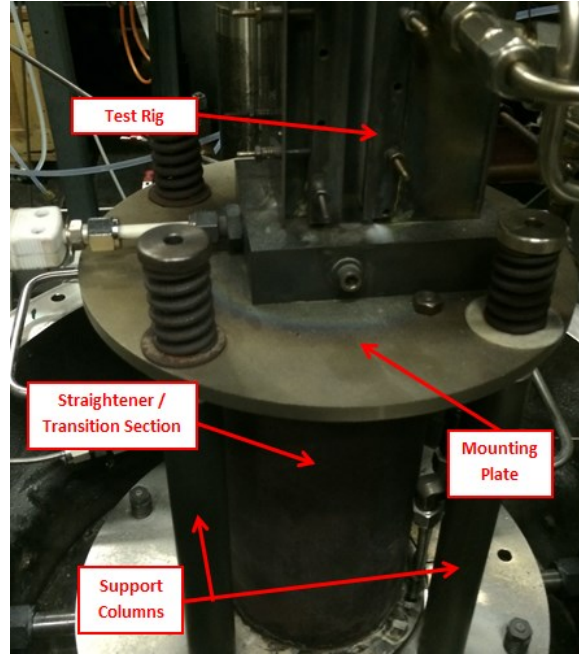
**Figure 0.7:** Mounting Plate and Rig Support

### 3.3    Flat Plate Film Cooling – Test Section

The test rig is shown in Figure 3.8 and consisted of a test section comprised of a

cooling plenum accommodating multiple film-cooling plates, an instrumentation block

consisting of 16 heat transfer gauge assemblies, and front and side window assemblies.

Two quartz windows formed the side walls of the test section allowing for optical access.

A sliding frame containing a quartz and sapphire window was positioned within the

opposite wall of the flat plate cooling scheme.  The nominal freestream velocity was

73 m/s giving a $Re_{DH} = 6260$.  For the test case of $\Phi = 1.175$ and a freestream

temperature of 1690 K, the average inlet Mach number was 0.091.
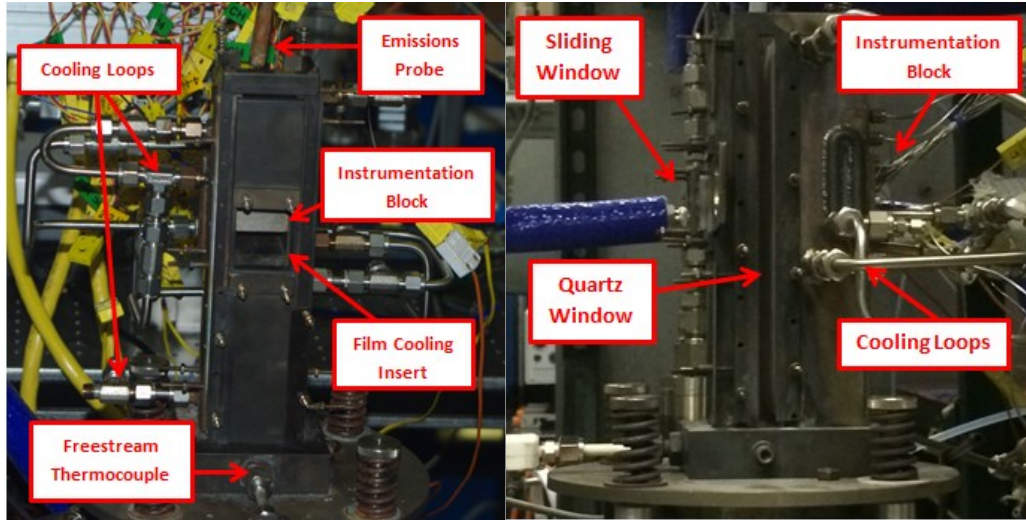
**Figure 0.8:** Test Section, Front View (left); Side View (right)

The core component of the test section was a 28 cm × 5.08 cm × 6.35 cm Hastelloy-X block machined to accept the instrumentation block and flat plate cooling schemes as inserts.  The test section was designed so the flat plate cooling schemes were modular and could be switched out with ease. About 45 minutes were needed to allow the rig to cool down, safely swap the blocks and reignite the rig. The Hastelloy-X block was cooled with water, nitrogen, or a Mokon oil temperature control system through welded cooling loops and channels to maintain structural integrity and vary wall temperature. This thesis only utilized the Mokon oil cooling. The cooling loops, shown in Figures 3.8, were designed to setup a one-dimensional heat transfer condition for the instrumentation block and film cooling insert. Greiner et al. **Error! Reference source not found.** examined the heat transfer within the instrumentation block and found it was sufficiently one dimensional.  The Hastelloy-X block was also machined with a step, shown in Figure

49

3.9, designed to trip the flow to ensure turbulence within the test section. The step height was 7.01 mm and was designed to ensure the flow was fully transitioned to turbulent flow by the time it reached the film cooling insert and instrumentation block.
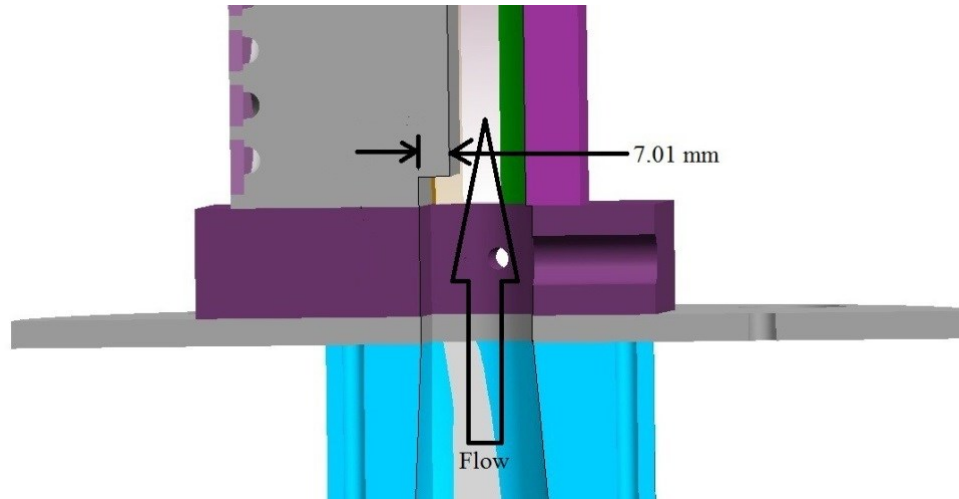


**Figure 0.9:** Hastelloy-X block step

Throughout the course of testing, a Mokon oil temperature control system was utilized to provide the testing rig with cold-side coolant. The Mokon oil control system uses an electric heater and water-cooled heat exchanger system to control the temperature of the oil is then pumped to the emissions probe and the rig's cooling loops. At the inlet to the rig, the oil temperature was measured at 420 K ± 12 K for all testing except the infrared wall temperature calibration described in Section 3.3.2. The Mokon oil entered the top of the Hastelloy-X block and proceeded through the upper cooling loop, exiting above the instrumentation block. The cooling flow then is split into two cooling paths feeding the upper portion of the lower cooling loop and the side loop. The flow is then

recombined and passed back into the oil system. A schematic of the cooling paths in the

Hastelloy-X block, created by Robertson [23] is shown in Figure 3.10.
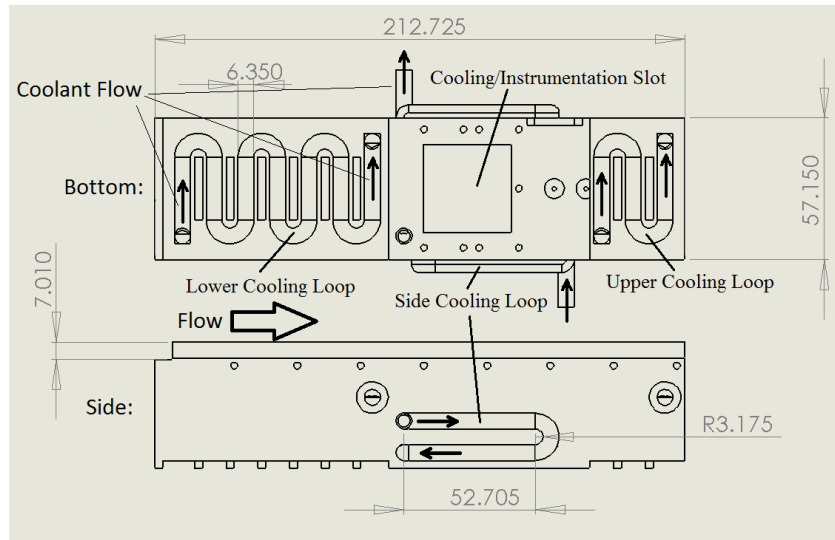


**Figure 0.10:** Hastelloy-X Block Cooling Paths Schematic [23]

The freestream fluid temperature at the inlet to the test section was measured with

a B-type thermocouple and served as a reference temperature. The freestream

temperature was directly related to the equivalence ratio of the well-stirred reactor. At an

$\Phi = 1.1$ the average exhaust temperature was 1690 K which decreased to 1590 K at an

$\Phi = 1.4$. The average exhaust temperatures varied as testing proceeded. An analysis on

the repeatability of the average exhaust temperature over the course of testing is provided

in Section 3.6.

The film cooling insert was a combination of modular rectangular film cooling

plates and a universal plenum inserted into the Hastelloy-X block. The cooling insert laid

flush with the hot side surface of the Hastelloy-X block and was secured on the cold side.

51

The plenum allowed for the use of multiple rows of coolant compared to the single rows of coolant used in previous AFIT research [23] which allowed for the study of the cooling configurations described in Section 3.4. A thermocouple was inserted into the cooling plenum and was positioned 2mm away from the wall of the internal face of the film cooling plate. This temperature measurement was considered the coolant temperature and the rise in temperature through the plate was neglected.

Designed to evaluate the downstream effectiveness of various film cooling configurations, the test section allows for evaluation of downstream heat flux, acquisition of infrared and visual spectrum imagery, and collection of CO, $O_2$, and $CO_2$ emissions. Downstream heat flux was measured through the use of the instrumentation block, described in Section 3.3.1. The various optical access features of the testing rig, the viewing areas, and the specifications of the cameras and lens used is discussed in Section 3.3.2. The emission collection probe and the sampling train are described in detail in Section 3.3.3.

### 3.3.1    Instrumentation Block

A removable Hastelloy-X instrumentation block (Figure 3.11) was integrated immediately downstream of the film cooling scheme insert. The instrumentation block was installed with sixteen pairs of 0.51 mm diameter, Omega® ungrounded Inconel 660 Type-K thermocouples, allowing for heat flux measurements between 10 and 30 injection hole diameters downstream. Each thermocouple pair consisted of an upper and lower thermocouple that were spaced 5.08 mm apart in the direction normal to the hot gas side

52

surface. The lower thermocouples were embedded through holes drilled in the backside of the instrumentation block. The upper thermocouples proceeded up the length of the instrumentation block through trenches and embedded through holes drilled into the sides of the instrumentation block. This design allowed the upper and lower thermocouples to be at the same spanwise and streamwise location but have spacing in the direction normal to the film cooled wall.
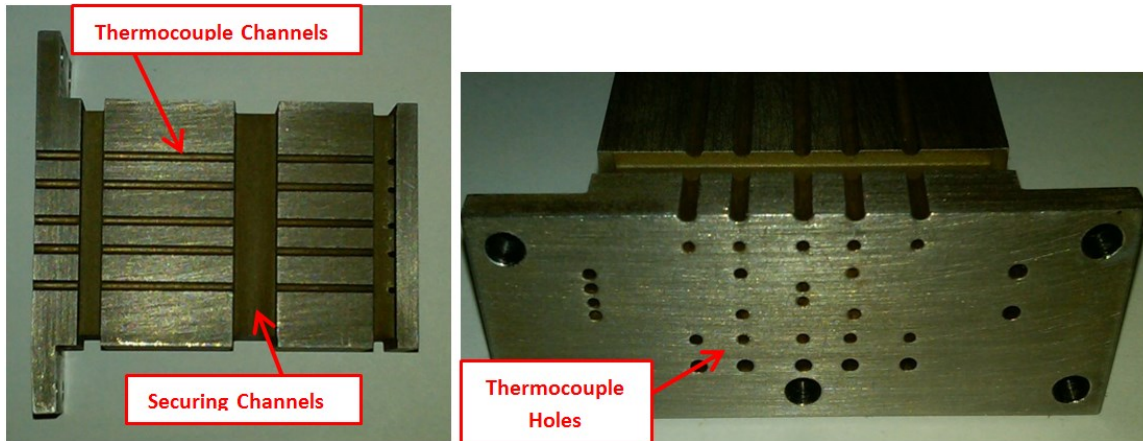


**Figure 0.11:** Instrumentation Block, Top View (Left), Backside View (Right)

The thermocouple pairs in the instrumentation block were spaced into four rows. These rows were located at 10, 17, 22, and 30 hole diameters downstream of the last row of cooling holes. $X/D = 10$ and $X/D = 30$ consisted of five sets of thermocouple pairs each. $X/D = 17$ and $X/D = 22$ had three pairs of thermocouples each. The locations of the thermocouple pairs with respect to the Five Row configuration, which will be described in Section 3.6.1, are shown in Figure 3.12. The origin of the coordinate system is centered on the center of the last row of cooling holes. The thermocouples at $X/D = 17$

53

and $X/D = 22$ are staggered slightly due to machining constraints but it is assumed that each set of three thermocouples are at the average downstream location of the group. Linking these thermocouple measurements and heat flux calculations with side window visualization and infrared imaging normal to the surface allow for a better insight on where reactions take place and their impact on downstream effectiveness.
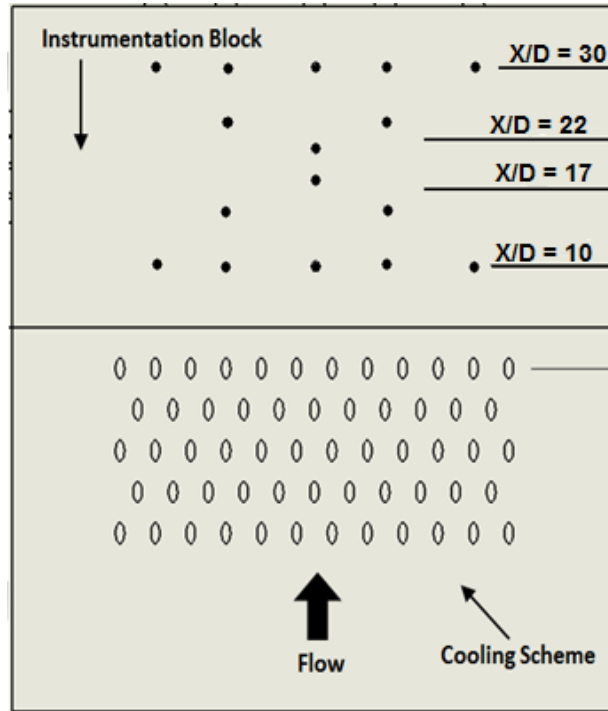


**Figure 0.12:** Visualization of thermocouple pair locations

The original design of the instrumentation block was utilized by Robertson [23]. During Robertson's testing, some of the thermocouples backed out of their hole. This created an air gap along with an unknown depth for the thermocouples. The first and last rows of thermocouples provided the most difficulty ensuring that the thermocouples were

secured and the correct spacing between thermocouples in each pair was maintained. The holes drilled into the instrumentation block to house the upper thermocouples for the first and fourth row were initially machined parallel to the flat plate section exposed to the hot gases and they were machined 2.39mm away from the edge of the block. This resulted in a very shallow insertion depth with a sharp 90° turn. So the first and last rows of thermocouples were prone to being pulled out of their correct locations. The lower thermocouples were also not efficiently secured in place and were prone to dislocation due to pulling on the wiring when the film cooling plates were switched. Improper spacing between the thermocouple pairs results in a dramatic variation of the calculated values of heat flux and wall temperature.

To solve the problem of thermocouples being displaced from their proper locations, the instrumentation block was modified. The paths drilled for the first and fourth row of upper thermocouples were modified so they were embedded 3.39 mm into the block and they were angled at 45° into the block. To hold the thermocouples in place, three groves were cut out and bands were welded on top of the thermocouples. To hold the lower thermocouples in place, JB weld was applied to the backside. The fully assembled modified instrumentation block can be seen in Figure 3.13. Modification of how the thermocouples were held in place allowed for a more precise knowledge of the distance between thermocouples in a pair. Thus, heat flux measurements were more precise compared to the previous version of the instrumentation block.
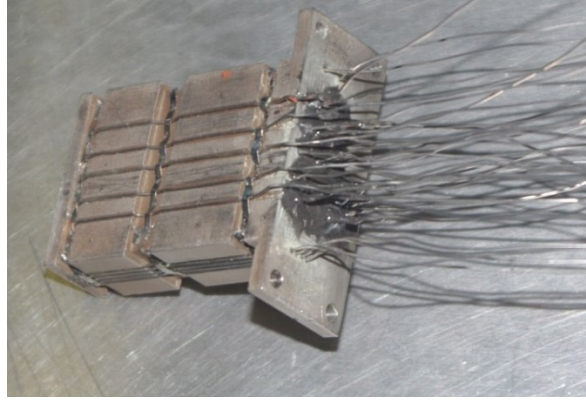
**Figure 0.13:** Fully assembled modified instrumentation block

Knowing the precise location of all thermocouples within the instrumentation block is crucial to minimizing the error within heat flux and wall temperature calculations. To obtain more precise locations, a calibration was designed that examined a steady state condition with no film cooling. The wall temperature and heat flux for this case were equal across the instrumentation block. At each thermocouple pair location, the heat flux and wall temperature were calculated. The average and standard deviation were calculated based on this data set and any thermocouple pair outside two standard deviations from the mean were removed from the data set. A new "true" average was calculated based on only the thermocouple pairs that fell within two standard deviations of the original mean. These "true" averages of wall temperature and heat flux were used to back solve for the distance from the upper thermocouple to the hot side wall and to solve for the distance between the thermocouples at each thermocouple pair for the locations that were thrown out of the "true" average. These corrected locations were used in all calculations in this thesis. Table 3.1 contains the location of each

thermocouple pair and the distance between the thermocouples in each pair. The 1-1
location corresponds with the bottom left thermocouple and 4-5 the top right
thermocouple in Figure 3.12.

**Table 0.1: Thermocouple locations in the instrumentation block**

| Location | x (mm) | z (mm) | dx (mm) |
|----------|--------|--------|---------|
| 1-1 | -12.2 | 2.39 | 13.4 |
| 1-2 | -6.1 | 2.39 | 9.41 |
| 1-3 | 0 | 2.39 | 12.2 |
| 1-4 | 6.1 | 2.39 | 22.1 |
| 1-5 | -12.2 | 2.39 | 9.28 |
| 2-2 | -6.1 | 6.18 | 12.33 |
| 2-3 | 0 | 7.23 | 19.3 |
| 2-4 | 6.1 | 6.18 | 10.6 |
| 3-2 | -6.1 | 9.53 | 22.45 |
| 3-3 | 0 | 8.62 | 10.68 |
| 3-4 | 6.1 | 9.53 | 10.85 |
| 4-1 | -12.2 | 13.49 | 11.55 |
| 4-2 | -6.1 | 13.49 | 7.25 |
| 4-3 | 0 | 13.49 | 9.42 |
| 4-4 | 6.1 | 13.49 | 9.66 |
| 4-5 | -12.2 | 13.49 | 7.71 |

### 3.3.2    Optical Access and Imaging Tools

To enable visual representation of the secondary reactions emanating from the
cooling holes, two fused silica windows were integrated into the test section. These
windows, shown in Figure 3.8, formed the two side walls for hot gases in the test section.

Images were captured from the side with a Pentax K200D camera set with a shutter speed of two seconds, an ISO at 400, and the aperture at f/16. These images were later modified to enhance the flame within the images. These images enabled qualitative information on the flame structures formed by secondary reactions between the coolant and rich freestream flow. Values such as flame length and starting location were quantified and provided insight on the various cooling configurations examined.

To enhance the flame images, each photograph was loaded into MATLAB as a matrix of values describing each pixel by a red, green, and blue eight-bit value. All pixels with blue values above a threshold based on the maximum blue value of the flame were modified by scaling them up. The flame was then considered to start when the blue value reached 5% of the maximum blue value and the considered to end at 10% of the maximum blue value. The program then drew vertical white lines at the beginning and end of the flame and the distance between these lines was used to calculate flame length.

The front of the rig was installed with a sliding plate that held a 35 mm diameter sapphire window and fused silica window. The window frames were designed so the window could easily slide within its brackets. This allowed the windows to be positioned in place when needed and to be stored safely out of the fuel-rich flow when not in use. The window was positioned out of the flow while waiting for the temperature to reach steady state. Once the rig was at steady state, the window was moved in place and the IR image was taken. The window was then slid back out so it was no longer exposed to the flame or any soot being produced. The front view of the test section with sliding window

58

installed is shown in Figure 3.14.  The positioning of the sliding window allowed for viewing of the Five Row cooling scheme and the entire length of the instrumentation block.  The sapphire window was used for infrared imaging due to its high transitivity of 0.9 for the wavelengths being examined in this study.

Due to high thermal gradients between the hot freestream gases and the ambient air, the sapphire window cracked.  This crack spans from the top center of the window to the left edge.  Various methods were examined to stop the window from breaking.  The only successful method was to create a new plate to hold the window.   The new plate integrated the window as a portion of the wall. This exposes the window to the hot freestream gases for the whole duration of testing.  This solution was not found until the majority of testing was done so this experiment continued to use the sliding holder and the cracked sapphire window.  However, it was shown that a sapphire window could remain intact at the testing conditions.
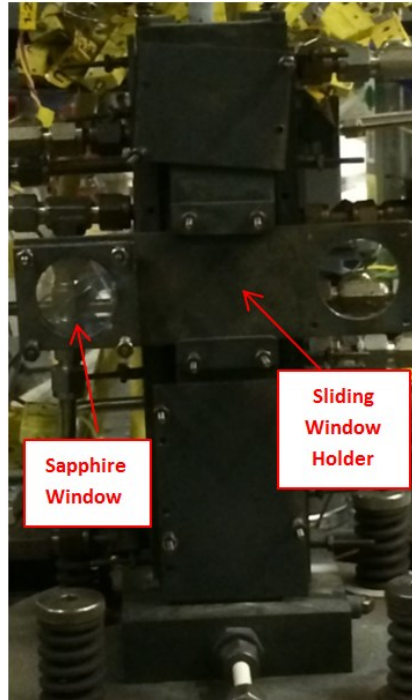
**Figure 0.14:** Test section with sliding window installed

The infrared camera used in this thesis was a FLIR SC6700.  This camera had a
maximum resolution of 640 × 512 at 124 fps and a maximum frame rate of 4.175 kHz at
its minimum resolution of 16 × 4.   The goal of the IR camera is to obtain a continuous
measurement of the downstream wall temperatures compared to the discrete calculations
of wall temperature made at each thermocouple pair location.  To achieve this, the IR
camera must look past the hot gasses and obtain measurements of the wall.  A pass-band
"flame" filter was used with the camera to achieve this goal.  The pass-band "flame"
filter blocked out all wavelengths except 3.750-4.200 μm which blocked out the
chemiluminescence of the hot gasses and secondary reactions.  This allowed for
measurement of the raw radiative component of the film cooled wall within this band.  IR

images were obtained at 60 fps over a duration of 15 seconds at a resolution of

$320 \times 240$. A detailed description of how the IR camera was setup and the setting used is

described in Appendix B.

Because the IR camera was only examined the voltage potential within a small

band of wavelengths and not the full blackbody signature, traditional conversions

between voltage potential and temperature do not apply. In order to convert the voltage

potential experienced by the IR camera to the temperature of the wall, a calibration was

performed. IR images were obtained at varying wall temperatures. Wall temperatures

were calculated at each thermocouple pair location and plotted against the measure of

counts displayed by the camera for the various testing conditions, shown in Figure 3.15.
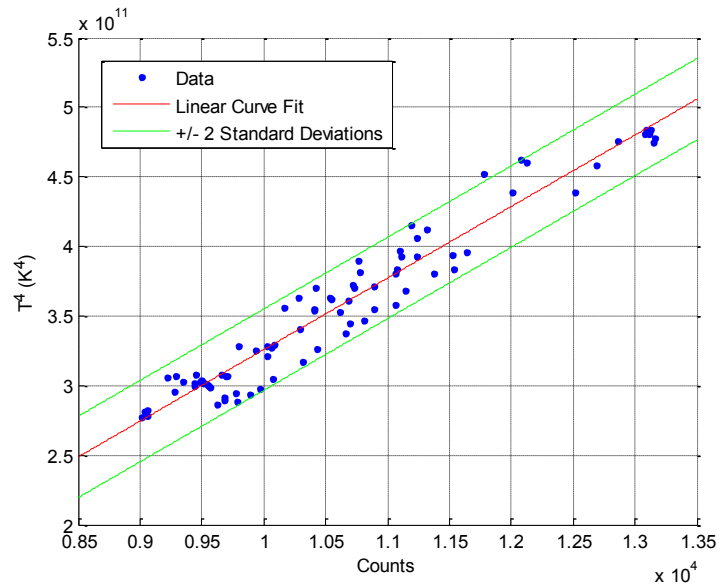


**Figure 0.15:** IR Calibration

A linear curve fit was then applied to the data and is shown in Equation 3.1 below:

$$T_w^4 = \frac{1}{0.343\sigma} (Counts - 3669) \qquad\qquad (3.1)$$

where $\sigma$ is the Stefan-Boltzmann constant ($\sigma = 5.67$ x $10^{-8}$ W/m$^2$ × K$^4$), $T_w$ ($K$) is the wall temperature, and counts is the voltage potential measured by the IR camera. The curve fit resulted in a standard deviation in wall temperature of 8 K. The 95% confidence interval around the curve fit is shown in green in Figure 3.16.   shows that a linear curve fit adequately modeled the data.

To apply the IR calibration it is vital to ensure the emissivity and reflectivity of the instrumentation block remain constant over the course of testing. Figure 3.16 shows a comparison between un-oxidized and oxidized Hastelloy-X. The un-oxidized image was taken shortly after machining was finished and the oxidized image was produced after several hours of baking at 600 K. Wade [27] showed the emissivity of Hastelloy-X increases greatly from its un-oxidized state to the oxidized state and the reflectivity drastically decreases. To ensure consistent IR images, it is advised to fully oxidize the film cooling plates by heating them at 600 K or higher for several hours.
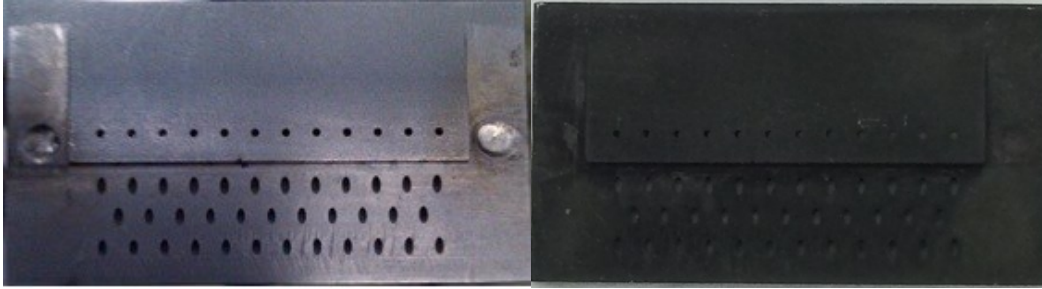
**Figure 0.16:** Variation in surface emissivity; Un-Oxidized (Left), Oxidized (Right)

### 3.3.3    Emissions Acquisition

To determine the chemical composition of the flow downstream of the film cooling, an emissions sampling probe was installed (See Figure 3.17) downstream of the test section.  The emission probe was a tube within a tube where emissions were sampled through the 6.35 mm inner tube.  The outer tube contained the cooling to maintain the temperature of the emission probe.  The probe was cooled via 422 K oil from the Mokon Oil temperature control system.  The emissions line was also heated to 422 K until it reached the sampling conditioning unit.  The emissions probe was mounted on a traverse giving the probe 25 mm of movement in the direction normal to the film cooled wall. The probe was positioned at $X/D = 200$ and $Z/D = 0$.   This allowed for evaluation of various cooling schemes consumption of radicals as a function of distance from the wall.

**Figure 0.17:** Emissions Probe

The emissions sample was transported to a series of emissions analyzers through heated sampling lines that were maintained at 422 K. The sample proceeded to the Sample Conditioning Unit where it was chilled and dried to remove water from the sample before proceeding to the analyzers. The dried sample was then routed through a system of analyzers which measured $CO_2$, $NO_x$, $O_2$, and CO. For the duration of testing done, the $NO_x$ analyzer was inoperable and as such measurements of $NO_x$ were not examined. A schematic of the sampling train of the emissions is shown in Figure 3.18.
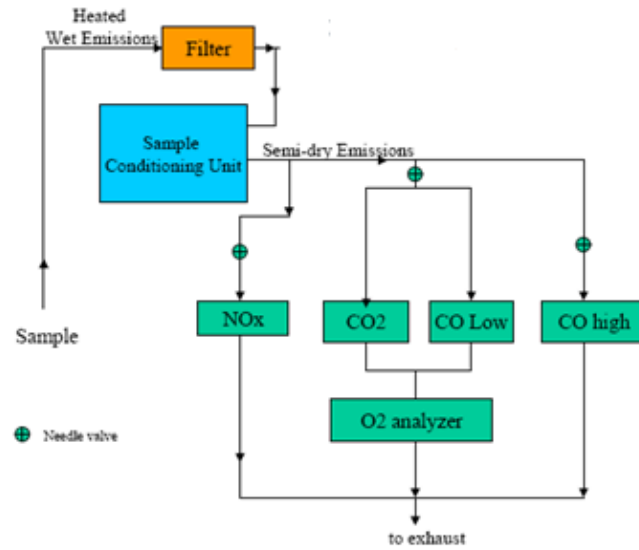
**Figure 0.18:** Sampling train schematic of gaseous emission measurements

A variety of cooling configurations were produced and tested with differing strategies to gain insight on reactive film cooling. The first objective of these cooling configurations was to evaluate previous trends and conclusions made by Robertson [23] on the build-up of multiple rows of cooling holes with the recalibrated heat flux measurements. Detailed descriptions of the cooling configurations used to evaluate Robertson's results are found in Section 3.4.1. The second objective was to examine various five row cooling schemes with the goals of protecting the wall and consumption of radicals. The cooling configurations used to achieve this second objective are detailed in Section 3.4.2.

65

## 3.4    Film Cooling Configurations

A variety of cooling configurations were produced and tested with differing strategies to gain insight on reactive film cooling.  The first objective of these cooling configurations was to evaluate previous trends and conclusions made by Robertson [23] on the build-up of multiple rows of cooling holes with the recalibrated heat flux measurements. Detailed descriptions of the cooling configurations used to evaluate Robertson's results are found in Section 3.4.1.   The second objective was to examine various five row cooling schemes with the goals of protecting the wall and consumption of radicals.   These cooling configurations used to achieve this second objective are detailed in Section 3.4.2. Lastly, Section 3.4.3 outlines the third set of cooling schemes; namely those designed for the consumption of radicals.

### 3.4.1    Robertson's Row Build-Up Campaign Evaluation

Robertson initially aimed to investigate the effects of compounding rows of film cooling holes to determine if upstream, sacrificial rows could be utilized to protect rows of coolant further downstream. The desired intent of building up multiple rows of coolant was to separate reactions from the wall through the creation of a thick coolant layer.  In short, a non-reactive layer of film would buffer the wall from a reactive layer of film. Robertson studied three cylindrical hole configurations angled at 30˚ from streamwise. The Single Row configuration featured a single row of twelve cylindrical holes with a diameter of 0.51mm with a hole spacing of four diameters in the spanwise direction.  The

66

length-to-diameter ratio (L/D) was 5.0.  The Single Row is shown in Figure 3.19 and served as the baseline.
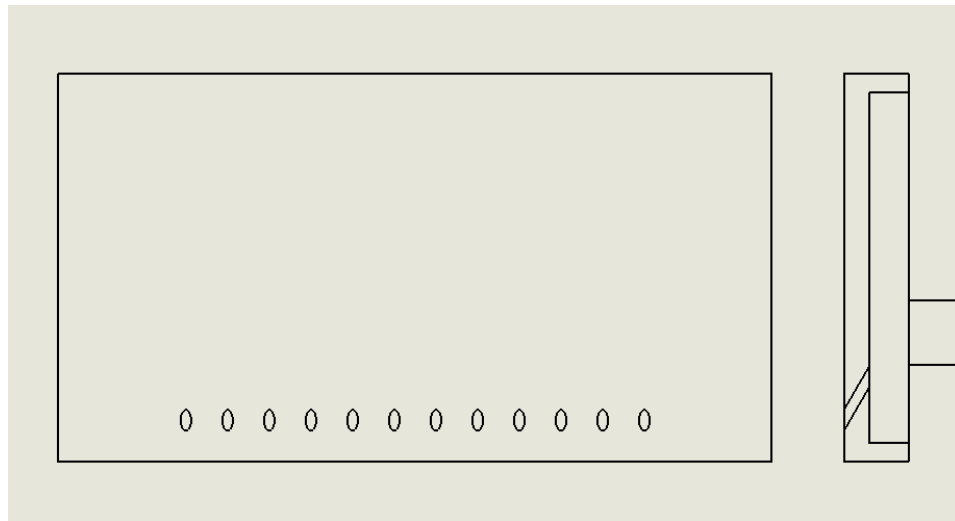


**Figure 0.19:** Single Row of Cylindrical Holes at 30˚, Top View

This data was subsequently compared to the Three Row configuration which consisted of three evenly spaced rows of cylindrical holes.  The rows were spaced four diameters in the streamwise direction from each other.  The holes had a diameter of 0.51mm, injection angle of 30˚ above the streamwise coordinate, and L/D = 5.0.  These rows were staggered such that the rows of coolant alternated twelve and eleven cooling holes.  Each cooling row maintained a hole spacing of four diameters.  The Three Row configuration is shown in Figure 3.20.
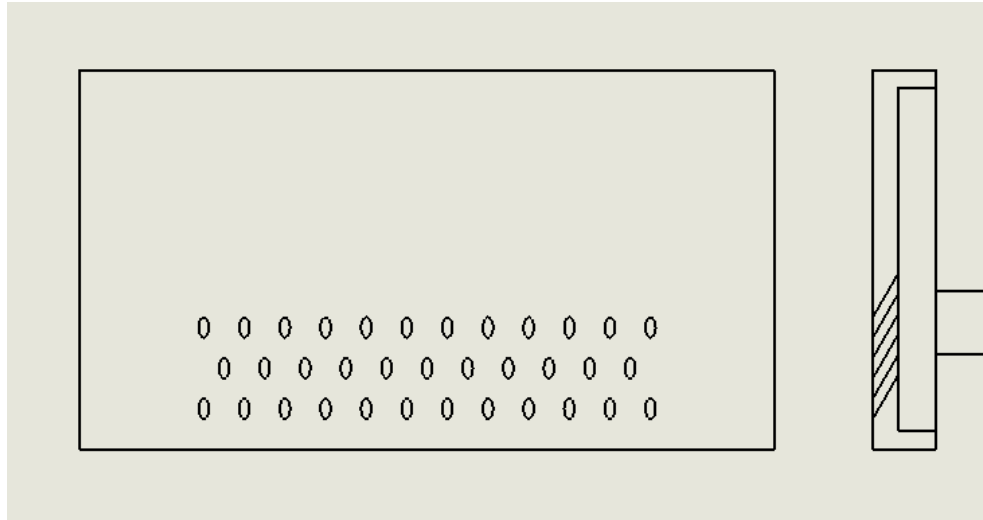
**Figure 0.20:** Three Rows of Cylindrical Holes at 30˚, Top View

The final configuration tested was the Five Row configuration which consists of five evenly spaced rows of cylindrical holes.  Previous research, (Section 2.3), showed that there is a similarity pattern that establishes for non-reacting film cooling configurations with more than five rows.  As such, this investigation focused on five rows of injection holes. The Five Row followed the same pattern as the Three Row configuration and the hole sizing, spacing, and injection angle remained the same.  The odd number rows consisted of twelve cooling holes and the even number rows consisted of eleven holes offset from the adjacent rows.  The Five Row configuration is shown in Figure 3.21.
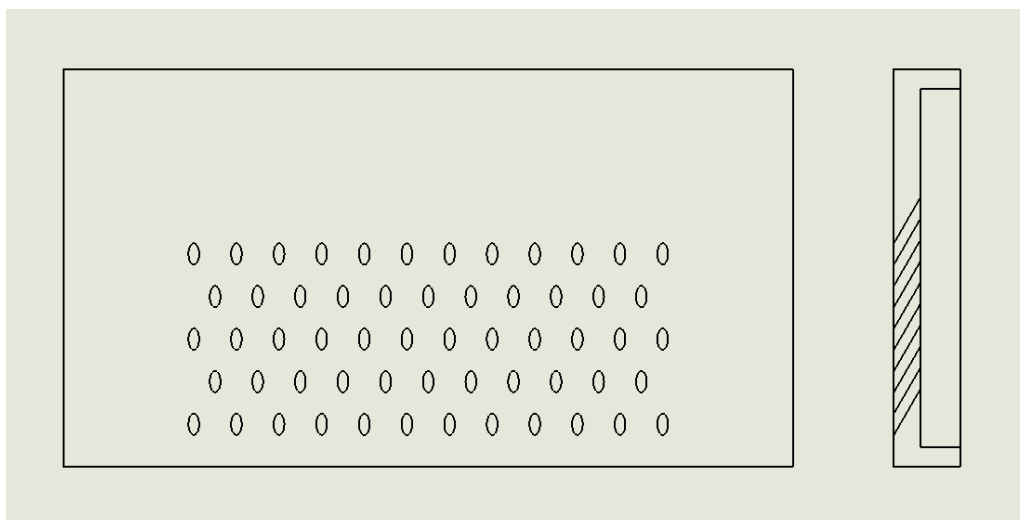
**Figure 0.21:** Five Rows of Cylindrical Holes at 30˚, Top View

### 3.4.2   Additional Cooling Configurations

Based on the results (to be discussed in Chapter 4.4) of the Five Row scheme, the

research then attempted to examine alternate configurations with five rows of coolant

with the goals of promoting mixing and consumption of radicals away from the wall and

minimization of the impact secondary reactions on the wall. Enhanced mixing schemes

would allow for higher consumption of radicals in the local region while reducing the

total available radicals further downstream.

#### 3.4.2.1 Roll Forward

The Roll Forward configuration was designed with the goal of creating a

sacrificial layer of detached coolant upstream of an attached layer of non-reacting film.  It

was hypothesized that the upstream rows would consume radicals quickly and away from

the wall, thus reducing the amount of reactive species near the wall available for reaction

69

with the downstream rows.  This would enable the coolant from the shallower angled downstream rows to cool more effectively.  To achieve this, coolant was injected from the same surface locations as the Five Row but the injection angle was varied from normal to the flow to 30° above the streamwise coordinate. The furthest upstream row injected normal to the flow and each proceeding row injection angle was reduced by 15°. The initial rows of coolant are detached from the wall and mix with the freestream, while subsequent rows remain attached beneath the layer of reactive film.
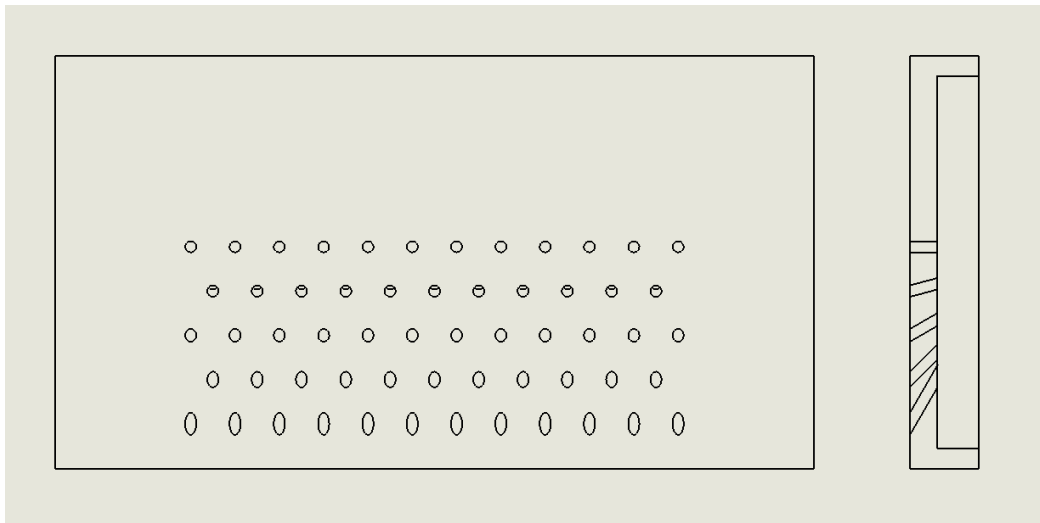


**Figure 0.22:** Roll Forward Cooling Configuration, Side and Top View

### 3.4.2.2 Two Row Upstream

The Two Row Upstream configuration was designed to evaluate if the increased penetration due to upstream-facing holes as shown by Oguntade et al. [9]. This increased penetration could be advantageous in a reacting film situation. Using the Three Row configuration as a baseline, the Two Row Upstream added two rows of injection holes,

eight diameters upstream of the most upstream row in the Three Row.   These two

upstream rows were injected at 150° from the streamwise coordinate.  The initial row of

upstream-facing holes consisted of twelve holes of coolant and the second row consisted

of eleven holes offset spanwise from the initial row.  The two rows of upstream-facing

holes were hypothesized to promote mixing and to create a flame zone away from the

wall.  The configuration is shown in Figure 3.23.
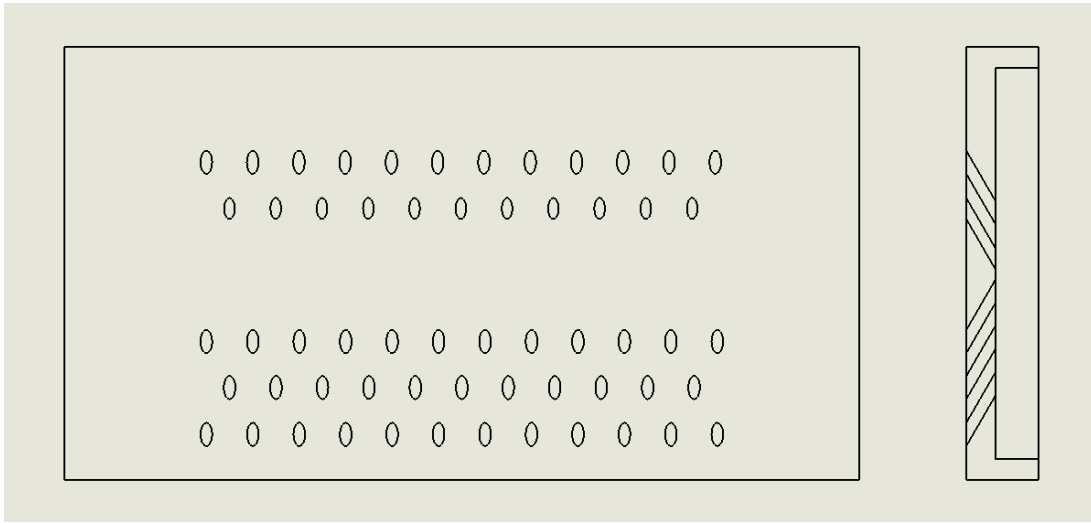


**Figure 0.23:** Two Row Upstream Cooling Configuration, Top View

### 3.4.2.3 Backward Facing Step

Previous reactive film cooling research conducted by Milanes et. al. [28]

examined a backward facing step and showed that modification of the coolant blowing

ratio allowed for control of the mixing layer.  Knowing and controlling where additional

heat transfer to the wall is going to occur, would allow for internal cooling schemes to be

modified accounting for the increased heat transfer.  For the current research, the

backward facing step with a height of 1.5 diameters is followed by three rows of coolant injected at 30˚, shown in Figure 3.24.  Twelve normal injection holes were placed at the top of the step and had a L/D of 4. This single row of normal holes was meant to act as a sacrificial row that starts the reacting process at the top of the step away from the wall. Eleven injection holes angled at 20˚ from the streamwise coordinate were placed at the face of the step and had a L/D of 16. These holes were meant to buffer the flame created by the row of normal holes further away from the wall. The three remaining rows were located at the same locations as the Three Row configuration.  The distance between the step and these rows of coolant was 4D.
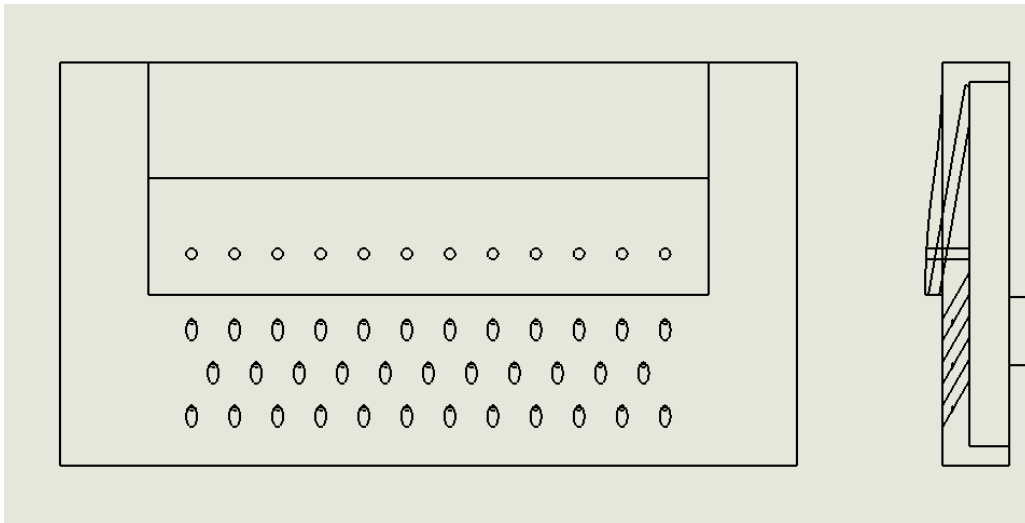


**Figure 0.24:** Backward Facing Step - Side View (Left), Top View (Right)

### 3.4.2.4 Crossflow

The Crossflow configuration, shown in Figure 3.25, used the Five Row as a base and added two upstream rows that injected spanwise. The first spanwise injection row injected coolant at 45˚ above the spanwise coordinate while the second row injected 45˚ above the spanwise in the opposite direction. The Crossflow aims at reducing the amount of radicals available to the five rows of coolant downstream through the creation of high turbulence and mixing formed by the opposing crossflow injection.
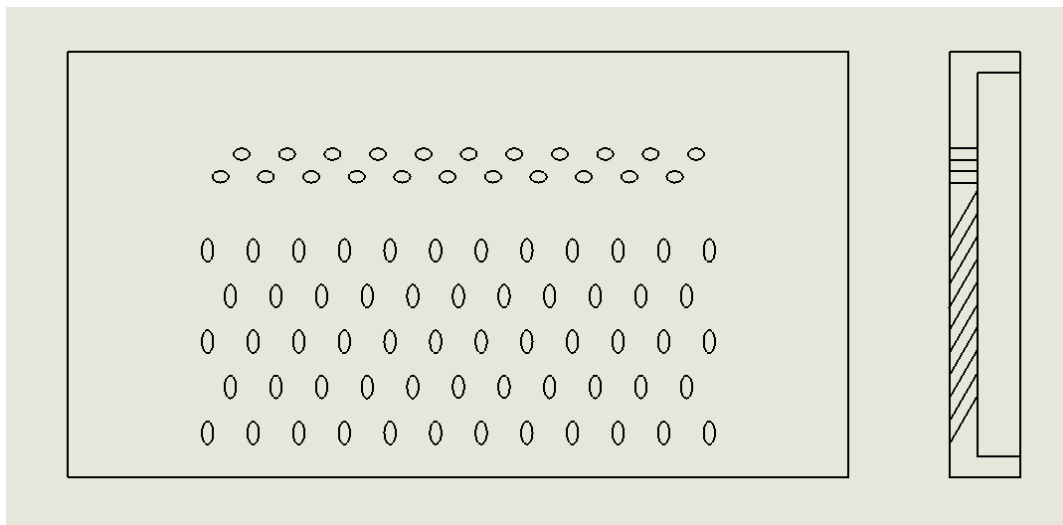


**Figure 0.25:** Cross Flow, Top View (Left), Side View (Right)

### 3.4.2.5 Enhanced Swirler

The Enhanced Swirler configuration, shown in Figure 3.26, was designed with the goal of creating two large vortices above the cooling region that promote rapid mixing and circulation. To achieve this, the injection angle was swept from outboard holes to central ones. This scheme was designed to attempt to shape and control the flame to a

smaller area.  By confining the flame to a known, smaller region, the overall effects of secondary reactions would be reduced.  The area under the flame, however, would experience an increase in heat transfer to the wall.  To counteract this increased heat transfer, the region where the increased heat transfer is occurring could be more intensively cooled.
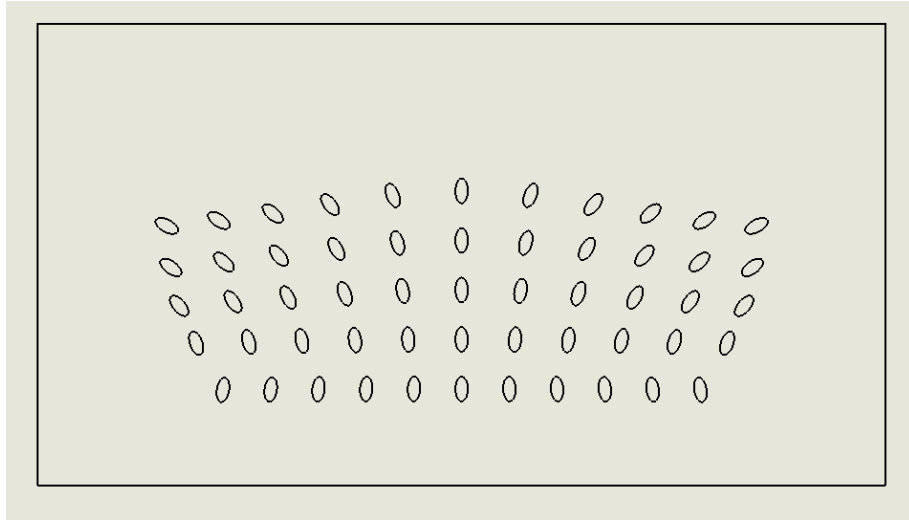


**Figure 0.26:** Swirler - Top View

### 3.4.2.6 Five Row Slot

The Five Row Slot, shown in Figure 3.27, represents a nearly ideal, full coverage film cooling case.  Slot cooling evenly distributes the coolant laterally while not being prone to separation as shown by Hartnett et al. [11].  His results showed injection through a slot at 30° maintained the mass, momentum, and energy of the flow introduced by the slot close to the wall.  The mass flow run through this cooling scheme was matched with that of the Five Row for better comparison of heat flux and wall temperature between

74

cooling configurations.  The slot height was 0.51mm and the width was 25.4mm.   While

slot cooling has excellent cooling characteristics, it suffers from its structural

impracticality in turbine applications.
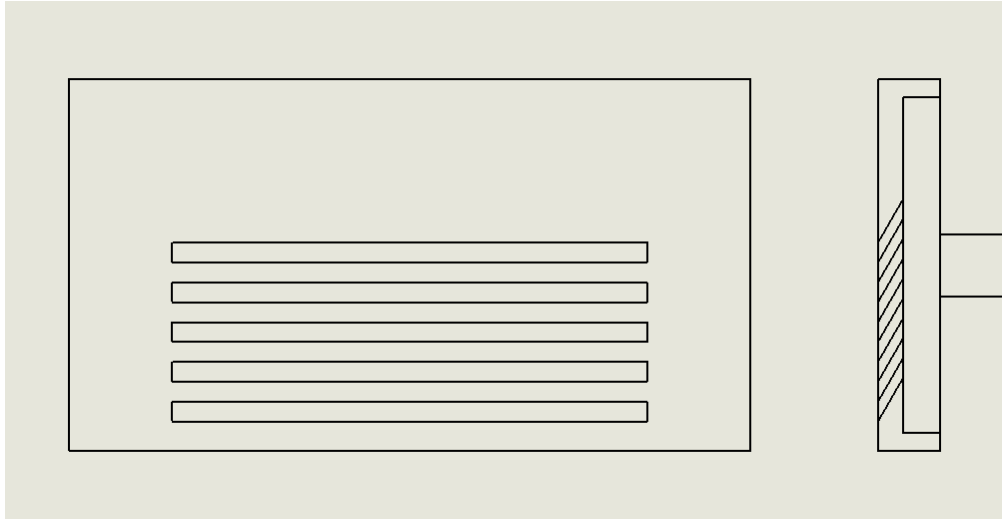


**Figure 0.27:** Five Row Slot - Top View(Left), Side View (Right)

### 3.4.2.7 Five Row Trench

In an attempt to create a more practical structure for turbine environments while

taking advantage of the benefits of slot cooling, the Five Row Trench configuration was

designed.  Trenches benefit from the diffusing process that occurs when portions of the

flow exiting the coolant holes impact the trench wall as speculated by Bunker [12].

Bunker also suggested that the vortices created by the trench wall may help to counteract

the vortices created from typical discrete film cooling jets in a cross flow. The diffusion

process is theorized to increase lateral spreading and to create a well attached film that is

not sensitive to blowing ratio.  The design of the Five Row Trench, shown in Figure 3.28,

used the hole locations of the Five Row configuration and designed a trench around them. The depth of the trenches were 0.381 mm
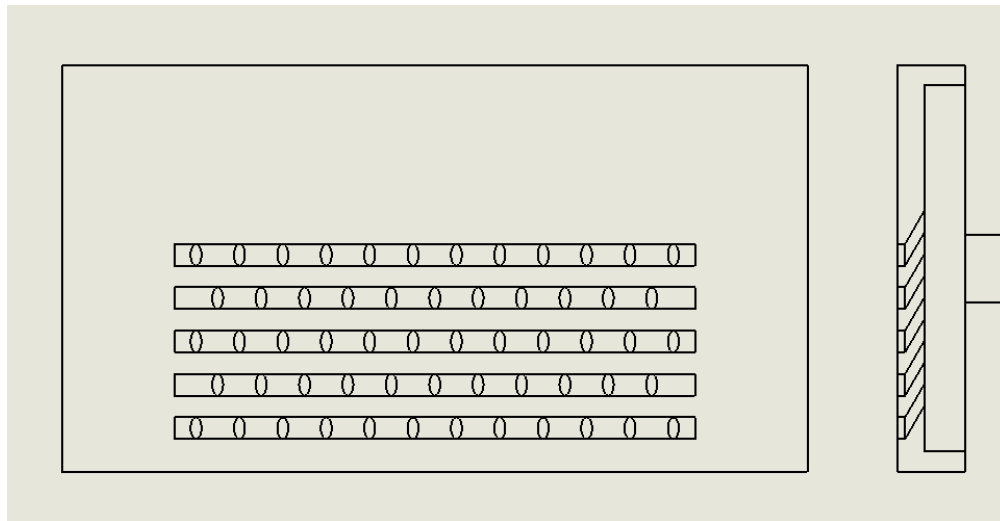


**Figure 0.28:** Five Row Trench - Side View (Left), Top View (Right)

### 3.5 Facility Fuel, Air, and Nitrogen Supply and Control

The WSR was supplied with propane, heated air, and water for cooling through the duration of experimentation. Liquid propane was stored outside of the Air Force Research Laboratories test cell 153 in 100-lb (45.4 kg) tanks (Figure 3.29). The propane tank was heated to quickly boil the propane so that the pressure required for the experiment was met. The gaseous propane passed through several regulators into the test facility, into a thermal mass flow controller and finally mixed with the heated air before passing into the WSR. The temperature and pressure of the propane were monitored to ensure consistent test conditions. The air provided to all components was provided from the facilities compressed air system. The air supplied to the WSR passed through a

thermal mass flow controller, into the combustion air heater where it is heated to 533 K, thereafter it is mixed with the propane, and finally it flows into the WSR. Both the propane and air flow rates were controlled via the control panel (Figure 3.30). Water was used to maintain the WSR's temperature below critical conditions. The mass flow rate was controlled via two 1 GPM water flow controllers where each controlled the flow of the upper and lower sections of the WSR.
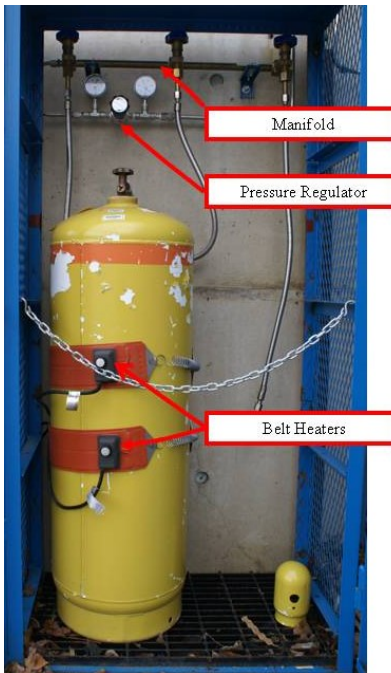


**Figure 0.29:** Propane tank, regulator, and heaters

The test section was supplied with air and nitrogen for film cooling and Mokon oil to cool the test section. The air and nitrogen were taken from facility supply and supplied the mass flow for the film cooling. For mass flows between 0-10 SLPM, the Brooks controller, shown in Figure 3.31, was used for its ability to finely control the mass

flow in these ranges.  For any flows over 10 SLPM, the Film Cooling Air and Nitrogen

Dilution mass flow controllers located on the control panel, Figure 3.30, were

implemented.  This allowed for finite control over the range of mass flow required.
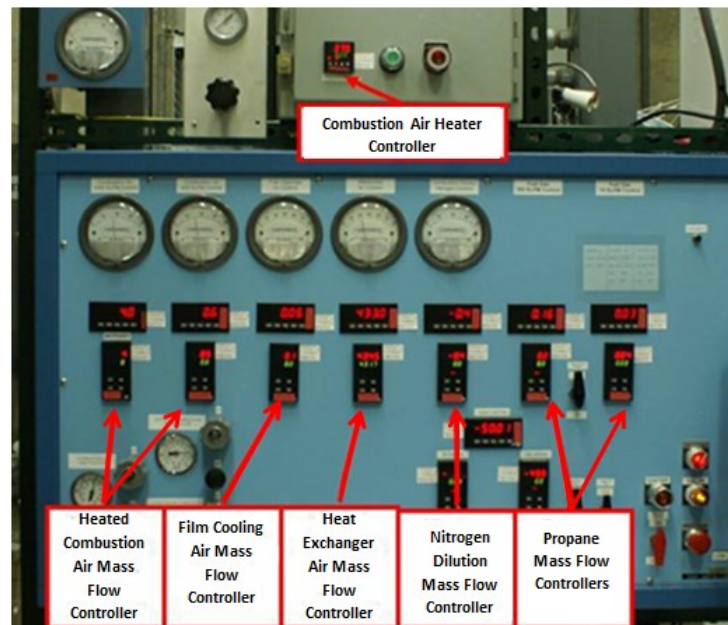


**Figure 0.30:** Control panel for fuel, air, and nitrogen



**Figure 0.31:** Brooks, 0-10 SLPM, mass flow controller for film cooling air/N2

### 3.6 Repeatability

This study examined the repeatability of measurements of wall temperature, freestream temperature, well-stirred reactor temperature, and heat flux measurements. The repeatability of these was determined by studying the variations over a single day and over all test days. The wall temperature for a set condition through a single day varied at most by 0.5%. The wall temperature over the course of testing for similar test conditions formed a 95% confidence interval around the mean of $\pm$ 5 K. This is relatively small variation compared to the wall temperatures that valued 800 K. The temperature of the combustion gasses in the well-stirred reactor varied by 0.7% throughout the day. Over the course of the entire testing period, the temperature of the combustion gases in the well-stirred reactor varied at most by 2% from the average value.
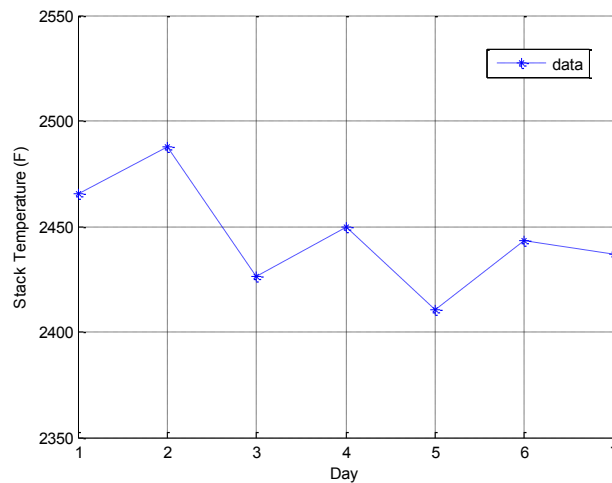


**Figure 0.32:** Repeatability of freestream temperature entering test rig.

The temperature of the gasses entering the test rig is plotted versus the test day in Figure 3.33 for a section of testing done. Day 1 represents the first day of testing where the ceramic transition was brand new and had not been tested with. Day 7 represents the end of a testing period of this thesis. During each day, similar data was collected and the rig was slowly being worn down. From Figure 3.32, it can be seen that the reactor temperature was slowly reducing in temperature as the rig was operated. This reduction in temperature is likely due to the degradation of the ceramic transition. As some of the ceramic is worn away with use, more thermal energy is leaked out the sides of the transition section. Even with this decrease in temperature the free stream gas temperature of the testing rig only showed a decrease of 3% from the beginning of testing to the end of testing providing confidence in the data quality.

# IV. Results and Analysis

This thesis' overall goal is the evaluation of various film cooling configurations on their ability to protect the wall and to consume radicals in a fuel-rich environment. This effort builds on previous results of film cooling specifically determining the interaction of multiple rows of cooling flow to reduce the heat load to a surface in the presence of a fuel rich freestream. Specifically, this investigation follows after the work of Robertson aiming to validate the trends that he showed in regards to a build-up effect that multiple rows create, while overcoming the difficulties that he encountered with measuring raw heat flux to the wall. Once this was complete, a detailed study of the Five Row configuration was performed and new performance tools of net heat flux reduction and infrared imaging were developed. The Five Row was then used as a baseline for comparison with other cooling configurations. These cooling schemes were developed to mimic both current cooling configurations and potential options for minimizing the heat load in a real world application. All configurations were evaluated based on augmentation, net heat flux reduction, emissions, flame images, and wall absorption parameter.

## 4.1    Test Plan

The initial phase of testing was focused on validating the trends found by Robertson [23] study of a build-up of rows of coolant. A newly made, modified instrumentation block was implemented to the same testing rig used by Robertson. This modified instrumentation block had slightly shifted thermocouple locations compared to

the instrumentation block of Robertson.  The new instrumentation block was designed

due to errors found within Robertson's instrumentation block concerning the distance

between thermocouples in a pair resulting in erroneous heat flux measurements.  While

augmentation is not a function of distance between thermocouple measurements, it is

important to verify the trends in augmentation shown by Robertson with more valid heat

flux measurements. The Single Row, Three Row, and Five Row cooling configurations,

described in Section 3.4.1, were tested at a range of blowing ratios from 0.5 to 3.0 at a

constant equivalence ratio and they were tested at a range of equivalence ratios from 1.1

to 1.4 at a constant blowing ratio of 2.0.  At each test condition, air cooling was injected

to test the performance of a reacting film and nitrogen cooling was injected to test the

performance of a non-reactive film.  These test conditions matched those of Robertson

and would allow for direct comparison between the two experiments.  Photographs of the

flame were taken from the side at each test condition at the same camera setting used by

Robertson, described in Figure 3.3.2.  These photographs were compared to those taken

by Robertson to evaluate the consistency of results produced between each experiment.

A detailed study of the Five Row configuration was performed to further

understand the effects of a build-up of rows of coolant.  This phase of testing focused on

improving old techniques of evaluation and developing new tools to evaluate

effectiveness.  A more detailed blowing ratio sweep and equivalence ratio sweep were

performed and evaluation of a new parameter developed by Robertson [23] called Wall

Absorption was implemented.  The procedure and calibration for implementation of an

infrared camera, described in Section 3.3.2, was derived in this phase of testing as a means to evaluate wall temperature.  Photographs of the flame were once again taken at each testing condition in conjunction with the infrared imaging.  In all, this test phase acted to develop and hone evaluation techniques that would later be used to compare multiple film cooling configurations.

The final phase of testing focused on various cooling schemes with five rows of coolant.  These cooling schemes are described in Section 3.4.2. All of these cooling schemes were tested at a range of blowing ratios from 0.5 to 3.0 at a constant equivalence ratio and they were tested at a range of equivalence ratios from 1.1 to 1.4 at a constant blowing ratio of 2.0.  These cooling configurations were evaluated based on heat flux, augmentation, net heat flux reduction, emission spans, infrared imaging, flame visualization, and wall absorption.  These configurations were all compared to a common baseline of the Five Row configuration.

## 4.2    Surface Temperature Uniformity

A key problem in previous research had been non-uniformity of temperature spanwise across the instrumentation block due to the swirl from the WSR. Bohan et al. [3] and Robertson [23] mitigated this problem through addition of a flow straightener as described in Section 3.2.  Robertson's surface temperature uniformity data showed up to 22K variation from left to right at $X/D = 7$.  In order to further mitigate spanwise non-uniformity, two flow straighteners were attached together and mounted inside the transition section.  Figure 4.1 shows the surface temperature uniformity of the

83

Five Row configuration with Φ = 1.175 and no film cooling present. The largest

variation in temperature was 12K (1.5% variation). This result is nearly a 50%

improvement over Robertson's results as a result of removing additional swirl from the

flow. Interestingly, *X/D* = 17 and *X/D* = 22 showed a higher calculated surface

temperature of around 15K compared to *X/D* = 10 and *X/D* = 30 for this test case. This is

likely the streamwise thermal gradient present due to the backside cooling present in the

upper cooling path of the testing rig that appears above the instrumentation block and the

cool film cooling plenum that appears below the instrumentation block. The backside

cooled wall and the film cooled plenum created two cold temperature boundaries around

the instrumentation block. Because the 17D and 22D are at the interior of the

instrumentation block, their temperature remains higher than the outer edges.
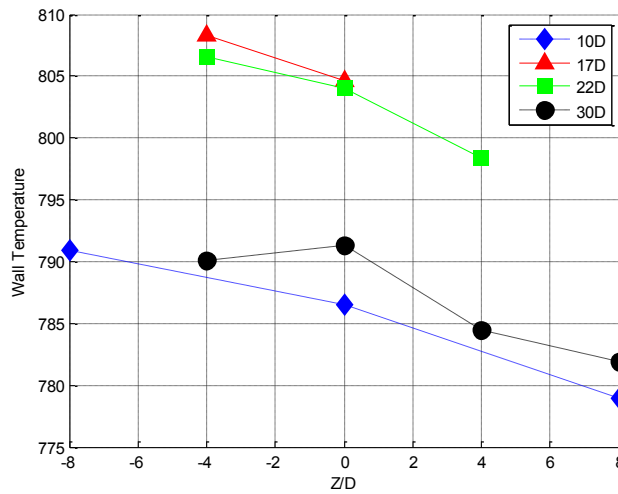


**Figure 0.1:** Surface Temperature Uniformity

### 4.3    Layer Build-Up Campaign Analysis

Robertson [23] preformed a study on the effects of a build-up of rows of cooling holes on the downstream effectiveness. Robertson evaluated the Single Row, Three Row, and Five Row cooling configurations described in Section 3.4.1. The purpose of these designs was to evaluate the feasibility of building a substantial layer of attached coolant beneath a burning layer of coolant.   However, due to various design flaws within the instrumentation block implemented by Robertson, the locations of the thermocouples in each pair were not precisely known which caused errors in the calculations of heat flux and augmentation. An improved instrumentation block was developed as discussed in Section 3.3.1 and Robertson's study was repeated. The goal of this section is to evaluate the validity of the trends seen in Robertson's Layer Build-Up Campaign on the effects of a build-up of rows of coolant coupled with more accurate values of the actual heat flux.

Robertson [23] preformed two different studies on the configurations stated above. The first study was a blowing ratio sweep where the blowing ratio was varied between 0.5 and 4.0 at a constant equivalence ratio of 1.175. To evaluate the trends shown in this study, this thesis preformed a similar blowing ratio sweep study where then blowing ratio was varied between 0.5 and 3.0 at a constant equivalence ratio of 1.3. The second study was an equivalence ratio sweep where the blowing ratio was held constant at 2.0 and the equivalence ratio was varied from 1.1 to 1.4. To evaluate the trends shown in Robertson's equivalence ratio sweep study, this thesis preformed a similar study where the $1.1 \leq \Phi \leq 1.3$ at a constant $M = 2.0$. Visible spectrum photographs were taken at each

85

test case and will be compared when applicable to Robertson's visible spectrum photographs.

### 4.3.1   Blowing Ratio Sweep

The goal of this section is to examine the differences found between Robertson's [23] data and the data obtain by the author.  Specifically, the issue was the values of the heat flux found initially by Robertson. His heat flux values ranged from 40,000 to 60,000 W/m$^2$ which was significantly less than the expected range.  As discussed in Chapter 3, the distance between his thermocouple pairs was in error.  Therefore, the test conditions of Robertson were repeated with the new instrumentation block.  Figure 4.2 shows heat flux values that ranged from 140,000 to 240,000 W/m$^2$.  The Five Row with air cooling experienced heat flux values varying from 210,000 W/m$^2$ at M = 0.5 reducing down to 165,000 W/m$^2$.  With nitrogen cooling, the Five Row experienced at maximum 145,000 W/m$^2$ indicating there is additional heat flux due to secondary reactions for air cooling.  This trend of increased heat flux of air cooling over nitrogen can be seen at all blowing ratios tested for all three configurations indicating secondary reactions are occurring for all configurations when cooled with air.

Each configuration was also run with no cooling.  The no cooling case is plotted on Figure 4.2 as a black line and resulted in a heat flux of 172,500 W/m$^2$.  The goal of film cooling is to reduce the heat flux to the wall so the target is to keep heat flux values below the black line.  For nitrogen cooling, all configurations across all blowing ratios showed reduced heat flux to the wall compared to the no cooling case.  For air cooling,

86

on the other hand, only the Five Row showed a reduction of heat flux to the wall from M = 1.5 to M = 3.0. The Single Row and Three Row configurations fail to protect the wall as the heat flux produced across all blowing ratios was higher than the no cooling case.
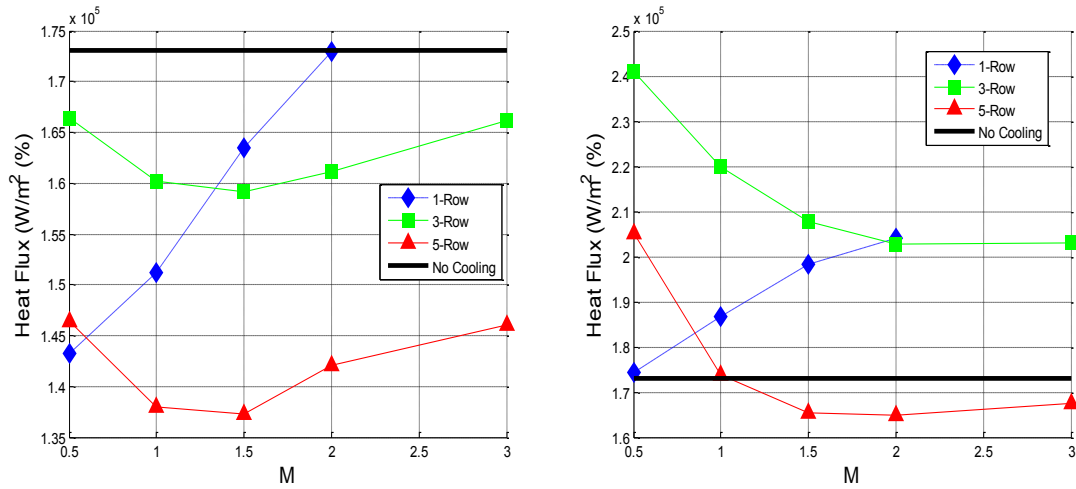


**Figure 0.2:** Shewhart - Heat Flux Measurements Nitrogen Cooling (Left);

Air Cooling (Right); $\varphi = 1.3$, $X/D = 22$

Robertson understood that his actual heat flux levels were erroneous, therefore he focused on the trends in augmentation because augmentation is only a function of the temperature difference between thermocouples at each location. The augmentation results for Robertson's blowing ratio sweeps are compared with the results of the current investigation. The average augmentations are presented for the row of thermocouples at the specific downstream location. Figures 4.3 and 4.4 show Robertson's and the author's results at $X/D = 7$ and $X/D = 10$. These downstream measurement locations varied

because of the modification of the instrumentation block made by the author to solve the problems experienced by Robertson. Robertson showed an unintuitive result at this location where the Single and Three Row configurations have negative augmentations for blowing ratios of 0.5 to 3.0 suggesting that air cooling performed better than nitrogen cooling. This result was likely due to thermocouples within the instrumentation block being out of their proper position and thus forming errors in the calculations. Robertson also showed increasing augmentation with increasing blowing for the Three Row and the Five Row. This result would indicate that the configuration is failing to protect the wall with increasing mass flow.
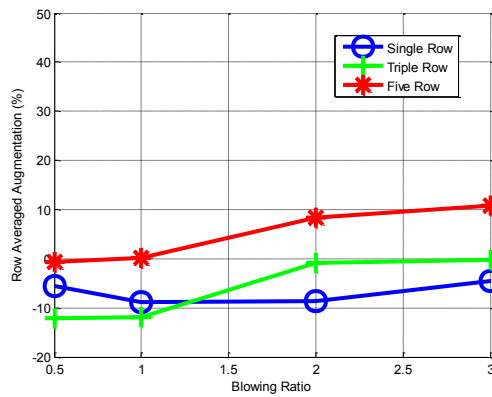


**Figure 0.3:** Robertson, σ vs. M, $X/D = 7$      **Figure 0.4:** Shewhart, σ vs. M, $X/D = 10$
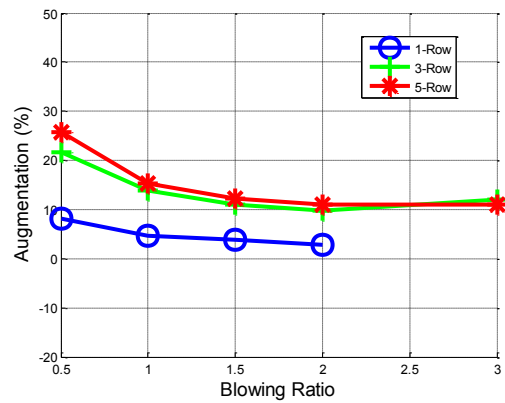
The trends at $X/D = 7$ discussed by Robertson were not seen in the results produced in the current study. All augmentations produced by the author were positive suggesting that air cooling always produced worse results than the nitrogen cooling cases.

In order to understand why such fundamental differences were seen at this location, a comparison of the flames images produced by each configuration is required.

Photographs of the flame produced by all three configurations taken at $\varphi = 1.175$ and M = 2.0 by Robertson [23] are displayed in Figure 4.5. Current photographs are shown in Figure 4.6. These photographs were then enhanced and evaluated based on the procedure developed by Robertson that is described in Section 3.3.2. These photographs allow for evaluation of where the flame is occurring and some insight on the trends in augmentation seen. The flame images produced by Robertson and by this investigation look the same for all three configurations tested. Therefore, the chemistry has not changed between each experiment. A table of the flame lengths for each data set is provided in Table 4.1. The white lines near the flames on Figures 4.5 and 4.6 indicate either the start or end of the flame. These lines were placed based on 5% of the maximum blue value for the beginning of the flame and 10% of the maximum blue value for the end of the flame. The flame length was then determined by calculating the distance between these two lines. This method for determining the flame length was developed by Robertson [23].
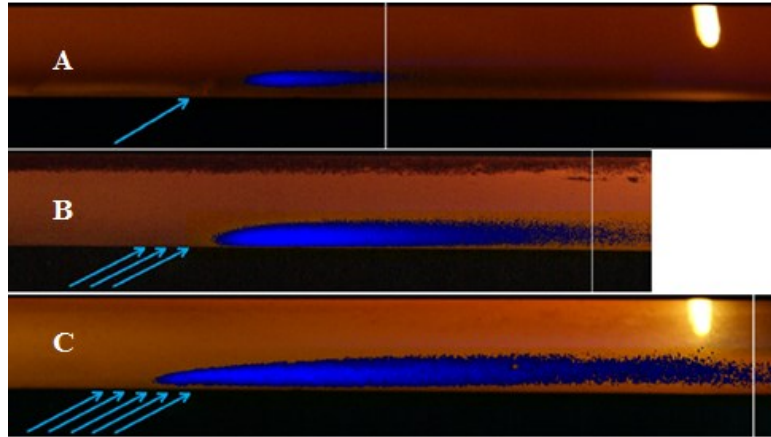
**Figure 0.5:** Robertson: Flame Images; A - Single Row, B - Three Row; C - Five Row,
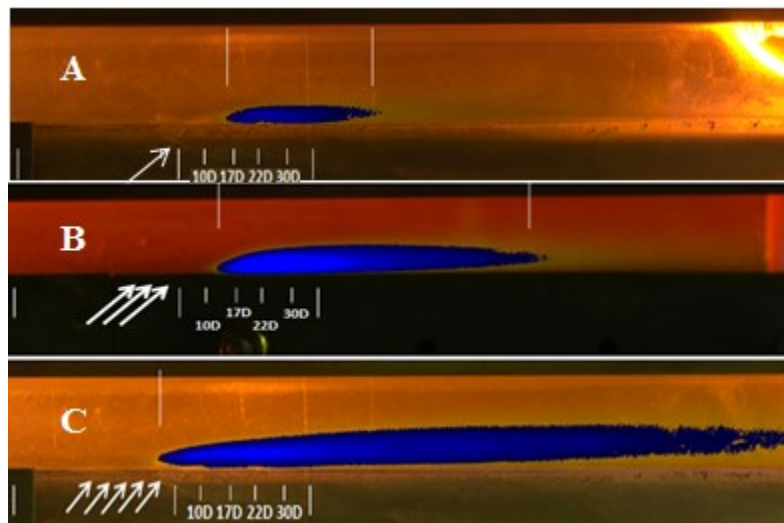
φ = 1.175, M=2.0



**Figure 0.6:** Shewhart: Flame Images; A - Single Row, B - Three Row; C - Five Row,

φ = 1.175, M=2.0

The calculated flame lengths were similar for all configurations. The difference in flame length is likely a result of differing cameras combined with the process used to enhance the image. However, even with the small difference in flame length, the starting location and general shape of the flame produced by all three cooling schemes are the same between the two data sets. The Single Row produced the shortest flame for both data sets with a length of about 30 diameters. The Single Row produced a thin flame that was located close to the wall and began around $X/D = 17$. This late starting location explains the low augmentation of 3% at the 10 diameter location (Figure 4.3) because the flame had not formed at this location yet. Compared to the Three Row and Five Row, the Single Row produced the dullest flame which corresponds with its low potential heat release.

**Table 0.1:** Flame Length Results

| | Flame Length (D) | | |
| --- | --- | --- | --- |
| | Single Row | Three Row | Five Row |
| Robertson | 28 | 72 | 138 |
| Shewhart | 33 | 70 | 145 |

The Three Row produced a much taller, further off the wall, and longer flame compared to the Single Row. Having three times the mass flow as the Single Row for an equivalent blowing ratio, the length of the flame and thickness of the flame are expected to increase. The intensity of the flame produced by the Three Row was the greatest of all three configurations and the highest intensities of the flame were located between $X/D =$

15 and $X/D = 40$.  This increased heat release is seen in the augmentation analysis in Figure 4.6 and 4.8 where the Three Row had the highest augmentation by a minimum of 5% augmentation.  The flame created by the Three Row started at the 10 diameter location which was ahead of the starting location of the Single Row.   This result was caused by the earlier injection of coolant from upstream rows.

The Five Row produced the longest flame of all three configurations at 145 D long and formed at the last row of cooling holes.  This long drawn out flame spread the intensity of the secondary reactions over four times the length of the single row. However, the reacting film separated from the wall around $X/D = 30$ and a non-reactive layer grew with downstream distance.  Therefore the overall augmentation of the surface heat flux was low.  It is hypothesized that coolant from the initial few rows buffered the hot gases away from the wall and minimized a downstream reaction with the final rows of coolant.  This allowed the cooling film from the later rows to remain attached to the wall and exist in a region of flow with fewer reactive species.

Looking at the augmentation results for the three cases reveals how the flame locations impacted the heat flux augmentation. The results for Robertson, at $X/D = 15$, can be seen in Figure 4.7 and the author's results, at $X/D = 17$, are shown in Figure 4.8. Robertson showed a decrease in heat flux augmentation with increasing mass flow. Robertson showed the Five Row performing the best of all configurations across all blowing ratios.   The Three Row configuration displayed the worst performance of all configurations at this location.  This result was attributed to the fact that the second row

of the Three Row was spanwise from the first and third rows and as such the second row was unprotected from freestream radicals by upstream rows. Also the Three Rows increased mass flow translates to higher potential heat release compared to that of the Single Row. The combination of these two factors made the Three Row non-optimum. The trend of the Three Row and the Five Row configurations are very similar with the Five Row having lower augmentation, indicating that a build-up of rows is helping to protect the wall at this location.
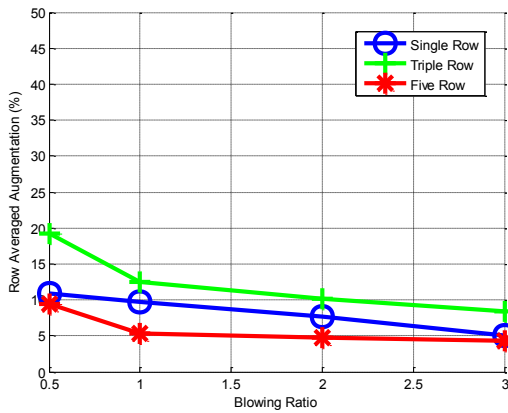


**Figure 0.7:** Robertson, σ vs. M, *X/D* = 15    **Figure 0.8:** Shewhart, σ vs. M, *X/D* = 17
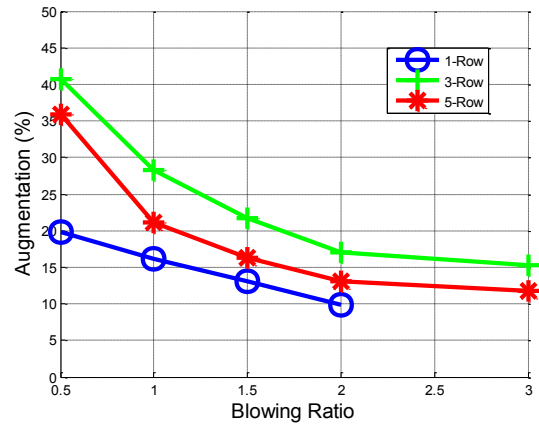
The augmentation levels for the current study are higher than those seen by Robertson. This is due to the difference of equivalence ratio. As will be discussed in Section 4.3.2, as equivalence ratio increases the augmentation increases. The current results came to the same general conclusions as Robertson when comparing the fifteen and seventeen diameters downstream locations. All configurations showed a decrease in augmentation as the mass flow was increased. The Three Row configuration performed

93

the worst of all configurations.  The Single Row for the current study shows lower augmentation than the Five Row. Examining Figure 4.6, the flame produced by the Single Row shows that the flame does not begin until around the $X/D = 17$ mark.  This would result in lower augmentation at this downstream location for the Single Row than the Five Row.

The trends seen at $X/D = 15$ continue at $X/D = 20$ for both studies shown in Figures 4.9 and 4.10.  All configurations follow the same pattern of decreasing augmentation with increasing blowing ratio.   The augmentation for each configuration has increased at this further downstream location consistent with the more intense flame and higher gas temperature. The differential augmentation between the Three Row and the Five Row has grown between the $X/D = 15$ and $X/D = 20$.  This indicates that the Five Row is more effective at protecting the wall farther downstream than the Single Row and the Three Row. One caveat to this conclusion is that the Single Row outperformed the Five Row configuration in the blowing ratio sweep analysis based solely on augmentation alone.  This result is unintuitive and when examining the heat flux, seen in Figure 4.2, it can be seen that the Five Row configuration outperforms the Single Row for all blowing ratios except $M = 0.5$.  This shows that augmentation alone does not give the full story on how well a configuration performs.  As such additional parameters must be considered to correctly evaluate the effectiveness of a cooling schemes and not augmentation alone. These additional parameters will be discussed in more detail in Section 4.4.
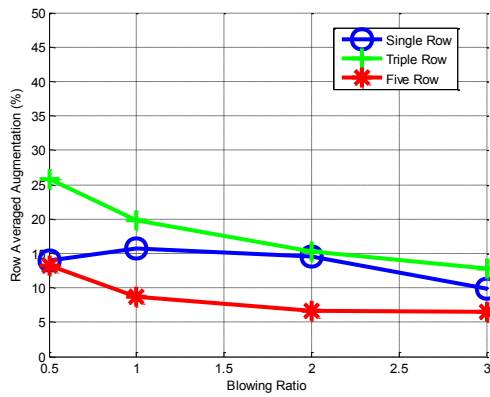
**Figure 0.9:** Robertson, σ vs. M, *X/D* = 20     **Figure 0.10:** Shewhart, σ vs. M, *X/D* = 22
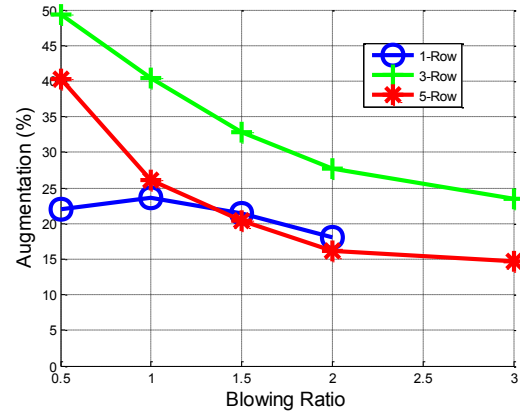
The general trends seen at *X/D* = 22 continue at *X/D* = 30 shown in Figure 4.11. The value of augmentation for each configuration has slightly decreased from *X/D* = 22 to *X/D* = 30.
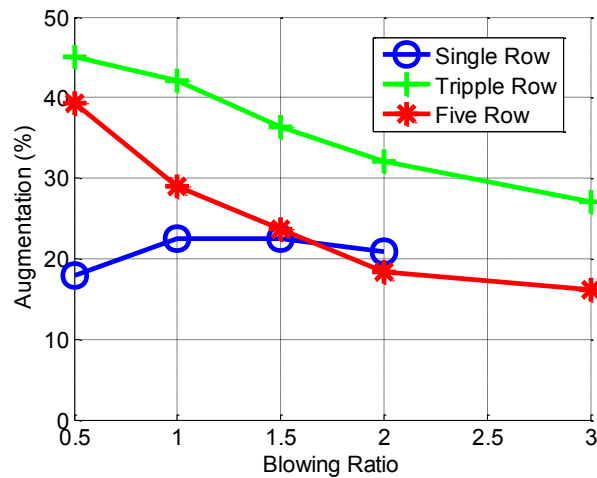


**Figure 0.11:** Shewhart, σ vs. M, *X/D* = 22

### 4.3.2 Equivalence Ratio Sweep

The results of Robertson's equivalence ratio sweeps are shown in Figures 4.12, 4.14, and 4.16 and the results of the current investigation's equivalence ratio sweeps are shown in Figures 4.13, 4.154, and 4.17. The augmentations are once again presented as average augmentations for the row of thermocouples at the specific downstream location. Figures 4.12 and 4.13 show Robertson's and the current results at seven and ten diameters downstream of the injection point, respectively. For the Single and Three row configurations, Robertson showed negative augmentation at all equivalence ratios with a trend of decreasing augmentation as equivalence ratio was increased. The trends of the Single and Three Row again are inconsistent with expected results as they state that air cooling is increasingly performing better than nitrogen as more unconsumed radicals are introduced to the system. The Five Row configuration showed increasing augmentation to an equivalence ratio of 1.2 then a decrease in augmentation with further increase in equivalence ratio.
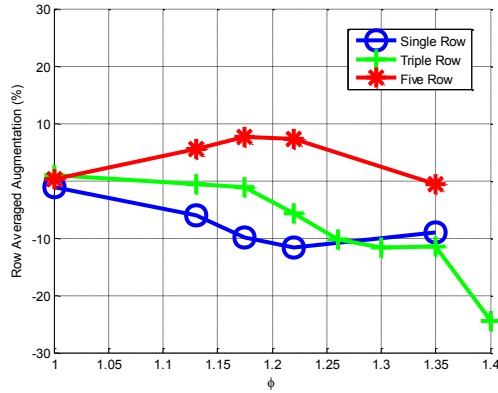
**Figure 0.12:** Robertson, σ vs. φ, $X/D = 7$      **Figure 0.13:** Shewhart, σ vs. φ, $X/D = 10$
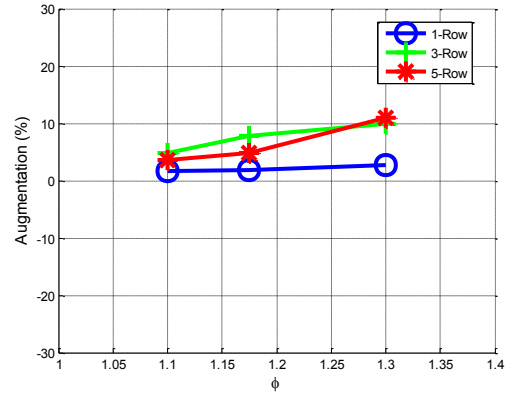
The current results show a more realistic set of trends at the ten diameter downstream location. Unlike the results shown in Figure 4.11, the Single Row and Three Row configurations have positive augmentations with trends of increasing augmentation with increasing equivalence ratio. A richer equivalence ratio yields more available radicals to mix and react with the coolant resulting in a higher potential heat release in the local downstream location resulting in elevated heat flux augmentation. This topic is discussed in further detail in Section 4.3.3. The Five Row configuration follows the same pattern as the Single Row and Three Row configurations in having a positive augmentation with increasing augmentation as equivalence ratio increases.

Proceeding to the $X/D = 15$, similar trends were found between Robertson's data (Figure 4.14) and the current investigation (Figure 4.15) at $X/D = 10$ location. All heat flux augmentations at this location were positive indicating that air cooling performed worse than nitrogen cooling. For all three configurations, augmentation increased as

97

equivalence ratio increased.  The only exception to this trend was the Single Row that

decreased in augmentation at an equivalence ratio of 1.225.  It can be seen in both data

sets, that as equivalence ratio goes to one, the augmentation is going to zero.  This trend

is intuitive because at an equivalence ratio below one there should be no difference in the

cooling between air and nitrogen.
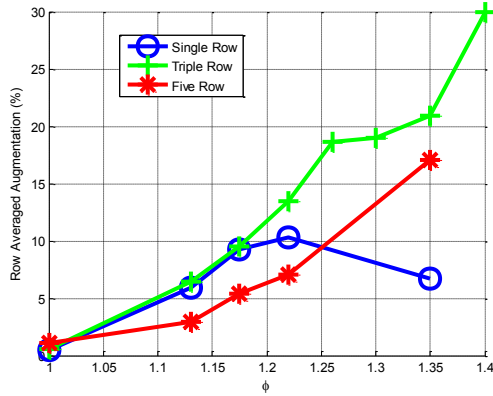


**Figure 0.14:** Robertson, σ vs. φ, $X/D = 15$          **Figure 0.15:** Shewhart, σ vs. φ, $X/D = 17$
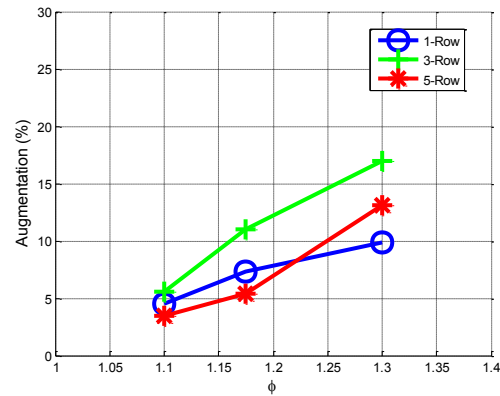
The trends shown at the $X/D = 15$ continue at $X/D = 20$.  Augmentation once

again increases almost linearly with equivalence ratio and the slope at this location

appears to have increased over the previous downstream location.  All augmentation

values are once again positive meaning that air cooling performs worse than nitrogen

cooling.  At this location, Robertson did not show the Single Row peaking in magnitude

at an equivalence ratio of 1.25.  Instead, the Single Row continued to increase but at a

slightly lower rate suggesting a peak in augmentation at a higher equivalence ratio.   In

fact, the Single Row does have a peak augmentation at a higher equivalence ratio and this

result is discussed in Section 4.3.3.  It is also suggested that the Three Row and Five Row would also experience a peak in augmentation at a higher equivalence ratio than the range tested.
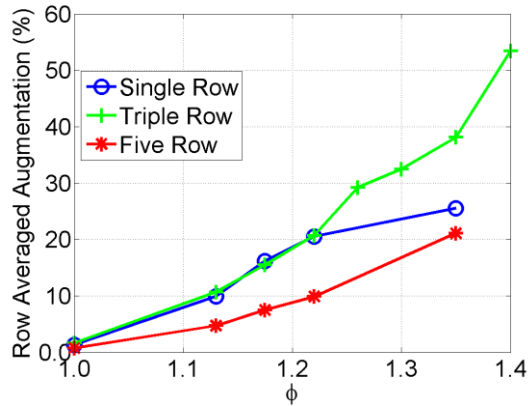


**Figure 0.16:** Robertson, σ vs. φ, $X/D = 20$    **Figure 0.17:** Shewhart, σ vs. φ, $X/D = 22$
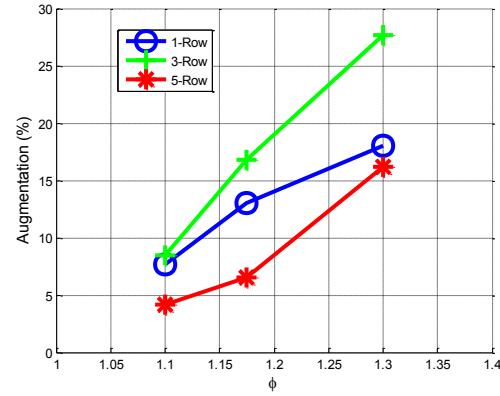
The trends shown by this thesis at the $X/D = 17$ and $X/D = 22$ diameters downstream locations match the trends found by Robertson at $X/D = 15$ and $X/D = 20$. Robertson's data showed that the Five Row configuration provided the most effective coverage downstream in terms of augmentation as a function of blowing ratio.  Robertson concluded that a wall could be sufficiently cooled in a fuel-rich environment through the build-up of multiple rows of cooling holes.

The general trends seen at $X/D = 22$ continue at $X/D = 30$ shown in Figure 4.18. The value of augmentation for each configuration has slightly increased from $X/D = 22$ to $X/D = 30$.
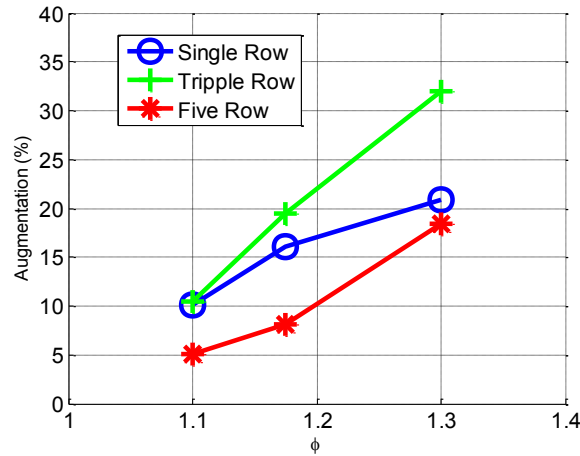
**Figure 0.18:** Shewhart, σ vs. φ, *X/D* = 30

### 4.3.3 Detailed Equivalence Ratio Sweep Study of the Single Row

A detailed study of augmentation as a function of equivalence ratio for the single row of cylindrical holes is shown in Figure 4.19. In this figure, M = 1.0 was represented by solid symbols and M = 2.0 was represented by open symbols. Augmentation increased at each downstream location with equivalence ratio as more radicals became available to be burned. Each location experienced a peak in augmentation occurring around an $\phi = 1.35$. This is consistent with previous work of Bohan et al. [3] due primarily with the reduction in freestream temperature as the equivalence ratio increased coupled with the available oxygen from the cooling rows. As the available freestream radicals increased, the local equivalence ratio would also increase and thus the flame temperature of the secondary reaction would also decline. These factors cause the additional heat flux due to secondary reactions to decrease. Furthermore, these factors cause the peak and subsequent decline in augmentation as equivalence ratio increases.

100

The magnitude of the peak in augmentation was affected by the blowing ratio. At the locations closer to the cooling holes, increased augmentation occurred at the lower blowing ratio of 1.0 over a blowing ratio of 2.0. This is in contrast to Bohan et al.'s work which showed increased augmentation for $M = 2.0$ was greater than $M = 1.0$. However, that data was taken further downstream when the reaction had time to initiate. At the $X/D = 30$, the augmentation for $M = 1.0$ and $M = 2.0$ were nearly identical suggesting that the trends are likely to reverse at further downstream locations, consistent with the work by Bohan et al. Physically, the lower M flow will remain closer to the wall thus it is not surprising that near the injection location the increase heat flux is higher for this case over $M = 2$. However, because $M = 1.0$ has half the mass flow of $M = 2.0$, the oxygen supply is consumed more rapidly and thus the potential heat release decreases more rapidly as the flow proceeds downstream resulting in lower heat flux augmentation far downstream.
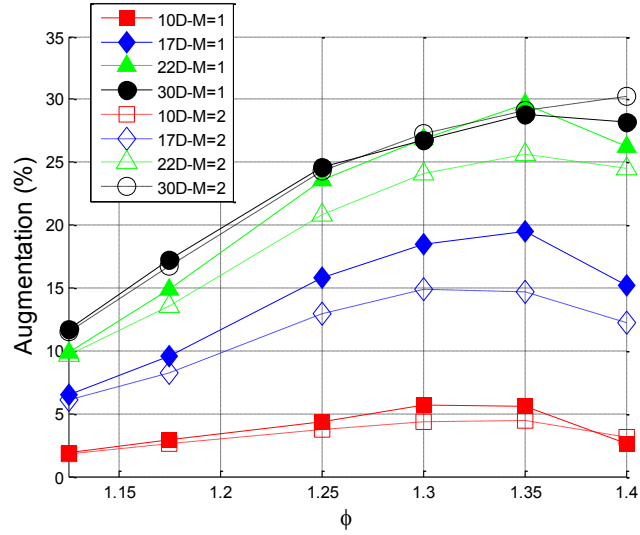
**Figure 0.19:** Single Row - Augmentation vs. Equivalence Ratio: Solid symbols are for M=1, Open Symbols represent M=2.

Figure 4.19 also shows a trend of increasing augmentation with increasing downstream distance. At $X/D = 10$, the single row configuration has a peak augmentation of around 5%. This augmentation is considerably high for a region where a substantial flame has yet to form as shown by the flame image of Figure 4.6. The level of augmentation rises quickly as the flame intensifies. Peak augmentation upwards of 25% is experienced by $X/D = 22$. These results show that the single row configuration was unable to protect the wall from secondary reactions.

## 4.4  Five Row Cylindrical Hole Cooling Scheme

This section will discuss the heat flux, augmentation, and net heat flux reduction (NHFR) as functions of blowing ratio and equivalence ratio and evaluate the Five Rows

ability to protect the wall. Additionally, an examination of an emissions sweep will provide insight on the consumption of radicals as a function of distance from the film cooled wall. Finally, evaluation of infrared images and visible spectrum photographs as well as wall absorption parameter will give insight to where heat release occurred and how it impacted the film cooled wall. Overall the goal of this section is to provide a detailed evaluation of the Five Row's ability to protect the wall while consuming freestream radicals that can be used as a baseline for comparison in other cooling configurations.

### 4.4.1   Five Row – Impact of Blowing Ratio on Heat Flux, Net Heat Flux Reduction, and Augmentation

A blowing ratio sweep and equivalence ratio sweep were performed on the Five Row and heat flux and augmentation were evaluated. The blowing ratio sweep test was performed at a constant equivalence ratio of 1.3 and the blowing ratio was varied from 0.5 to 3.0. The equivalence ratio sweep varied $1.1 \leq \varphi \leq 1.3$ at a constant blowing ratio of 2.0.

An evaluation of the heat flux and net heat flux reduction was performed for the blowing ratio sweep. Net heat flux reduction is a non-dimensional parameter described in Section 2.2.1 that allows for comparison between heat flux with cooling and without cooling. At each downstream location, NHFR was calculated and plotted versus blowing ratio for both air and nitrogen cooling. Heat flux and NHFR at each downstream location is presented in Figures 4.20, 4.21, 4.22, and 4.23 as a function of blowing ratio. The heat

flux results of nitrogen cooling are plotted as solid blue diamonds, air cooling as solid red squares, and no cooling as solid black circles are shown in each figure. The NHFR results of nitrogen cooling are plotted as open blue diamonds and air cooling as open red squares.

At the $X/D = 10$, the addition of coolant reduces the heat load to the surface. The biggest difference in heat flux between the air cooling and the nitrogen cooling was the largest at a $M = 0.5$. The small amount of mass flow at this blowing ratio causes the flame to be anchored to the wall causing increased heat flux. The nitrogen and air cooling produced a trend of decreasing heat flux down to a minimum of $M = 1$ for nitrogen and $M = 1.5$ for air and then increasing heat flux with increasing blowing ratio. The cause of this trend is likely the coolant separating from the wall around a $M = 2.0$. At this location, air cooling protects the wall more efficiently than no cooling but secondary reactions increased the heat flux to the wall for all blowing ratios. The optimal blowing ratio for this location is $M = 1.5$ because it produces the lowest heat flux for air cooling with the smallest differential in heat flux between nitrogen and air.

The trend in NHFR for nitrogen and air coolant is positive across all blowing ratios. Positive NHFR indicates that both the air and nitrogen reduce the heat flux to the wall compared to not cooling the wall. Nitrogen cooling has a larger, positive NHFR than air cooling meaning that it reduces the heat flux to the wall more effectively than the air cooling. Both the air and nitrogen cases increased in NHFR up to a maximum and then decreases with increasing blowing ratio. The small difference of 0.07 NHFR

104

between the air and nitrogen cooling along with the positive NHFR suggests the air cooling is providing adequate protection to the wall through the formation of a non-reacting layer.
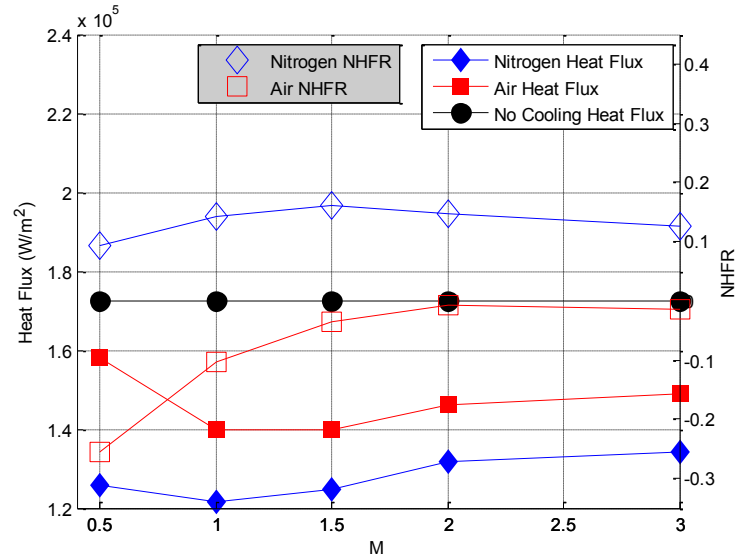


**Figure 0.20: Five Row** – Heat Flux and NHFR vs. Blowing Ratio, $\varphi = 1.175$, $X/D = 10$

Continuing to $X/D = 17$, both nitrogen and air follow the same trend of decreasing heat flux to a minimum and then increasing augmentation as seen at $X/D = 10$. Both nitrogen cooling and air cooling experienced an increase in heat flux across all blowing ratios and the difference between nitrogen and air has increased from $X/D = 10$. At a blowing ratio of 0.5, cooling with air resulted in an increased heat flux over the no cooling case. This result is contrary to the purpose of film cooling and it would be better to not film cool the wall at all than to run at M = 0.5. For all other blowing ratios, air cooling was able to reduce the wall temperature over the uncooled case but the difference

105

in heat flux at this location decreased. This trend indicates that the ability of the Five Row to protect the wall diminishes with downstream distance and is likely caused by the additional heat released by the coolant interaction with the freestream radicals resulting in an increase in the film temperature.
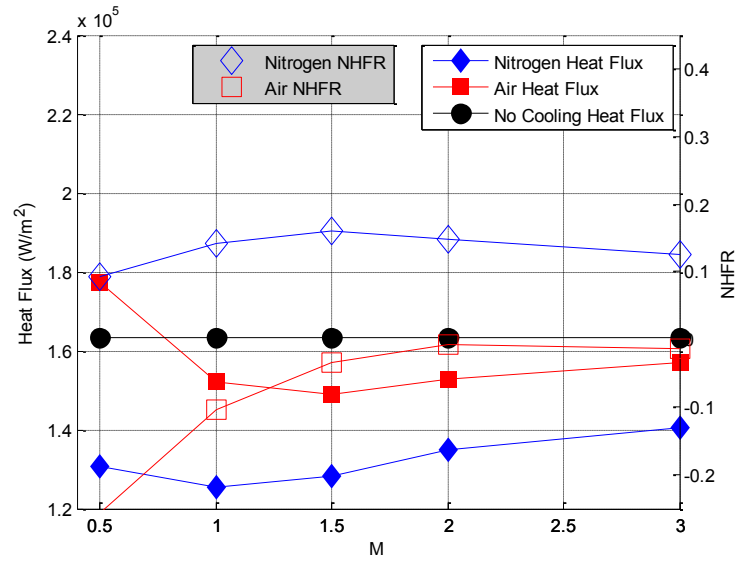


**Figure 0.21: Five Row** – Heat Flux and NHFR vs. Blowing Ratio, $\varphi = 1.175$, *X/D* = 17

Both air and nitrogen cooling show a significant decrease of at least 0.1 NHFR at all blowing ratios. Air cooling at M = 0.5 showed the biggest reduction in NHFR of 0.2 down to -0.1. Negative NHFR means the air coolant failed to protect the wall at this location and even added additional heat flux over the uncooled case. The difference between air cooling and nitrogen cooling NHFR increased at this location compared to *X/D* = 10. This result matches the increase in heat flux.

The trends seen at $X/D = 17$ continue at X.D = 22.  The heat flux of the nitrogen

and air cooling increased once again and the difference between air and nitrogen further

increased.  This increase is attributed to the continued consumption of radicals as seen in

the flame visualization in Figure 4.34.   The heat flux at M = 0.5 for air cooling increased

by a large amount and was 30,000 W/m$^2$ above the no cooling case.  At M = 1.0, air

cooling produced the same heat flux as the no cooling case.  This means that it would be

better to not cool the wall than to run with blowing ratios less than 1.0.    These trends

show that the effectiveness of the Five Row to protect the wall downstream of the cooling

holes is decreasing at this location.
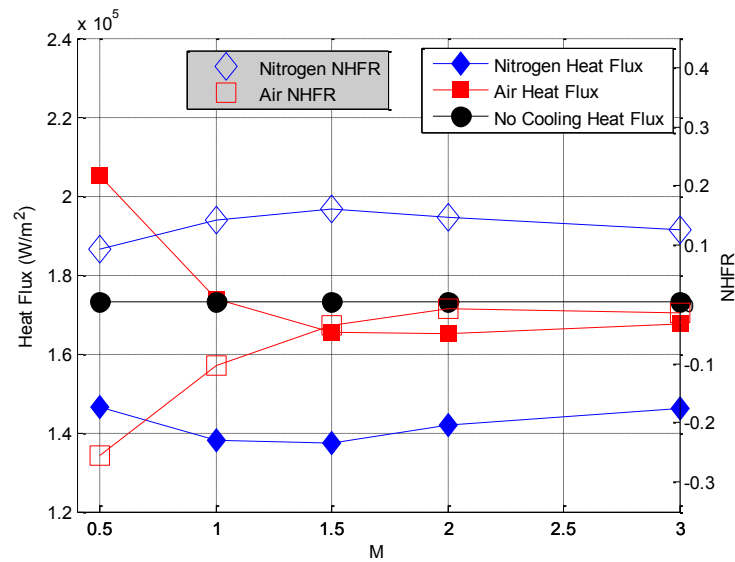


**Figure 0.22:** Five Row – Heat Flux and NHFR vs. Blowing Ratio, φ = 1.175, $X/D = 22$

Further reduction of NHFR occurs for air cooling at $X/D = 22$.  At M = 0.5,

NHFR reduced to -0.2 and at a blowing ratio of 1.0, NHFR was zero for air cooling.  This

107

shows that air cooling is failing to protect the wall at this downstream location for

$0.5 \leq M \leq 1.0$. Nitrogen cooling continued to decrease in NHFR with downstream

distance. The trend of NHFR with respect to blowing ratio began to flatten out at this

downstream location.
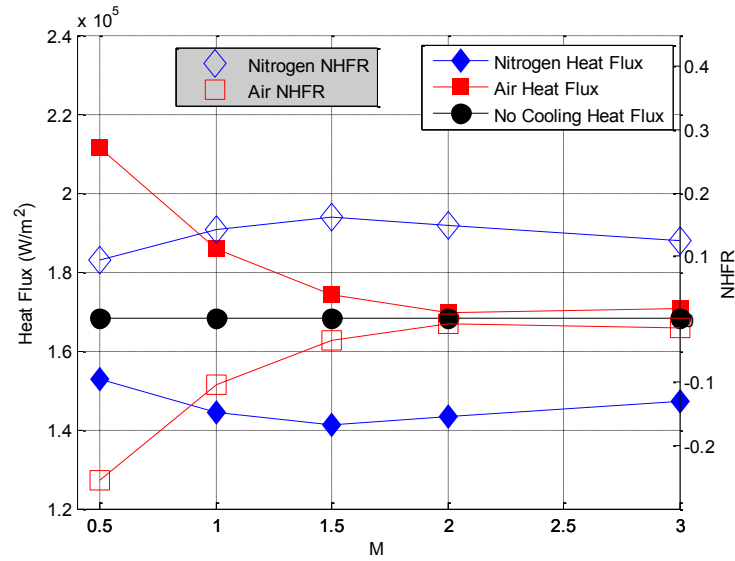


**Figure 0.23: Five Row –** Heat Flux and NHFR vs. Blowing Ratio, $\varphi = 1.175$, *X/D* = 30

The trends of the *X/D* = 17 and *X/D* = 22 continue at *X/D* = 30 as seen in Figure

4.22. NHFR continues to decrease and the difference in NHFR between air and nitrogen

continues to increase with downstream distance. For all blowing ratios, air cooling

resulted in negative NHFR. This result indicates that the Five Row is no longer

protecting the wall using air as a coolant at this location. For $0.5 \leq M \leq 2.0$, the Five

Row is performing worse than if the wall was not cooled at all. In order to continue

using air as a coolant, additional rows of coolant must be added upstream of $X/D = 30$ to resupply the cool, non-reacting layer formed next to the wall.

Nitrogen and air cooling continue to show increased heat flux at all locations and the difference between the two continues to increase. Air cooling at all blowing ratios produced greater or equal heat flux to that of the no cooling case. This shows that the Five Row configuration with air cooling fails to protect the wall at all at this downstream location and likely further downstream locations. In order to continue protecting the wall with air as a coolant, additional rows of coolant would have to be added before the $X/D = 30$ to maintain the heat flux below that of the no cooling case. This suggests that the coolant needs to be continually refreshed downstream to continue to provide a benefit in a reactive environment. While creating the initial layer of film can protect the wall for a while, reactions continue to occur within the film, consuming the oxygen. This investigation suggests that 5 rows can withstand this process for 22 downstream diameters as M > 1.0 and about 30 diameters for M > 2.0.

The augmentation results of a blowing ratio sweep for the five row configuration with $\phi = 1.3$ are shown in Figure 4.24. The data is presented as augmentation with averaged values reported at each downstream location. It was found that as blowing ratio increased the augmentation decreased and eventually levels off to a constant low value. Augmentation was shown to increase with downstream distance. This result was seen in the heat flux data as the difference in heat flux between nitrogen and air increasing with downstream distance. A maximum augmentation of 40% was found at $X/D = 22$ with

*M* = 0.5. The maximum augmentation for each configuration was found at M = 0.5, indicating that *M* = 0.5 is not sufficient to fully protect the wall. A minimum augmentation of around 10% was measured at *X/D* = 10 over a wide range of blowing ratios. The small variation in augmentation within the range of $2.0 \leq M \leq 3.0$ shows that adding even more mass flow to this system would achieve negligible reduction of heat flux to the wall as the wall was already well protected.
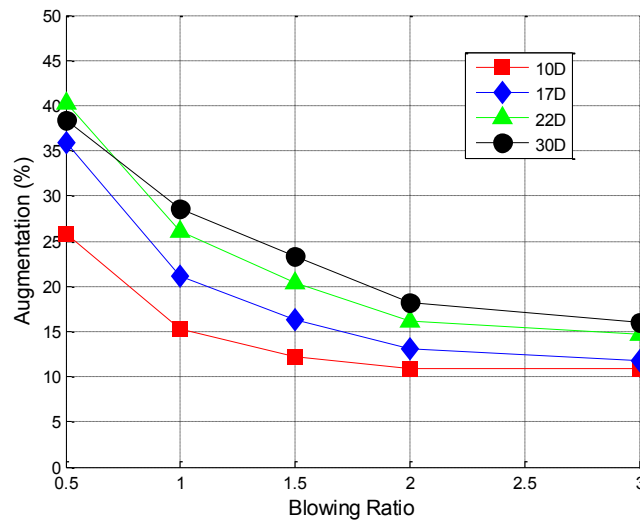


**Figure 0.24:** Five Row - Augmentation vs. Blowing Ratio, $\phi$ = 1.3

### 4.4.2   Five Row – Impact of Equivalence Ratio on Heat Flux and Augmentation

The augmentation results of an equivalence ratio sweep with M = 2.0 are shown in Figure 4.25 and the data is presented in averaged augmentation at each downstream location. A linear trend of increasing augmentation with increasing equivalence ratio was observed for all downstream locations. Similar to the blowing ratio results, augmentation increased with downstream distance *X/D* = 10 to *X/D* = 30. This trend was

110

also seen in the heat flux results, as the difference between nitrogen cooling and air cooling heat flux increased with downstream distance. As more radicals were introduced to the freestream, more radicals were consumed in the mixing layer causing an increased augmentation. Unlike the single row configuration discussed in Section 4.3.3, the Five Row configuration did not exhibit a peak in augmentation for this range of equivalence ratios as a significant amount of oxygen was always present. It is proposed that at an exceptionally high equivalence ratio, the oxygen would be consumed and the Five Row would also show a maximum in augmentation and sequential reduction.
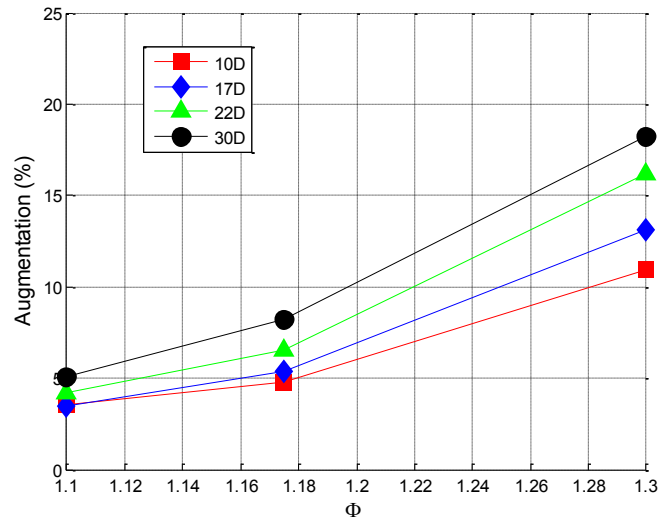


**Figure 0.25:** Five Row – Augmentation vs. $\phi$, M = 2.0

The heat flux at each downstream location for both air and nitrogen cooling is plotted in Figure 4.26. Air cooling cases are plotted with solid symbols and nitrogen cooling cases with open symbols. As equivalence ratio was increased, the heat flux due to nitrogen cooling decreased for all downstream locations. This trend is due to the

111

decreasing freestream temperature with increasing rich equivalence ratio. The opposite

trend was seen with the air cooling; as equivalence ratio was increased the heat flux

increased. This shows that as more radicals were available more heat is released and

absorbed by the wall. The differential between the nitrogen and air cooling cases

increases with downstream distance. This agrees with the trend shown of increasing

augmentation with increasing equivalence ratio.
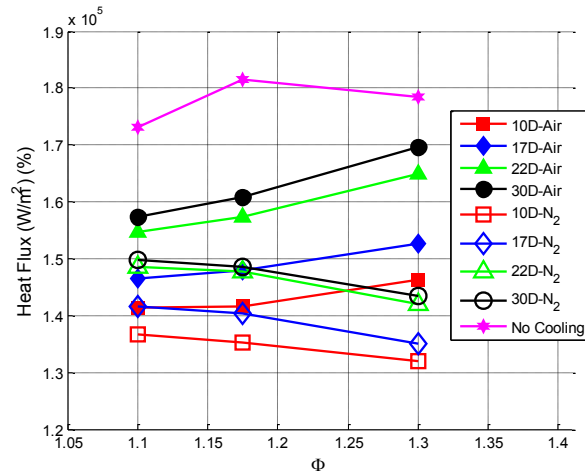


**Figure 0.26:** Five Row - Augmentation vs. $\phi$, M = 2.0

### 4.4.3   Five Row – Emissions

An emissions analysis was performed on the Five Row and swept in the direction

normal to the wall in increments of 2.5 mm. The emissions sampled the percent volume

of $O_2$, CO, and $CO_2$ as described within Section 3.3.3. The results of each species are

presented separately and against distance from the film cooled wall. Each species is also

compared to their no cooling, freestream measurement counterparts. The emissions

results for $O_2$ are presented in Figure 4.27, for CO in Figure 4.28, and for $CO_2$ in Figure

4.29.  All data was taken at a $\phi$ = 1.175 and a M = 2.0.  The emissions of $O_2$ suggest how well the Five Row is creating a layer of non-reacting film.  The baseline, no cooling data of $O_2$ was 0% by volume due to the lack of oxygen in the rich freestream.  For the Five Row case with air as the coolant, the $O_2$ levels increased from 0% in the freestream (*Y/D* = 18) up to 0.85% at the wall. The emissions probe was only able to traverse 18D out of the total width of 35D.  This shows the Five Row created a small layer of non-reacting coolant.  However, when evaluated with the heat flux and NHFR data, this small layer of non-reacting coolant wasn't enough to continue protecting the wall up to *X/D* = 30.  Additional coolant would have to be added to maintain the heat flux below the non-cooling value.
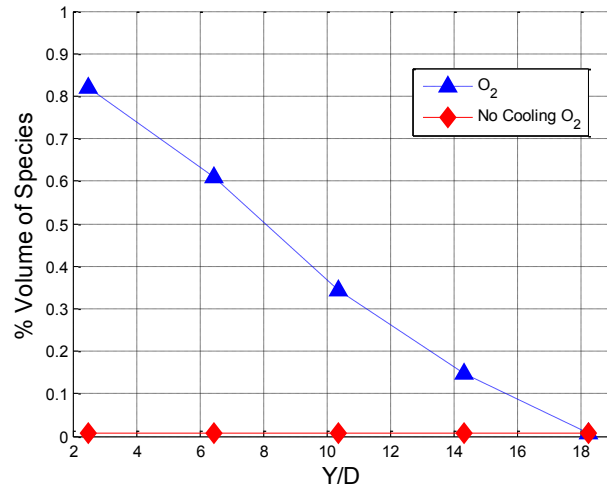


**Figure 0.27:** Five Row – O2 Emissions vs. Distance form film cooled wall, $\phi$ = 1.175, M = 2.0

The emissions of CO give insight to the consumption of radicals by the cooling configuration. The baseline, no cooling data shows CO at 4.6% by volume at a $\varphi = 1.175$. As the emissions probe moved closer to the wall, the amount of CO decreased steadily from 4% down to 1.5% at the wall. This shows that a large portion of the radicals present in the freestream close to the wall are being consumed. However, not all of the radicals are consumed consistent with the elevated heat flux levels shown previously at the further downstream locations. Combining the CO results with the heat flux and augmentation results, the Five Row is doing a decent job of protecting the wall for a small distance downstream while consuming a large number of freestream radicals. Additional rows of coolant added downstream of the Five Row would finish consuming the radicals near the wall and replenish the layer of non-reacting coolant first formed by the Five Row. At the $Y/D = 18$, the value of CO did not reach the no cooling value. From the trend it can be seen the CO emission is approaching freestream value around $Y/D = 21$.
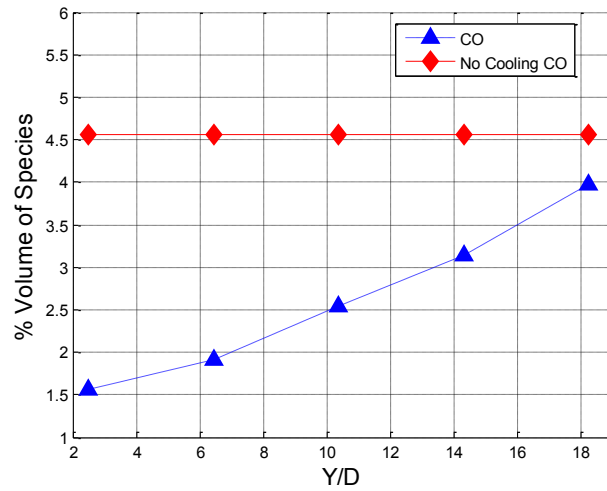
**Figure 0.28:** Five Row - CO Emissions vs. Distance form film cooled wall, $\phi = 1.175$,

$M = 2.0$

The results of the $CO_2$ emissions are complementary to the results of the CO emissions. As CO is consumed, $CO_2$ is produced in its place. As expected, the emissions span showed an increase in $CO_2$ from 9.1% to 10.1% as the probe was traversed towards the wall.  The baseline, no cooling data shows $CO_2$ at 8.7% by volume making an increase of 1.4% by volume of $CO_2$ at the wall.
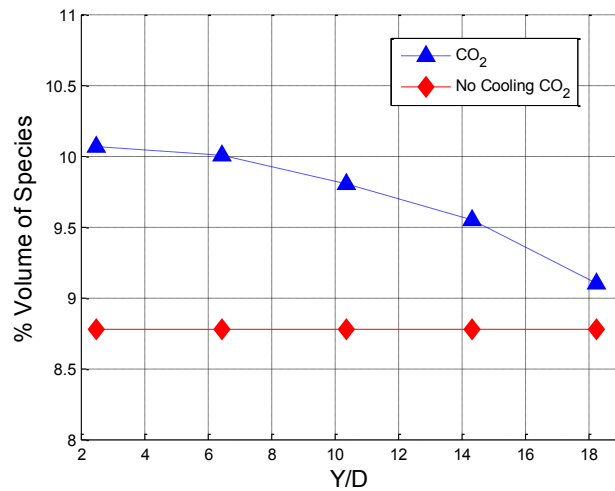
**Figure 0.29:** Five Row – CO2 Emissions vs. Distance form film cooled wall, $\phi = 1.175$,

$M = 2.0$

### 4.4.4 Infrared Imaging

To illustrate the effectiveness of the flame filter to block out the chemiluminescence of the hot combusted gases, IR images are displayed with and without the flame filter in the field-of-view.  Figure 4.30 displays the IR image without the flame filter.  In this image, the flame produced from secondary reactions due to cooling with air can be seen at the top of the image.  Also regions of varying counts can be seen over the whole image indicating the IR camera is seeing the patches of hot gas. When examining a video without the flame filter in place, the hot gas moving downstream is clearly seen.
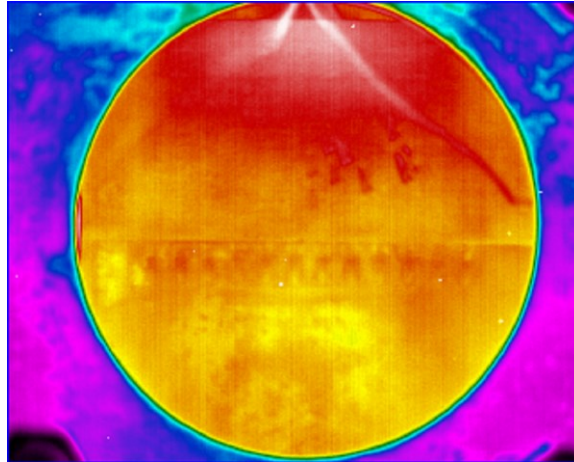
**Figure 0.30:** IR Image without Flame Filter

Figure 4.31 shows the IR image with the flame filter in place. The cooling holes in this image are more visible compared to the cooling holes in Figure 4.30. The high intensity flame region cannot be seen in this image as well. When examining a video with the flame filter in place, the video looks like a static image indicating that the IR camera is only viewing the radiation due to the film cooled wall.
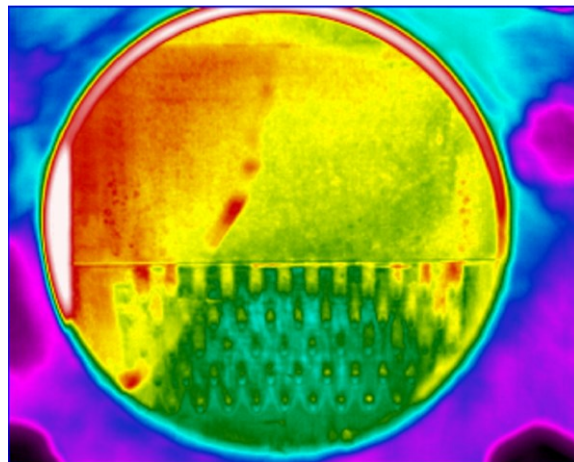


**Figure 0.31:** IR Image with Flame Filter

To gain insight into the distribution of coolant across the span, infrared imaging was examined for its viability to obtain a spatially resolved temperature of the film cooled wall. The IR camera was setup normal to the film cooled wall and videos were taken at 60 fps for 15 seconds. These videos were then averaged to produce an averaged image of the raw counts of photons striking the IR camera. To convert these averaged images of counts into averaged images of temperature, the calibration described in Section 3.3.2 and expressed in Equation 3.1 was used. Figure 4.32 shows the calibrated infrared images of the wall temperature for the five row configuration cooled with air and nitrogen at $M = 2.0$ and $\phi = 1.3$.

A trend of increasing temperature with downstream distance is shown for both cooling cases and this result is expected due to the increase in heat flux with downstream distance. The temperature of the nitrogen cooled wall is around 30 K lower than the temperature of the air cooled wall. This result is also expected due to the lower heat flux and higher NHFR of the nitrogen cooling compared to the air cooling. The discontinuity seen in the middle of the IR image is a crack in the sapphire window that was caused by high thermal gradients as discussed in Section 3.3.2. The white line on both the air and nitrogen IR images indicates where data for comparison later was pulled.

118
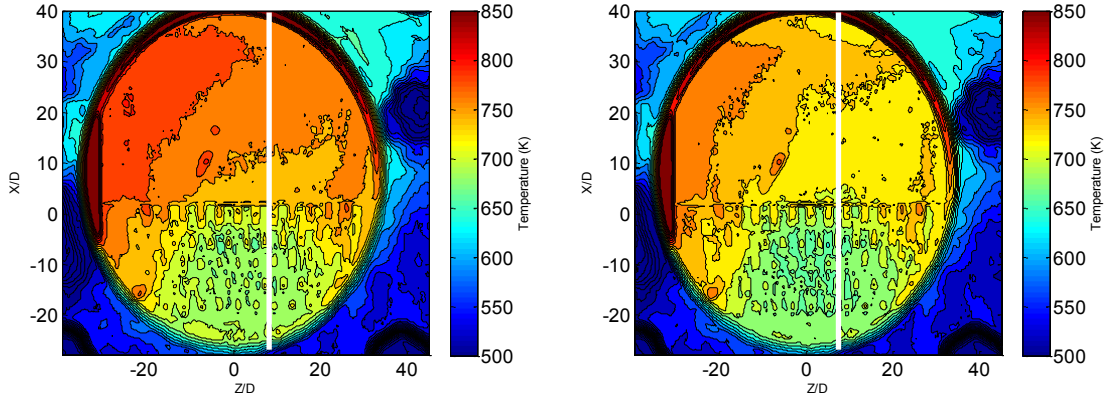
**Figure 0.32:** Air Cooled IR Image (Left), Nitrogen Cooled IR Image (Right), M = 2.0,

$\phi = 1.3$

These calibrated infrared images were compared to the discrete wall temperatures

calculated by the instrumentation block.  The calibration was applied to nitrogen and air

cooled infrared cases and the temperature between the IR image and the thermocouples

were compared. Data from the IR camera was taken at *Z/D* = 5 and compared with the

thermocouples at the matching spanwise location.  These results are shown in Figure

4.33.  A maximum variation of ± 15K is shown which equates to a variation of 1.3% of

the wall temperature.  While the wall temperature of the calibrated IR image is slightly

different than the wall temperature calculated by the thermocouples, the variation

between the two is small enough to conclude that the IR calibration produces an

acceptable wall temperature and certainly captures the surface temperature

119
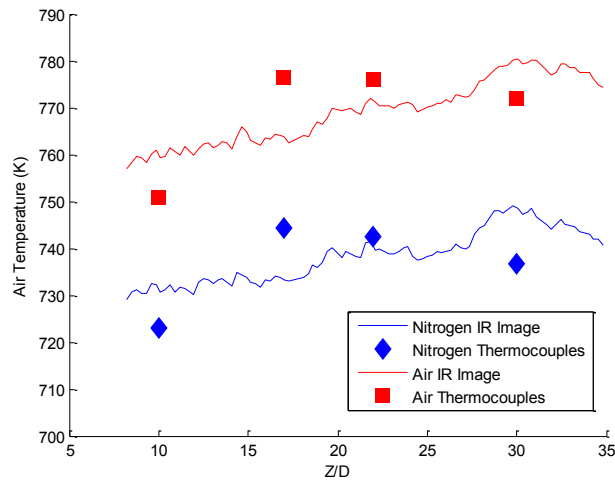
**Figure 0.33:** Air Cooling and Nitrogen Cooling IR Wall Temperature, *Z/D* = 50

An important characteristic is the difference in wall temperature created by reacting and non-reacting film cooling. It is important to ensure the IR calibration can match the temperature along with the difference in temperature between air and nitrogen cooling. Figure 4.34 shows the calibrated IR image of temperature difference between nitrogen and air cooling for the Five Row configuration at $\phi = 1.3$ with M = 2.0. Figure 4.34 was formed by subtracting the nitrogen case from the oxygen case of the calibrated IR images in Figure 4.32. The calibrated IR image of temperature difference was compared to the difference between the thermocouple measurements at *Z/D* = 50 spanwise location (Figure 4.35). A maximum variation of ± 2.5K is seen between the thermocouple measurements and the IR image. This result is small compared to the variation of the air and nitrogen cooling. This shows that the variation in the nitrogen

and air cooling were interdependent and thus the difference between the two had small

variance in temperature.
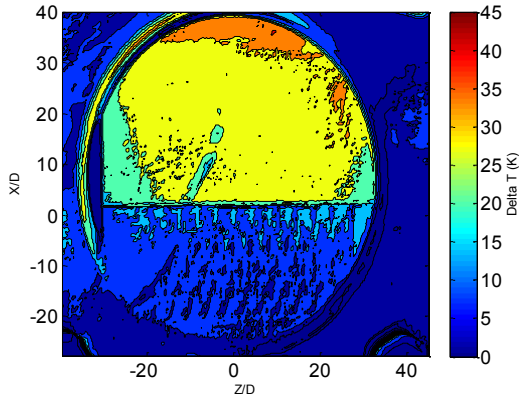


**Figure 0.34:** Temperature Difference, IR Image, M = 2.0, $\phi$ = 1.3
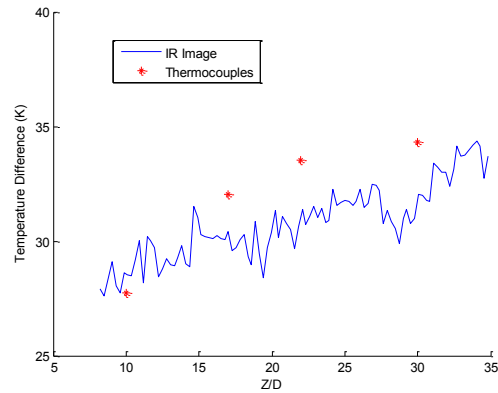


**Figure 0.35:** IR Wall Temperature Difference, *Z/D* = 50

### 4.4.5    Five Row – Flame Visualization and Wall Absorption Parameter

Photographs of the flame were taken at each data point collected during the

blowing ratio sweep and equivalence ratio sweep used to determine heat flux and

augmentation in Section 4.4.1.  These images were enhanced via the method developed

by Robertson that is described in Section 3.3.2.  These photographs give insight to the

location, size, and shape of the flame produced at each condition.  The enhanced images

for the blowing ratio sweep are presented in Figure 4.36 and the for the equivalence ratio

in Figure 4.37.  Table 4.2 contains the flame lengths for the blowing ratio sweep and

Table 4.3 the flame lengths for the equivalence ratio sweep.

At a blowing ratio of 0.5, the flame produced was the shortest at 75 diameters

long and it was the thinnest of all blowing ratios tested.  The flame was highly attached to

the wall and the highest intensity seen in the flame was positioned adjacent to the wall. When combing this image with the heat flux and augmentation data, the close, high intensity flame matches with the high heat flux and augmentation seen at all downstream locations. As the blowing ratio increased, the flame lengths increased up to 153 diameters long and thickness increased. This result is expected because the reaction is oxygen limited and as such adding more oxygen to the system would produce more flame until the mixture became lean. The starting location of the flame remained the same between all the blowing ratios tested. As blowing ratio was increased, the flame showed increased separation from the wall far downstream of the instrumentation block.



**Figure 0.36:** Five Row Flame Visualization, Blowing Ratio Sweep, A – M = 0.5, B – M = 1.0, C – M = 2.0, D – M = 3.0, $\phi$ = 1.175

122

The location and size of the highest intensity of the flame above the instrumentation block changes with the variation in blowing ratio.  As blowing ratio increased, the most intense portions of the flame moved away from the wall but grew in size at the same time.  At a blowing ratio of 3.0, a large high intensity patch was shown above $X/D = 10$ to $X/D = 30$ but a section of less intense flame was present between the wall and this patch.  The distance from the wall and these intense patches of flame does not grow as quickly as the size of the patch.  This indicates a balance between distance from the wall and potential heat release of the flame and this matches the trend of a minimum heat flux release at a blowing ratio of 1.5 seen in Figures 4.20, 4.21, 4.22, and 4.23.

**Table 0.2:** Five Row Flame Lengths, Blowing Ratio Sweep

| Five Row - Flame Lengths | | | | | |
|---|---|---|---|---|---|
| Blowing Ratio | .0.5 | 1 | 1.5 | 2 | 3 |
| Flame Length (D) | 75 | 106 | 133 | 146 | 153 |

The enhanced flame images from the equivalence ratio sweep are presented in Figure 4.33.  As equivalence ratio was increased, the intensity of the flame increased above the region of $10 \leq X/D \leq 30$.  This indicates an increase in heat release at these locations which would result in increased heat flux to the wall.  This trend was seen by the augmentation analysis of the equivalence ratio sweep in Figure 4.25. Because the blowing ratio and configuration are the same between each image, the rate of mixing of the freestream and the coolant is the same between each image.  The increase in heat flux

is then causes by an increased number of radicals locally, which results in quicker mixing of the coolant and the freestream radicals. A larger portion of the oxygen in the coolant is consumed in this region resulting in a higher potential heat release and higher heat flux.
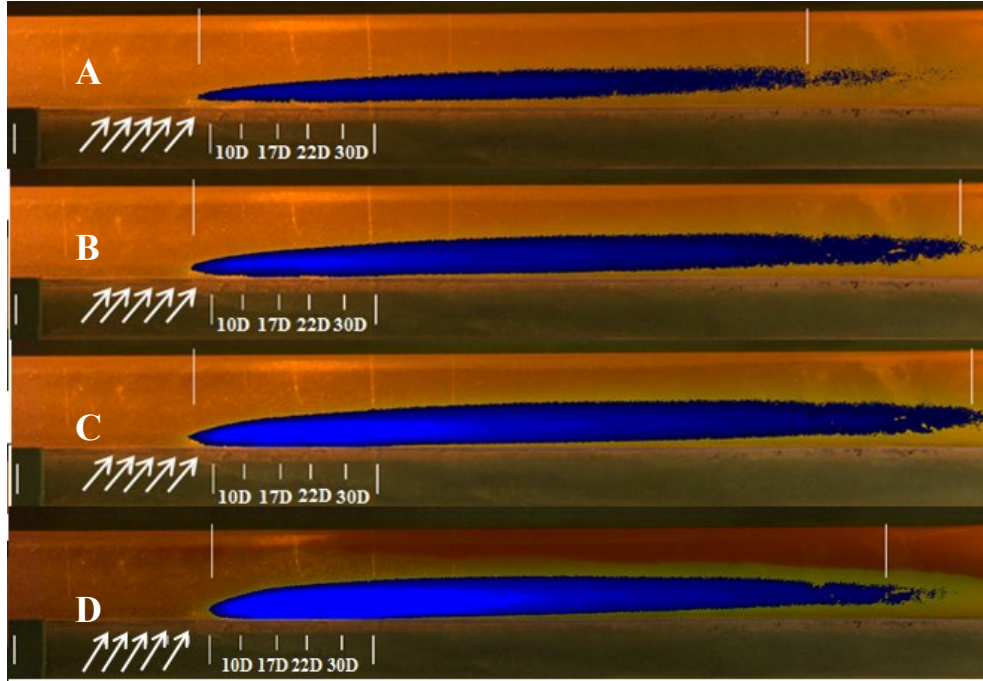


**Figure 0.37:** Five Row Flame Visualization, Equivalence Ratio Sweep, A – $\phi$ = 1.1, B – $\phi$ = 1.175, C – $\phi$ = 1.3 D – $\phi$ = 1.4, M = 2.0

**Table 0.3:** Five Row Flame Lengths, Equivalence Ratio Sweep

| Five Row - Flame Lengths | | | | |
|---|---|---|---|---|
| Equivalence Ratio | 1.1 | 1.175 | 1.3 | 1.4 |
| Flame Length (D) | 115 | 146 | 148 | 128 |

While heat flux augmentation enables a local comparison between cooling configurations, it does not take into account the extent of the heat release.  Furthermore,

augmentation does not allow comparisons between configurations with different mass flow rates of coolant due to different number or size of holes.   As the mass flow rate increases, the chemical potential for heat release also increases.  To account for variations, Robertson [23] created a parameter called Wall Absorption (WA), discussed in Section 2.4.1.  By measuring the length of the flame ($L_{flame}$), through visible spectrum photographs such as seen in Tables 4.2 and 4.3, and taking the width ($w_{flame}$) to be the span encompassing the film cooling holes a flame sheet area was determined. A nominal power absorbed by the wall was obtained by multiplying the increase in heat flux ($q_{differential}$) between reactive and nonreactive cases by the flame area.  This value was normalized by dividing by the predicted maximum heat release ($Q_{potential}$).  This heat release was calculated through the use of CHEMKIN taking account the freestream equivalence ratio, the heating value of the fuel, and the amount of injected air. The potential heat release for five rows of holes was found to be 478 W for $M = 2.0$ and $\phi = 1.3$.  Table 4.4 shows the *WA* parameter values for $\phi = 1.3$ with $M = 1.0$ and 2.0 and for $\phi = 1.175$ with $M = 2.0$.

**Table 0.4:** Five Row - Wall Absorption Parameter

| Configuration | Wall Absorption (%) | | |
| --- | --- | --- | --- |
| | $\varphi$=1.3 M=1.0 | $\varphi$=1.3 M=2.0 | $\varphi$=1.175 M=2.0 |
| Five Row | 46.30% | 21.06% | 7.46% |

The trends shown by the WA parameter follow similar trends to that of heat flux and augmentation. As the blowing ratio was increased, the Five Row provided better protection downstream and thus resulted in low wall absorption even with the increased potential heat release. As the equivalence ratio increased the number of available radicals increased. As the freestream and the cooling jet mix, the increased number of radicals caused the reaction to release more heat near the wall. This resulted in higher augmentation and higher wall absorption.

## 4.5    Additional Cooling Configuration Comparison

The Five Row configuration was first developed and examined to determine the effect of the build-up of multiple rows of coolant. Because the Five Row showed promise in providing effective downstream cooling by minimizing additional heat flux to the wall while consuming radicals, it was chosen to act as a baseline for comparison with additional configurations described in Section 3.4.2. The purpose of these additional configurations focused on either consuming more freestream radicals or creating a film cooling film that protected the wall better than the cylindrical holes. This section will discuss the augmentation as functions of blowing ratio, equivalence ratio, and downstream distance and net heat flux reduction (Section 4.5.1) for these additional cooling configurations. These parameters will assess the ability for the cooling configurations to protect the wall from secondary reactions. Additionally, an examination of emissions sweeps (Section 4.5.1) will provide insight on the consumption of radicals as a function of distance from the film cooled wall. Finally, evaluation of

visible spectrum photographs of the flames produced by secondary reactions as well as wall absorption parameter will give insight to where heat release occurred and how it impacted the film cooled wall.

With the goals of consuming radicals while protecting the wall from secondary reactions, this thesis devised various five row cooling schemes that are described in Section 3.4.2. These configurations were designed with varying goals in mind. The Five Row Slot, Five Row Trench, and Backwards Facing Step configurations were designed to protect the wall by minimizing the heat flux to the wall through the build-up of a non-reactive coolant layer beneath the burning layer. This group is referred to as the Wall Protection group. The Cross Flow, Swirler, Roll Forward, and Two Row Upstream, on the other hand, were meant to enhance mixing in an attempt to consume radicals and to control where radical consumption was taking place. This group is referred to as the Enhanced Mixing group. Both groups were compared to the baseline Five Row of cylindrical holes. Because of the distinctions in design goals, the cooling configurations were plotted separately for better comparison between like goaled configurations.

### 4.5.1 Wall Protection Schemes

#### 4.5.1.1 Impact of Blowing Ratio on Augmentation

The results of a blowing ratio sweep are presented for the Wall Protection Schemes in Figure 4.38. The blowing ratio was varied from 0.5 to 3.0 at a constant $\Phi =$ 1.3. All configurations were run at the same mass flow as the Five Row configuration. This allowed for comparison of configurations with differing coolant exit areas like the

Five Row Slot configuration.  The blowing ratio sweep data is presented at *X/D* = 22.

This location was arbitrarily chosen as representative of the general trends. Also the

variation of augmentation as a function of downstream distance is covered later in this

section.
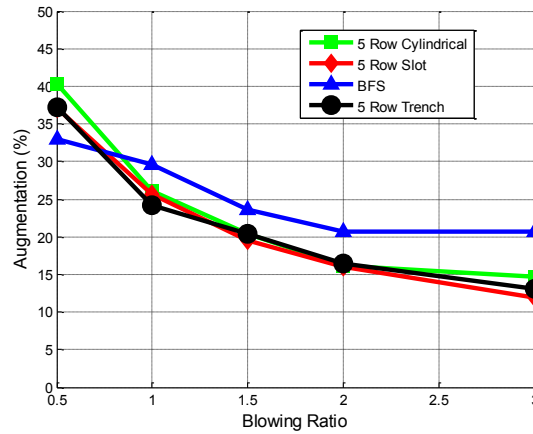


**Figure 0.38:** Augmentation vs. Blowing Ratio, $\phi$ = 1.3, *X/D* = 22

Almost identical trends between the Five Row Cylindrical, Five Row Slot, and

Five Row Trench are shown across all blowing ratios.  All three configurations peak

between 37% and 40% augmentation at a blowing ratio of 0.5 and continue to decrease in

augmentation to a value around 14% as blowing ratio increased.  The Backward Facing

Step followed a similar trend of decreasing augmentation with increasing blowing ratio.

However, it started at a lower augmentation at M = 0.5 and decreased slower than the

other three configurations leveling off around 20% augmentation at M = 3.0.   The higher

augmentation of the backward facing step for higher blowing ratios can be attributed to

less rows of cooling and therefore less available mass flow dedicated to protecting the wall.
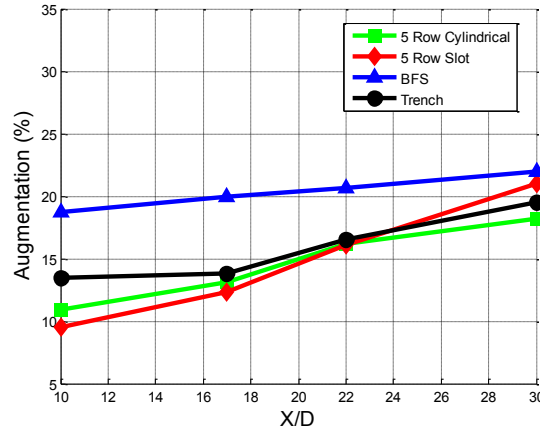


**Figure 0.39:** Augmentation as a function of downstream distance; $\phi = 1.3$, $M = 2.0$

The variation of augmentation as a function of downstream distance is displayed in Figure 4.39. The augmentation presented is averaged augmentation at each downstream location at a $M = 2.0$ and $\phi = 1.3$. All configurations show increasing augmentation with downstream distance. The BFS show a linear trend of increasing augmentation with downstream distance and produced the highest augmentation across all downstream distances. However, at $X/D = 30$ the other three configurations approach the value of the BFS indicating a slower growth of additional heat flux to the wall. The other three schemes show a similar trend with increasing downstream distance except for small variations at $X/D = 10$ and $X/D = 30$. At $X/D = 10$, the Five Row Trench showed 3% higher augmentation than the other two configurations and the Five Row Slot showed the lowest augmentation. At $X/D = 30$, the Five Row Slot showed the highest

129

augmentation of the three by 2.5% and the Five Row Trench and Five Row showed a trend of reduced, additional augmentation with downstream distance.  To explain the trends seen in augmentation, an examination of the flames produced by each configuration is in order.

### 4.5.1.2 Wall Protection Schemes - Flame Images

The flame images of the Wall Protection configurations can be seen in Figure 4.40.  Flame images were enhanced using the method described in Section 3.3.2.  The flame lengths of each configuration are listed in Tables 4.5.  This study examined the flame produced by the Wall Protection configurations at a blowing ratio of two and at an equivalence ratio of 1.3 in order to explain the trends seen in augmentation.

The Five Row configuration produced a 136 diameter long flame that began at the last row of cooling holes, $X/D = 0$.  The flame of the Five Row showed the highest intensity from $X/D = 10$ to around $X/D = 40$ where the intensity decreased with further downstream distance. This indicates that further downstream the amount of additional heat flux would be reduced.   The reacting film separated from the wall around an $X/D = 35$ and a non-reactive layer grew with downstream distance.  The separation of the reacting film would result in a reduction of additional heat flux to the wall due to secondary reactions.  This is likely the reason for the slope of the Five Row decreasing from $X/D = 22$ to $X/D = 30$.

**Figure 0.40:** Flame Visualization, $\phi = 1.3$, M = 2.0, A-Five Row, B-Five Row Slot, C-Five Row Trench, D-Backwards Facing Step

The Five Row Slot produced a 130 diameter long flame that started around the second to last cooling row which was the furthest upstream of the Wall Protection schemes. The flame produced was initially very skinny that grew in height steadily with downstream distance. The flame produced was highly attached. Unlike the Five Row configuration where the flame separated around $X/D = 40$, the flame of the Five Row Slot does not separate from the wall until approximately $X/D = 90$. The flame burning close to the wall for a long distance would cause increased heat flux to the wall. However, the intensity of the flame next to the wall was low so only a small amount of additional heat

was release per distance downstream. The height of the flame produced by the Five Row Slot was much larger at all downstream distances compared to the Five Row. This shows that a large portion of radicals were consumed further away from the wall than the Five Row scheme.

The Five Row Trench produced a flame with a length of 129 diameters that began 4 diameters downstream of the last row of injection holes. The flame produced had a smaller area of intense flame above the instrumentation block that dissipated quickly with downstream distance. This small region of intense flame produces less heat and thus less heat transfer to the wall. Also the reduction in intensity of the flame would result in lower heat flux to the wall downstream. The flame separated from the surface farther downstream then the Five Row around $X/D = 40$. The separation of the flame is thought to be due to the local equivalence ratio hitting the upper stability boundary after enough oxygen was consumed near the wall. This would indicate that a flame that separates from the wall more quickly, either has a cooling scheme that promotes separation at the flow conditions or a higher consumption of radicals near the wall shortly downstream of injection.

**Table 0.5:** Wall Protection configurations, Flame Lengths

| Length (D) | Five Row Cylindrical | Five Row Slot | Five Row Trench | Backwards Facing Step |
|---|---|---|---|---|
| M = 2, $\phi$ = 1.3 | 136 | 130 | 129 | 132 |
| M = 1, $\phi$ = 1.3 | 108 | 80 | 78 | 73 |

The Backward Facing Step (BFS) initially produced a large, intense flame directly above the instrumentation block. This intense flame above the $X/D = 0$ to $X/D = 22$ \ would explain the high augmentation at these locations. This initial burst of intense flame is likely due to the normal set of holes in the BFS meant to create a burning layer of film. This high intensity early on is the reason for the high augmentation in the region of $X/D = 10$ through $X/D = 22$. By the $X/D = 30$, the flame of the BFS begins to separate and the intensity of the flame is decreased. This decrease in flame intensity and early flame separation explains why the BFS experienced small increases in augmentation with downstream distance compared to the Five Row, Five Row Trench, and Five Row Slot.

### 4.5.1.3 Impact of Blowing Ratio on Heat Flux and Net Heat Flux Reduction

While the flame images and augmentation analysis give insight to the physics of each cooling configuration, these parameters do not directly tell how well a configuration cools the wall. In order to evaluate the effectiveness of a configuration to cool the wall, an analysis of heat flux and net heat flux reduction were performed. Heat flux and NHFR results at $X/D = 22$ and a $\phi = 1.3$ for the blowing ratio sweep are presented in Figure 4.41

133

and 4.42. The results of nitrogen cooling are plotted as open symbols, air cooling as solid symbols, and no cooling as solid cyan diamonds. The no cooling heat flux line was formed by supplying no coolant to the cooling scheme. While augmentation presented similar results for the Five Row, Five Row Slot, and Five Row Trench, the heat flux and NHFR results presented a very different story.

The Five Row Slot showed a trend of decreasing heat flux with increases blowing ratio. This trend only slightly tapered off at $M = 3.0$ indicating that more mass flow would still highly benefit the cooling scheme. Nitrogen cooling in the Five Row Slot produced heat flux values lower than the no cooling case indicating that the Five Row Slot effectively cools the wall with no secondary reactions. Nitrogen cooling in this configuration also produced the lowest heat flux of any nitrogen cooled configuration showing the Five Row Slot was the most effective configuration in cooling the wall as expected. This result is also shown by NHFR as the nitrogen cooled case produced the highest, positive NHFR. The Five Row Slot also produced the lowest heat flux and highest NHFR when air was supplied as a coolant. The difference between air and nitrogen heat flux is decreasing with increasing blowing ratio which matches the trend of decreasing augmentation with increasing blowing ratio shown in Figure 4.33. Overall, the Five Row Slot more effectively cooled the wall for blowing ratios above one.
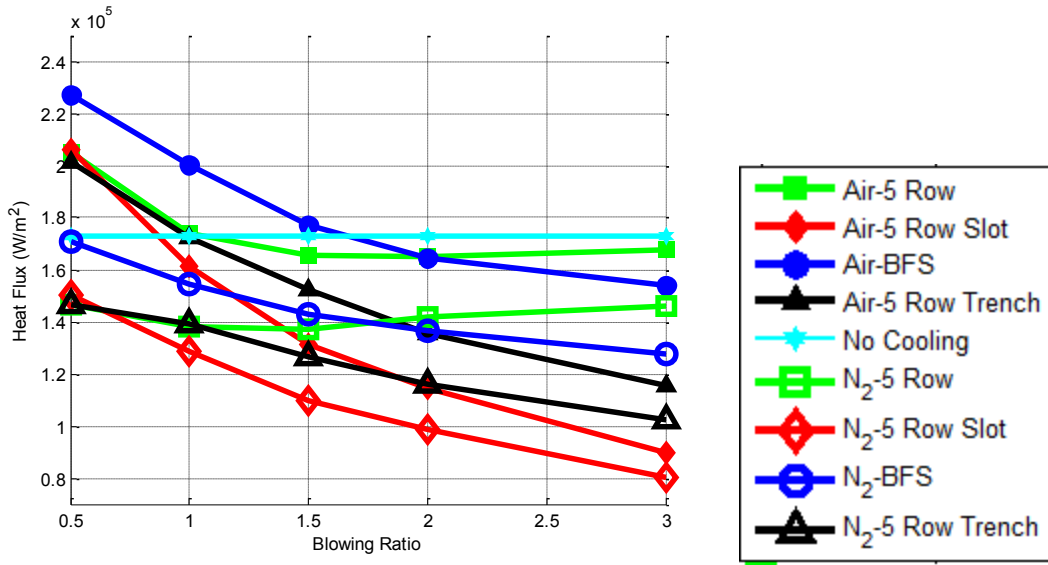
**Figure 0.41:** Heat Flux vs. Blowing Ratio, Wall Protection Schemes, $\phi = 1.3$, $X/D = 22$

The Five Row configuration also showed a trend of decreasing heat flux with increasing blowing ratio up to $M = 2.0$. After this point the trend being to reverse and the heat flux slightly increases with further increases in blowing ratio. This reversal in trend is likely due to separating of the film coolant from the wall drawing higher temperature reactive gasses back towards the wall. The nitrogen cooling of the Five Row produced heat flux values below that of the no cooling case indicating that without secondary reactions the Five Row scheme protects the wall. Air cooling however, only produced heat flux values below the no cooling value of 175,000 W/m$^2$ for blowing ratios greater than 1.5. Even at these blowing ratios the difference in heat flux between the air cooling and no cooling case was only 5,000 W/m$^2$ compared to upwards of 80,000 W/m$^2$ of the Five Row Slot. These trends are shown in the NHFR data as well where the Five Row

135

produced low, positive NHFR with air cooling indicating poor cooling performance for both air and nitrogen compared to the other configurations tested.  While the Five Row does protect the wall with secondary reactions present, its performance is dwarfed by that of the Five Row Slot.

The Five Row Trench produced a similar trend in heat flux and NHFR as the Five Row Slot.  The heat flux values of the Five Row Trench were higher for all blowing ratio tested for both air and nitrogen cooling compared to that of the Five Row Slot.  Considering a trench configuration was designed to mimic the characteristics of a slot without the unfeasibility of implementing the slot in turbine like conditions, the trends being similar was expected and is encouraging.  The higher heat flux values indicate that the Five Row Trench did not protect the wall as well as the Five Row Slot.  The NHFR shows that for $M = 0.5$ and $M = 1.0$ the Five Row Trench supplied with air increased the heat flux to the wall over the no cooling case.  This means for the Five Row Trench to be effective in protecting the wall it must be run at $M \geq 1.0$.  This is more than the required mass flow than the Five Row Slow which can effectively cool the wall at this downstream location at a $M = 1.0$.
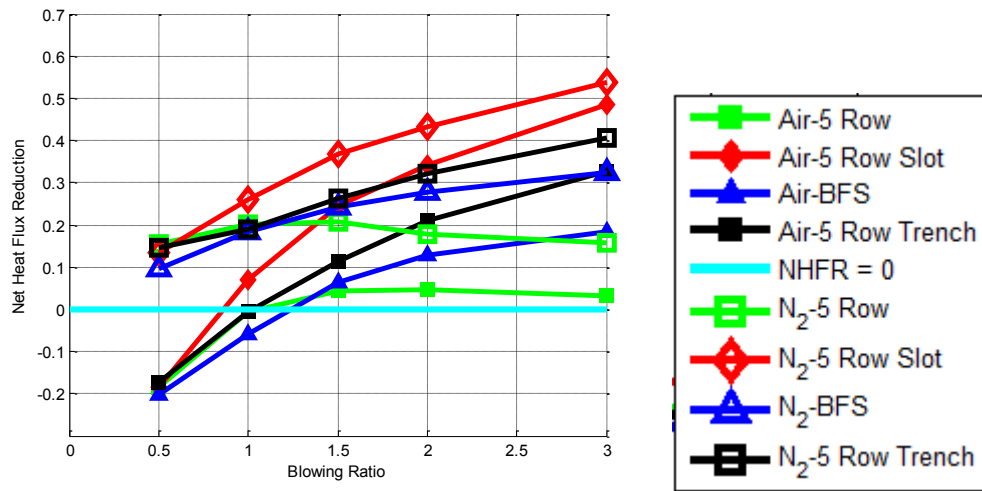
**Figure 0.42:** NHFR vs. Blowing Ratio, Wall Protection Schemes, $\phi = 1.3$, $X/D = 22$

The Backward Facing Step produced higher heat flux for both air and nitrogen cooling in the range of $0.5 \leq M \leq 1.5$. For $M > 1.5$, the heat flux of the BFS reduced below the heat flux of the Five Row and showed a trend of continued reduction with increasing mass flow. This trend showed signs of leveling off indicating that a limited amount of additional mass flow to the BFS would provide additional reduction in heat flux. These trends are shown in the NHFR results as well. The NHFR of the BFS increased with increasing blowing ratio for both air and nitrogen cooling and showed reducing gains in NHFR for increasing blowing ratio. Nitrogen cooling in the BFS resulted in positive NHFR across all blowing ratios tested but air cooling only resulted in positive NHFR for $M \geq 1.5$. This indicates that the BFS would be a poor cooling scheme for scenarios where a low amount of coolant is available.

137

Ultimately the overall goal of film cooling is to reduce the wall temperature of the component being cooled. IR images were taken of each configuration at $\phi = 1.3$, $M = 2.0$. These IR images were converted to temperature with the IR calibration derived in Section 4.4.4. The wall temperature was examined both streamwise and spanwise in order to understand the temperature distribution created by each cooling scheme. The streamwise variation was examined at $Z/D = 5$ and the spanwise variation was sampled from the $X/D = 22$. The regions were temperature data was taken for these studies are shown in Figure 4.43. These locations match the spanwise and streamwise locations of a few thermocouple pairs within the instrumentation bock.
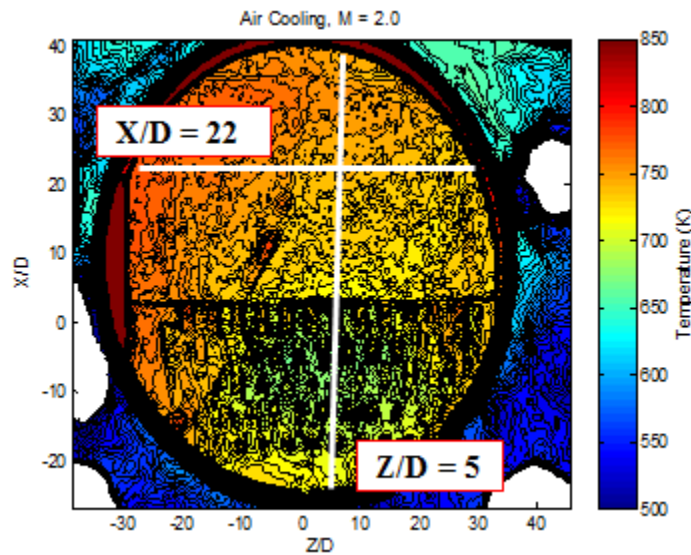


**Figure 0.43:** IR Wall Temperature Sampling Locations.

The streamwise variation of wall temperature as measured by the IR camera is displayed in Figure 4.44 for the Wall Protection configurations. The Five Row Slot

138

produced the lowest wall temperature from 680 K at $X/D = 0$ to 770K at $X/D = 35$. A lower heat flux produces a lower wall temperature so this result agrees with the heat flux and NHFR results. At $X/D = 30$, the wall temperature of the Five Row Trench scheme matches that of the Five Row Slot. This shows that the Five Row Slot is growing in temperature with downstream distance more quickly than the Five Row Trench. This is due to the highly attached flame of the Five Row Slow that continues to release heat adjacent to the wall unlike the Five Row Trench that separates from the wall around $X/D = 40$.

The Five Row and BFS configurations produced similar wall temperatures as functions of downstream distance for $X/D = 17$ to $X/D = 30$. At $X/D = 5$ the BFS produced a wall temperature 20 K below that of the Five Row that eventually matched the Five Rows wall temperature at $X/D = 17$. The rapid rise in temperature compared to the Five Row that the BFS experiences is due to the large region of intense flame in this location seen in Figure 4.40. The temperature of the BFS eventually increased above the temperature of the Five Row indicating poorer performance farther downstream for the BFS than the Five Row.
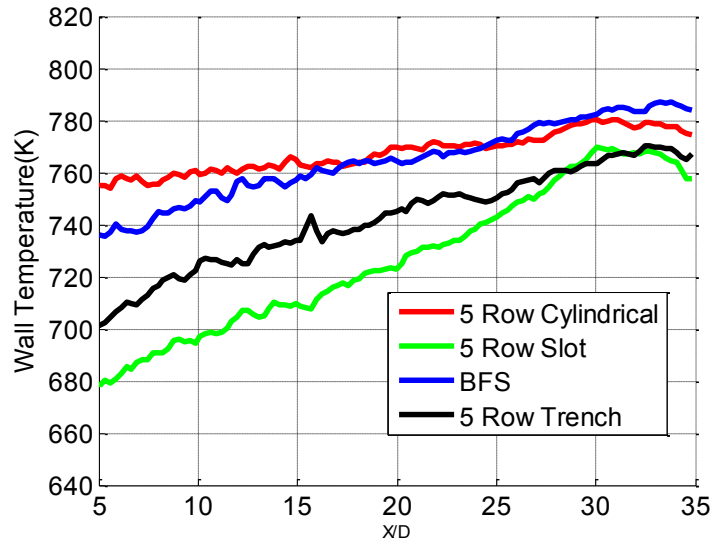
**Figure 0.44:** Downstream variation of wall temperature, *Z/D* = 5, $\phi$ = 1.3, M = 2.0

The spanwise variation of wall temperature as measured by the IR camera is displayed in Figure 4.45 for the Wall Protection configurations. Each configuration showed the same linear decrease in temperature from left to right. This trend was shown in the surface temperature uniformity discussion in Section 4.2 and was attributed to the swirl from the WSR not being fully removed. All results are presented in row averaged forms and the variation is small so this trend is unlikely to affect the results.
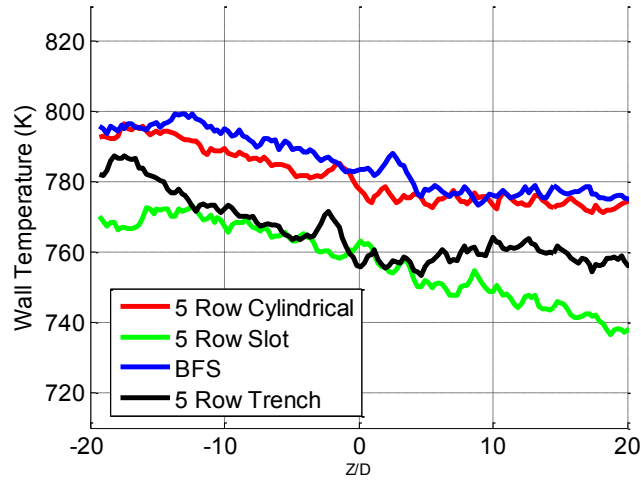
**Figure 0.45:** Spanwise variation of wall temperature, *X/D* = 22, φ = 1.3, M = 2.0

### 4.5.1.4 Emissions

An emissions analysis was performed on each configuration and swept in the direction normal to the wall in increments of 2.5 mm. The emissions sampled the percent volume of $O_2$, CO, and $CO_2$ as described within Section 3.3.3. The results of each species are presented separately and are plotted against distance from the film cooled wall. Each species is also compared to their no cooling, freestream measurement counterparts. Figure 4.46 displays the emissions of CO, Figure 4.47 the emissions of CO2, and Figure 4.48 presents the emissions of O2 for the Wall Protection schemes. The emissions data was taken far downstream of the holes around *X/D* = 200.

Out of the Wall Protection schemes, the Five Row Trench showed the largest consumption of CO with 6.3% at *Y/D* = 18 reducing to 2% at *Y/D* = 2. It also showed the largest reduction in CO in locations near the wall by nearly 0.5%. Combining this result

with the heat flux and NHFR results yields a cooling scheme that consumes a large number of radicals while still viably protecting the wall. The Five Row Slot which showed reduced heat flux and increased NHFR than the Five Row Trench showed reduced CO consumption.  The Five Row Slot more effectively cooled the wall because it mixed and consumed less CO from the freestream with its coolant flow.  Even though the flame produced by the Five Row Slot is similar in size to the Five Row Trench, the intensity of the flame is much less indicating lower heat release.  The lower CO consumption of the Five Row Slot confirms that the Five Row Slot released less heat due to secondary reactions and as a result it produced the lowest wall temperature.
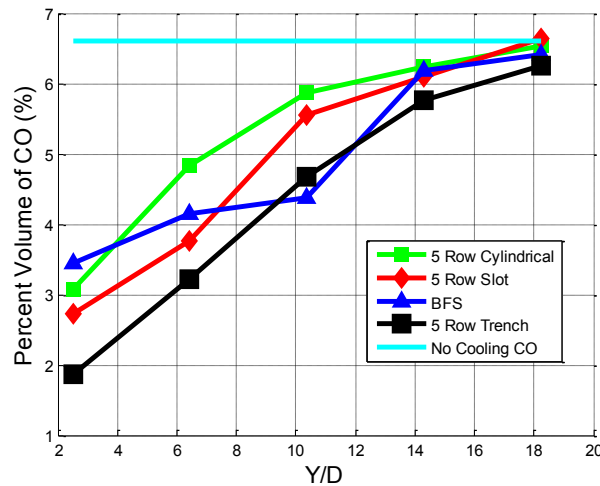


**Figure 0.46:** CO Emissions, $\phi = 1.3$, M = 2.0

The Backward Facing Step consumed similar amounts of CO as the Five Row Slot from $Y/D = 18$ to $Y/D = 14$.  At $Y/D = 10$, however, the BFS showed a big reduction of CO from 6.2% at $Y/D = 14$ to 4.5% at $Y/D = 10$.  This spike in consumption of CO is

142

due to the row of normal holes at the top of the step. The flow from the normal set of holes penetrated the freestream flow to *Y/D* = 14 and mixed with it, resulting in a high consumption of CO. This configuration does not consume as much CO as the Five Row Trench nor does it protect the wall as well as the Five Row Trench. However, it does show promise that large, controlled consumption of CO is possible while still reducing the heat flux to the wall compared to the Five Row configuration.
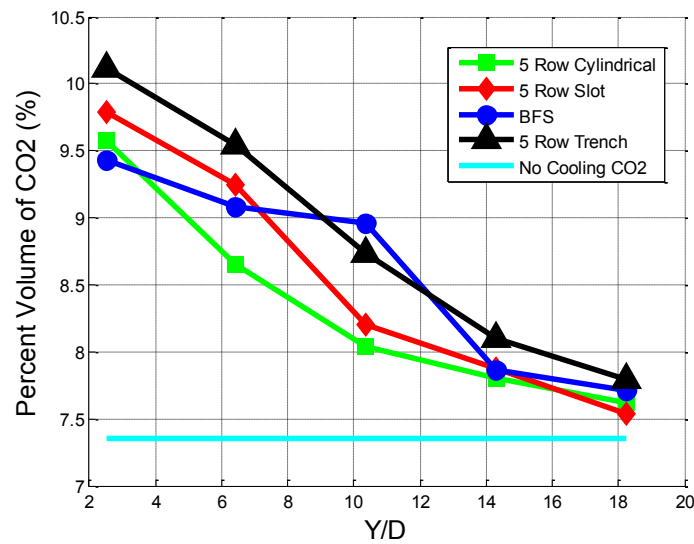


**Figure 0.47:** CO2 Emissions, $\phi$ = 1.3, M = 2.0

The $CO_2$ emissions are complementary to the results of the CO emissions. As CO is consumed, $CO_2$ is produced in its place. The configurations that consumed the most CO produced the most $CO_2$.

Emission of oxygen remaining in the flow as a distance from the wall tells how much oxygen remained attached to the wall. The remaining oxygen in the flow tells how

much coolant remained attached to the wall and unconsumed and how much potential heat was not released. Schemes that have high oxygen near the wall don't necessarily prevent reactions from occurring near the wall. If the flow mechanics prevent mixing with the coolant layer near the wall with additional freestream radicals, the local equivalence ratio will eventually become too low and the flame will become unstable and eventually go out. This is thought to be the reason for the flames produced to eventually "separate" or stop reacting in areas next to the wall.
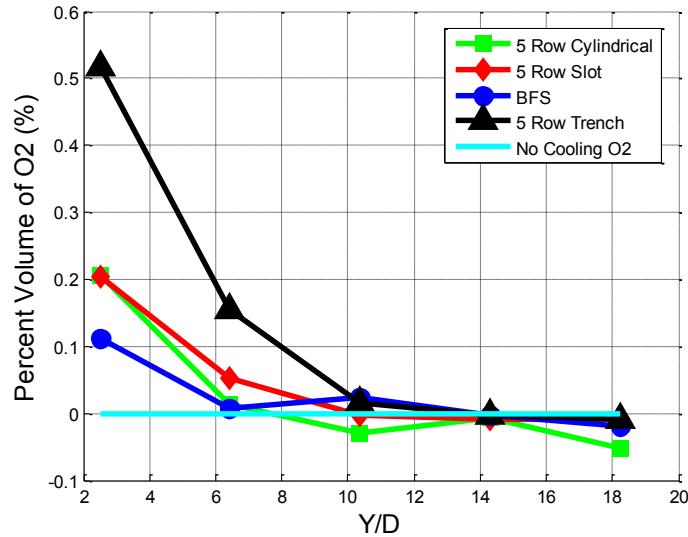


**Figure 0.48:** O2 Emissions, $\phi = 1.3$, $M = 2.0$

The Five Row Trench showed the largest amount of oxygen near the wall. From the discussion of trenches in Section 2.4, the interaction with the trench wall creates vortices that counteract the vortices created from typical discrete film cooling that would result in the sweeping of hot core flow towards the wall. Because the trench counteracts

these vortices, less freestream flow full of radicals reaches the near wall area resulting in a reduction of the local equivalence ratio until the flame can no longer be sustained.  The other configurations tested show very little oxygen left near the wall indicating consumption of oxygen near the wall and more CO radicals remaining near the wall as confirmed by Figure 4.48.

### 4.5.1.5 Impact of Equivalence Ratio on Heat Flux and Augmentation

The augmentation results of an equivalence ratio sweep are presented for the Wall Protection Schemes in Figure 4.49.  The equivalence was varied from 1.1 to 1.3 at a constant M = 2.0.  The equivalence ratio sweep data is presented at the $X/D = 22$ location. Similar to the blowing ratio sweep results, the Five Row Cylindrical, Five Row Slot, and Five Row Trench have almost identical variation in augmentation with equivalence ratio. These three configurations show a linear increase in augmentation with increasing equivalence ratio.  These configurations are almost indistinguishable when examining their augmentation.  The Backward Facing Step shows the same trend of linear increase of augmentation with increasing equivalence ratio but it was 5% augmentation higher at every data point.  This result is due to the increased mixing from the row of normal holes at the top of the step that injects coolant that penetrates farther into the freestream than the 30˚ holes.  Also the higher augmentation of the BFS is due to fewer rows of coolant being directed to protect the wall.  If five rows of coolant were put down to protect the wall instead of four the augmentation would be much more similar but still slightly increased due to the enhanced mixing.

145
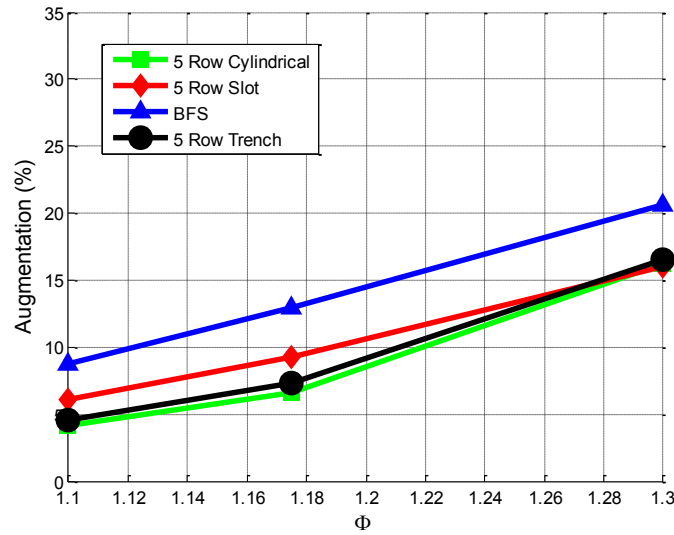
**Figure 0.49:** Augmentation vs. $\Phi$, M = 2.0, *X/D* = 22

The heat flux results as a function of equivalence ratio for M = 2.0 at *X/D* = 22 are shown in Figure 4.50. All nitrogen cooling cases showed linearly decreasing heat flux as equivalence ratio increased. This result is due to the decrease in freestream temperature experience when a rich equivalence ratio is increased. All air cooling cases experience linear increases in heat flux as equivalence ratio was increased. This result was likely due to the local equivalence ratio in the area next to the wall increasing and causes a quicker consumption of radicals. The linearly increasing air cooling along with linearly decreasing nitrogen cooling heat flux results in linearly increasing augmentation as seen in Figure 4.49.
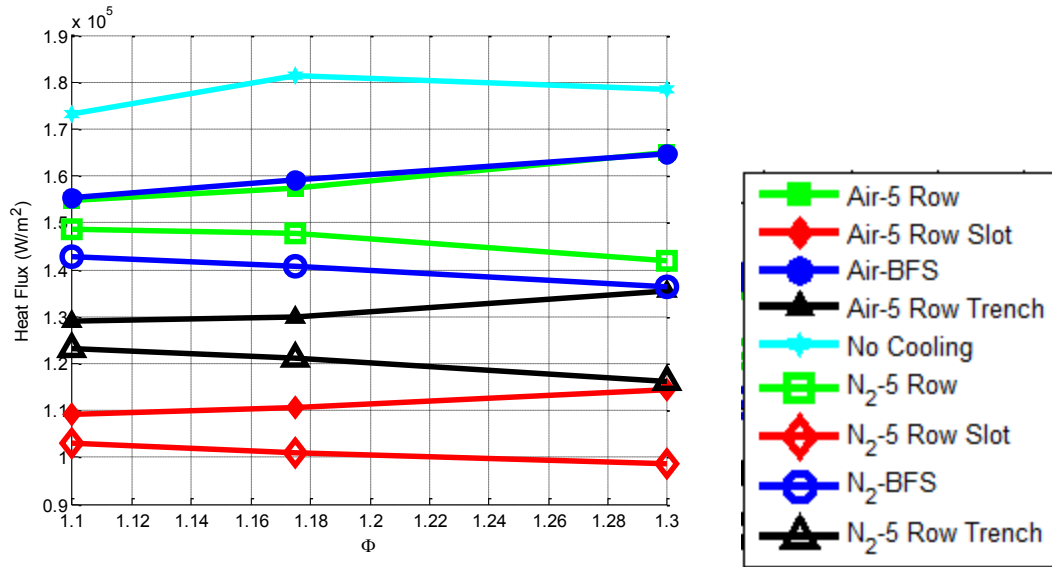
**Figure 0.50**: Heat Flux vs. Φ, M = 2.0, *X/D* = 22

### 4.5.1.6 Wall Absorption Parameter

Determination of Wall Absorption allows for the examination of the overall effect of the heat release due to secondary reactions.  However, to determine the overall effect, the heat flux underneath the entire flame length must be known.  Because this information was unable to be acquired with this test rig, the WA parameter was calculated to examine the amount of potential heat entering the instrumentation block. Table 4.6 displays the Wall Absorption parameter of the Wall Protection configurations tested at a constant equivalence ratio of 1.3 and M = 1.0 and  M = 2.0.  All configurations showed a 50% or greater reduction in Wall Absorption parameter when the blowing ratio was increased from 1.0 to 2.0.  This indicates that the configurations protected the wall more efficiently with more mass flow even with the increased heat flux potential.

The Five Row Slot produced the lowest Wall Absorption parameter. As expected the configurations that produced the lowest heat flux and wall temperature should show the lowest amount of heat being absorbed by the wall under the flame. The Five Row Trench resulted in slightly higher Wall Absorption than the Five Row Slot. This result matches the slightly higher heat flux and wall temperature displayed by the Five Row Trench. More of the potential heat release reached the wall for this configuration and thus a worse cooling performance was seen. However, even though the Five Row Trench does not protect the wall as effectively as the Five Row Slot it is a more feasible configuration to implement in a turbine environment.

The Backwards Facing Step showed increased Wall Absorption compared to the Five Row for $M = 1.0$ and $M = 2.0$. Because the Five Row configuration has five rows of coolant to protect the wall and the BFS only has four, the increase in mass flow allowed the Five Row to protect the wall more efficiently than the BFS. However, the BFS consumed far more radicals away from the wall than that of the Five Row. The increased reduction in radicals would reduce the heat release due to secondary reactions for cooling configurations further downstream of the BFS.

**Table 0.6:** Wall Absorption Parameter

| Configuration | Wall Absorption (%) | |
|---|---|---|
| | $\phi$=1.3 M=1.0 | $\phi$=1.3 M=2.0 |
| **Five Row Cylindrical** | 12.86% | 4.27% |
| **Five Row Slot** | 11.53% | 2.97% |
| **Five Row Trench** | 12.18% | 3.66% |
| **Backwards Facing Step** | 16.44% | 5.27% |

## 4.5.2   Enhanced Mixing Schemes

### 4.5.2.1 Impact of Blowing Ratio on Augmentation

The results of a blowing ratio sweep are presented for the Enhanced Mixing

Schemes in Figure 4.47.  The flow was varied from an equivalent Five Row blowing ratio

of0.5 to 3.0 at a constant equivalence ratio of 1.3.  By maintaining the same overall mass

flow as the Five Row configuration, this allowed for comparison of configurations with

differing coolant exit areas like the Cross Flow configuration.  The blowing ratio sweep

data is presented at the 22 diameter downstream location. This location was arbitrarily

chosen as the variation of augmentation as a function of downstream distance is covered

later in this section.

The Roll Forward configuration and the Two Row Upstream configuration had

the highest augmentations.  This result was expected because these configurations

produced the high mixing with the lowest amount of low penetration rows of coolant.

149

The Roll Forward produced high mixing by injection coolant at angles where the flow penetrated deep into the flow and had little streamwise momentum.  The Two Row Upstream expelled two rows of coolant in the opposite direction of the freestream flow resulting in an even higher mixing rate.  The higher mixing resulted in higher heat release in the area near the injection holes.  Both these configurations showed decreasing augmentation with increasing blowing ratio until M = 1.5 where the trend reversed due presumably to separation of the coolant from the near wall region.  This indicates an optimal operating condition for additional heat release for these configurations.

The Cross Flow produced a lower augmentation than the Roll Forward and Two Row Upstream  but showed a similar trend of decreasing augmentation to a minimum value around M = 2.0  than increasing augmentation with further increases in blowing ratio.  The Swirler produced the lowest augmentation of the four Enhanced Mixing configurations..  This result is due to the Swirler orientating coolant toward downstream holes thus generating the least mixing of these configurations. Unlike the other three configurations, the Swirler showed decreasing augmentation with increasing blowing ratio for range of blowing ratios tested suggestive that the upstream rows were protecting the downstream rows from detaching.  Like the Five Row, the Swirler began to show a reduction in the decrease in augmentation with each increase in blowing ratio.
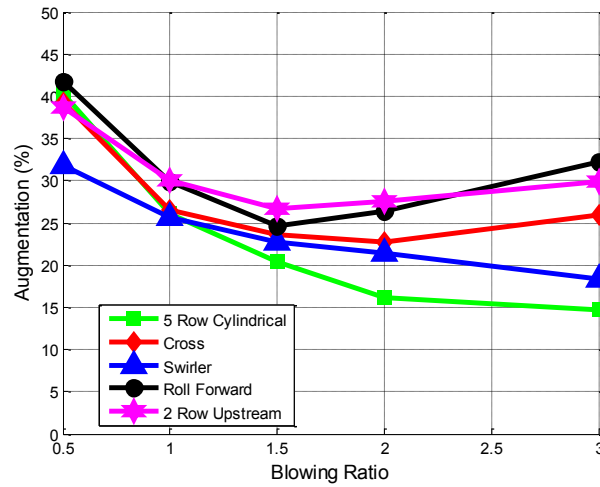
**Figure 0.51:** Augmentation vs. M, $\phi = 1.3$, $X/D = 22$

The variation of augmentation as a function of downstream distance is displayed in Figure 4.52. The augmentation presented is averaged augmentation at each downstream location at a $M = 2.0$ and $\phi = 1.3$. The Two Row Upstream showed a maximum augmentation at $X/D = 17$ then decreasing augmentation with downstream distance. The Roll Forward showed a similar trend with downstream distance except the peak occurred at $X/D = 22$. The Cross Flow also showed a maximum augmentation at $X/D = 17$ that then decreased and leveled off with downstream distance. The Swirler showed increasing augmentation with downstream distance similar to that of the Five Row but with increased augmentation at each downstream location. To explain these trends seen in augmentation with downstream distance an examination of the structure of the flames produces by each configuration is required.

151
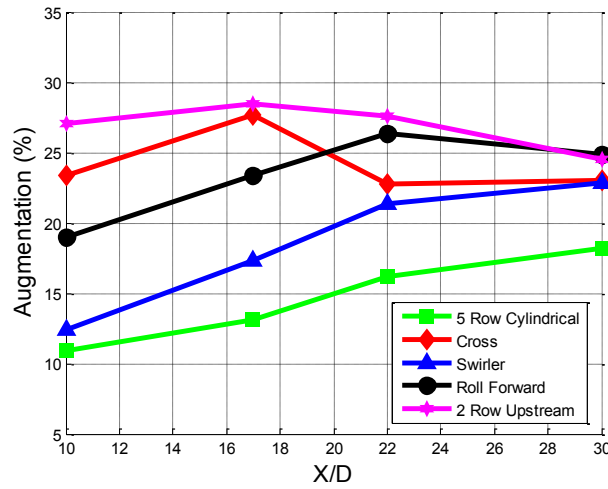
**Figure 0.52:** Augmentation vs. *X/D*, ϕ = 1.3, M = 2.0

### 4.5.2.2 Enhanced Mixing Schemes - Flame Images

This study examined the flame produced by the Enhanced Mixing configurations at a blowing ratio of two and at an equivalence ratio of 1.3 in order to explain the trends seen in augmentation. The flame images of the Enhanced Mixing configurations can be seen in Figure 4.53. Flame images were enhanced using the method described in Section 3.3.2. The flame lengths of each configuration are listed in Tables 4.7. The Two Row Upstream produced a very large region of intense flame from its start at the second to last row of cooling to the X/D = 22 location. This region of intense flame begins to dissipate and reduce in size around the X/D = 17 location which corresponds to the peak augmentation shown in Figure 4.47. The flame height and intensity continues to decrease with downstream distance indicating a decrease in heat release. The flame also becomes separated from the wall starting around the X/D = 22 location. The height of the flame

152

became smaller once it separated from the wall creating a region of non-reaction flow.
The separation of the flame and the reduction in flame height results in reduced heat flux
to the wall due to secondary reactions.  This confirms the trends shown in Figure 4.52.



**Figure 0.53:** Flame Visualization, $\phi$ = 1.3, M = 2.0, A-Five Row,  B-Two Row

Upstream, C-Roll Forward, D-Swirler, E – Cross Flow

The Roll Forward created a flame 125 diameters long that started at the second to
last row of cooling holes.  The initial row of normal holes and the second row of holes at
75˚ enhanced the mixing of the scheme causing the flame to start sooner.  The enhanced
mixing also caused the initial height of the flame to be large.  This large initial height

153

continues until the flame separates from the wall and begins to create a layer of non-reacting film underneath the still burning layer.  The region of intense flame above the 10 diameter to 30 diameter region is consistent with the high augmentation seen in Figure 4.47.  Around $X/D = 25$, the size of the intense flame section started to noticeably decrease.  This corresponds with the peak in augmentation seen in Figure 4.48. The Cross Flow produced the longest flame of all the configurations tested at 139 diameters.  The flame started with a region of intense flame near the wall in the region of $X/D = 10$ through $X/D = 22$.  This result matches the peak in augmentation seen at $X/D = 17$ in Figure 4.52.    The flame then continued to grow in height and eventually separated from the wall around $X/D = 40$ similar to that of the Five Row.

**Table 0.7:** Enhanced Mixing configurations, Flame Lengths

| Flame Length | Five Row | Two Row Upstream | Roll Forward | Swirler | Cross Flow |
|---|---|---|---|---|---|
| **M = 2, Phi - 1.3** | 136 | 116 | 125 | 66 | 139 |
| **M = 1, Phi - 1.3** | 106 | 90 | 94 | 50 | 72 |

The Swirler produced the smallest flame at a length of 66 diameters long that began around $X/D = 4$.  This late start is the reason for the low initial augmentation shown in Figure 4.48.  The intensity of the flame was high over the region of $X/D = 17$ to $X/D = 30$.  After this point the intensity decreased and the flame began separating from the wall. The high mixing of this scheme caused the oxygen to be consumed quickly over

154

the short distance.  However, due to the large height of the flame produced, much less of the heat released was absorbed by the wall.

### 4.5.2.3 Impact of Blowing Ratio on Heat Flux and Net Heat Flux Reduction

While the flame images and augmentation analysis give insight to the physics of each cooling configuration, these parameters do not directly tell how well a configuration cools the wall. In order to evaluate the effectiveness of a configuration to cool the wall, an analysis of heat flux and net heat flux reduction were performed.  Heat flux and NHFR results at $X/D = 22$ and a $\phi = 1.3$ for the blowing ratio sweep are presented in Figure 4.54 and 4.55. The results of nitrogen cooling are plotted as open symbols, air cooling as solid symbols, and no cooling as solid cyan diamonds.  The no cooling heat flux line was determined by supplying no coolant to the Five Row configuration.

For nitrogen cooling, all configurations showed reduced heat flux compared to the no cooling case across all blowing ratios.  This shows that with no secondary reactions each coolant configuration is effective at protecting the wall.  The Five Row, Roll Forward, and Cross Flow produced similar heat flux with nitrogen cooling.  The Five Row and Roll Forward reach a minimum heat flux around $M = 1.5$ and being increasing in heat flux with further increases in blowing ratio.  The Cross Flow's heat flux continued decreasing with further increases in blowing ratio. This is due to the larger coolant exit area in this scheme that caused the mass flow required for separation of coolant from the wall to be increased.

155

The Two Row Upstream showed the highest heat flux for both the nitrogen cooling and the air cooling cases across all blowing ratios. This configuration injected fluid counter to the flow at an angle that would not penetrate as far as a row of normal holes. This meant that a high rate of mixing was found near the wall. The high rate of mixing caused hot freestream gases to be mixed quickly with the coolant increasing the coolant temperature of the freestream air upstream of the remainder of the holes. The increase of the film temperature results in increased heat flux. Furthermore, for the air cooling case, the additional mixing causes reactions and high heat release directly adjacent to the wall. Both the air cooling and nitrogen cooling showed minimum heat flux values at $M = 1.5$ which matches the trend found in augmentation in Figure 4.52.

The Swirler configuration showed no variation of heat flux with blowing ratio for nitrogen cooling. This scheme created two counter rotating vortices that swept coolant towards the middle of the test plate. Therefore little changes were expected at high blowing ratio as there was already a large amount of coolant along the centerline. When the Swirler was supplied with air, the heat flux showed a slight decrease in heat flux with increases in blowing ratio. The large quantity of coolant buffered the reaction off the wall in the middle of the plate consistently for all blowing ratios. However, this scheme was unable to completely keep radicals, and thus reactions, from the wall. For all blowing ratios, the Swirler with air cooling failed to reduce the heat flux below that of the no cooling case. This resulted in negative NHFR across all the blowing ratios as seen in

156

Figure 4.551. This means that the Swirler fails to protect the wall when used in a fuel-rich environment.
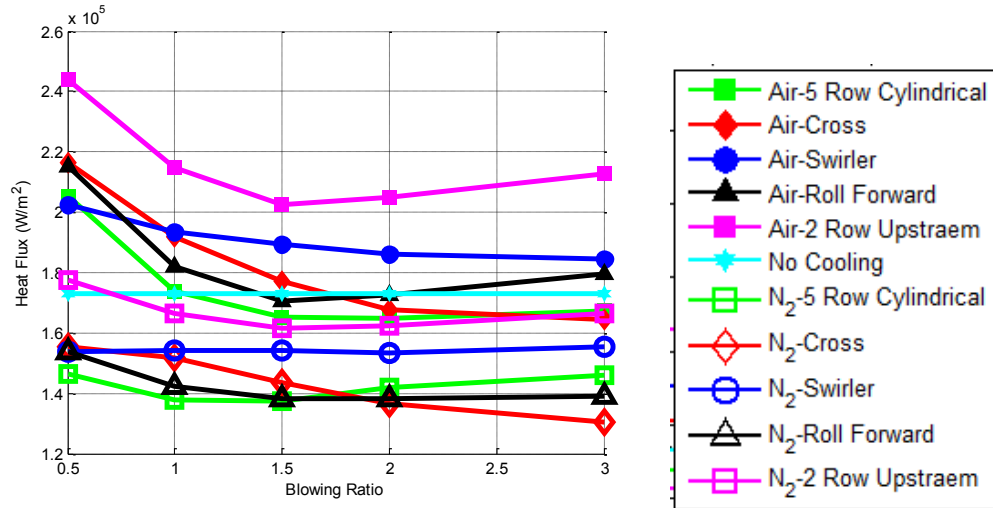


**Figure 0.54:** Heat Flux vs. M, Enhanced Mixing Schemes, $\phi = 1.3$, $X/D = 22$

The Two Row Upstream, Swirler, and Roll Forward configurations yielded negative NHFR for air cooling across all blowing ratios tested. This indicates that the local region around the instrumentation block would be better protected by no cooling than cooling with air for these configurations. These three configurations also showed a peak in NHFR around $M = 1.5$ and then decreasing NHFR with further increased blowing ratio. This indicates that more mass flow beyond $M = 1.5$ would only make the cooling performance worse. Each of these configurations also had very high difference in NHFR between air and nitrogen cooling that decreased to a minimum around $M = 1.5$ and increased with further increases in blowing ratio. This indicates that $M = 1.5$ was their optimal running condition. The poor performance of these configurations was expected

because they were designed to increase the mixing of the freestream and coolant. However, these configurations are meant to consume large numbers of radicals in the region near the cooling holes to reduce the potential heat release downstream.
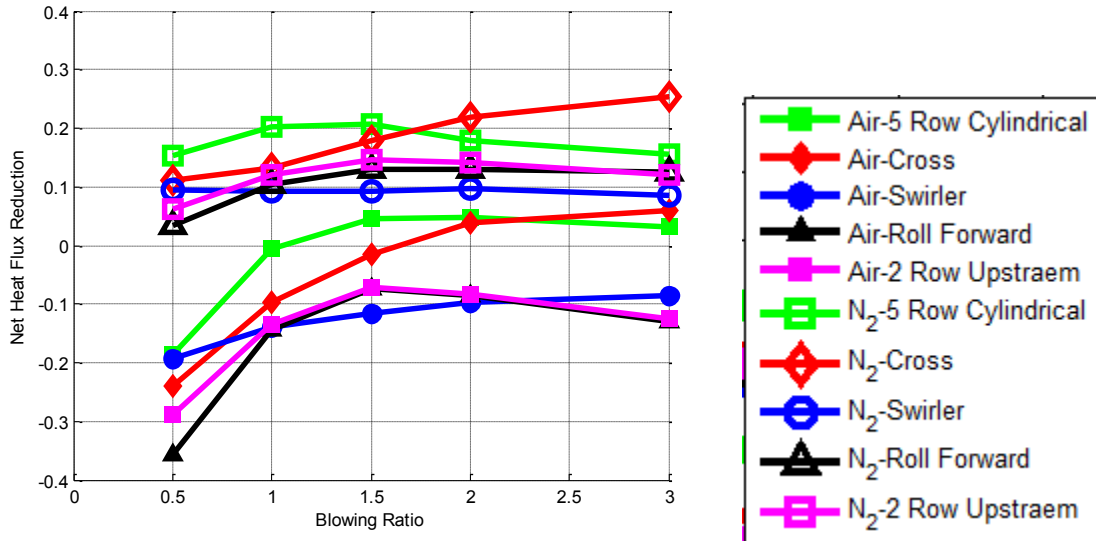


**Figure 0.55:** NHFR vs. M, Enhanced Mixing Schemes, $\phi = 1.3$, $X/D = 22$

### 4.5.2.4 Emissions

An emissions analysis was performed on each configuration and swept in the direction normal to the wall in increments of 2.5 mm. The emissions sampled the percent volume of $O_2$, CO, and $CO_2$ as described within Section 3.3.3. The results of each species are presented separately and are plotted against distance from the film cooled wall. Each species is also compared to their no cooling, freestream measurement counterparts. Figure 4.56 displays the emissions of CO, Figure 4.57 the emissions of CO2, and Figure 4.58 presents the emissions of O2 for the Wall Protection schemes.

The Swirler consumed the largest amount of CO of any configuration tested in this study. The Swirler varied from 5.9% CO at $Y/D = 18$ to 2.3% at $Y/D = 2$. The CO value at $Y/D = 18$ did not match the freestream value of 6.7% indicating that the Swirler affected the flow further out than 18 diameters. The high mixing caused by the two vortices penetrated deep into the flow and produced the desired result of increased radical consumption.

The Cross Flow configuration consumed an intermediate value of CO between that of the Five Row and the Swirler. The Cross Flow varied from 6.6 % CO at $Y/D = 18$ to 2.8% at $Y/D = 2$. The two mixing rows of the Cross Flow caused the increase in radical consumption while the five remaining rows of coolant minimized the effect of the additional heat release to the wall. This resulted in a higher CO consumption but similar heat flux results as the Five Row.

The Two Row Upstream consumed a similar overall amount of CO when compared to the Cross Flow. However, in the region of $Y/D = 10$ to $Y/D = 18$ the Two Row Upstream consumed more radicals than the Cross Flow. This region is between 25% and 50% of the 35D span away from the film cooled wall. Examining the flame image of the Two Row Upstream shows that the flame resides largely in this region for the majority of its length. This would result in a higher consumption of radicals in this region. Overall, the Two Row Upstream increased radical consumption over the Five Row as intended.

159
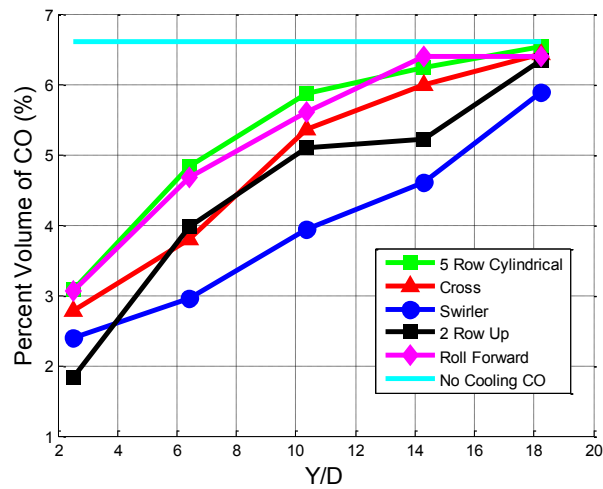
**Figure 0.56:** CO Emissions, $\phi = 1.3$, M = 2.0

The Roll Forward consumed similar amounts of CO as the Five Row

configuration. Instead of consuming more total radicals, the Roll Forward consumed

more radicals in the local area around the injection holes and created a shorter flame than

the Five Row.  The local heat release in the area of the instrumentation block was higher

for the Roll Forward because of the large number of radicals being consumed in this

location.  However, the overall impact of this additional heat release is limited to this

local area.  So even though the total amount of CO consumed far downstream is the same

between the Roll Forward and Five Row, the distribution of where the CO was consumed

is different.
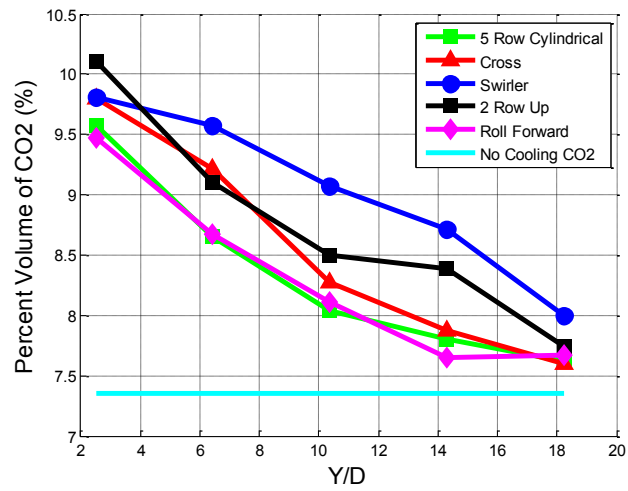
**Figure 0.57:** CO2 Emissions, $\phi = 1.3$, $M = 2.0$

The $CO_2$ emissions are complementary to the results of the CO emissions. As CO is consumed, $CO_2$ is produced in its place. The configurations that consumed the most CO produced the most $CO_2$.
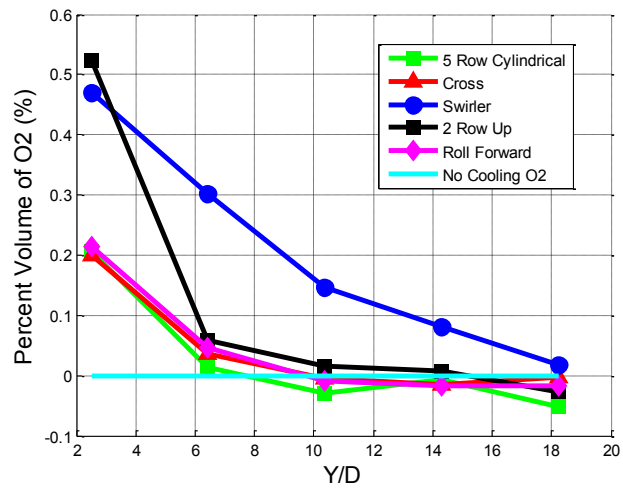


**Figure 0.58:** O2 Emissions, $\phi = 1.3$, $M = 2.0$

161

**4.5.2.5 Impact of Equivalence Ratio on Heat Flux and Augmentation**

The augmentation results of an equivalence ratio sweep are presented for the

Enhanced Mixing Schemes in Figure 4.59. The equivalence was varied from 1.1 to 1.3 at

a constant M = 2.0. The Φ sweep data is presented at the *X/D* = 22. The Enhanced

Mixing configurations showed nearly linear, positively sloped trends in augmentation as

a function of equivalence ratio. As expected the Five Row configuration produced much

lower augmentation than the Enhanced Mixing schemes. The Two Row Upstream

configuration produced the highest augmentation across all equivalence ratios at 10%

higher than the Five Row configuration. This was not surprising as this configuration

was expected to stagnate the incoming flow. The Cross Flow, Swirler, and Roll Forward

had similar augmentations that were approximately 5% higher than that of the Five Row

Configuration due to their enhanced mixing compared to the Five Row.
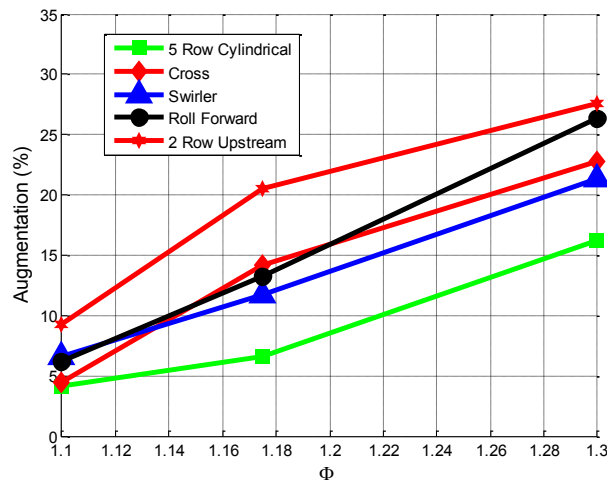


**Figure 0.59:** Augmentation vs. Φ, M = 2.0, *X/D* = 22

### 4.5.2.6 Wall Absorption Parameter

Determination of Wall Absorption allows for the examination of the overall effect of the heat release due to secondary reactions. However, to determine the overall effect, the heat flux underneath the entire flame length must be known. Because this information was unable to be acquired with this test rig, the WA parameter was calculated to examine the amount of potential heat entering the instrumentation block. Examining the percentage of the potential energy into the instrumentation block allows for evaluation of the local impact of secondary reactions on the film cooled wall. Table 4.8 displays the Wall Absorption parameter of the Enhanced Mixing configurations tested at a constant equivalence ratio of 1.3 and M = 1.0 and 2.0.

The Swirler showed slightly increased WA compared to the Five Row but the lowest WA of the Enhanced Mixing schemes. With the lowest overall impact on the wall and the highest radical consumption, the Swirler is an attractive scheme for consuming radicals. However, even with a low Wall Absorption, the Swirler still raises the temperature of the wall in the local region above that of the no cooled case making practical implementation of the Swirler more difficult.

The Two Row Upstream showed the largest improvement in Wall Absorption parameter between M = 1.0 to M = 2.0 from 18.52% to 8.81%. The increased mass flow allowed for higher penetration of the two upstream facing rows causing reactions to occur further from the wall. Because reactions are occurring further from the wall, less of the

163

heat released is transfer to the wall causing lower differential in heat flux between air and nitrogen and hence a lower WA even with a longer flame length.

The Cross Flow showed increased WA over the Five Row at both blowing ratios examined.  The increased mixing due to the two counter 45˚ spanwise rows caused the more heat to be released and thus a higher heat flux to the wall compared to the Five Row.  The Roll Forward resulted in a Wall Absorption parameter of 6.52% at M = 2.0. This result was center between all the other configurations tested. The Roll Forward failed to protect the wall compared to the Five Row and consumed a similar amount of radicals.  Instead of highly enhancing the mixing and causing a substantial increase in radical consumption, the Two Row Upstream consumed slightly more radicals while buffering the reactions away from the wall.  Because fewer rows of attached coolant are found in the Roll Forward scheme, the WA was higher compared to the Five Row.

**Table 0.8:** Wall Absorption Parameter

| Configuration | Wall Absorption (%) | |
|---|---|---|
| | $\phi$=1.3 M=1.0 | $\phi$=1.3 M=2.0 |
| **Five Row Cylindrical** | 12.86% | 4.27% |
| **2 Row Upstream** | 18.52% | 8.81% |
| **Roll Forward** | 13.77% | 6.52% |
| **Swirler** | 14.03% | 5.73% |
| **Cross Flow** | 15.39% | 6.65% |

### 4.5.2.7 Spanwise Variation of the Swirler Configuration

The IR images of the Swirler configuration for both nitrogen cooling and air cooling are shown in Figure 4.60.  Upon examination of the IR images of the Swirler configuration, an interesting trend was noticed.  In both images, lower wall temperatures can be seen the centerline of the cooling scheme at $Z/D = 0$ compared to the edges.  The Swirler configuration focused coolant towards $Z/D = 0$ and was expected to modify the shape of the flame.
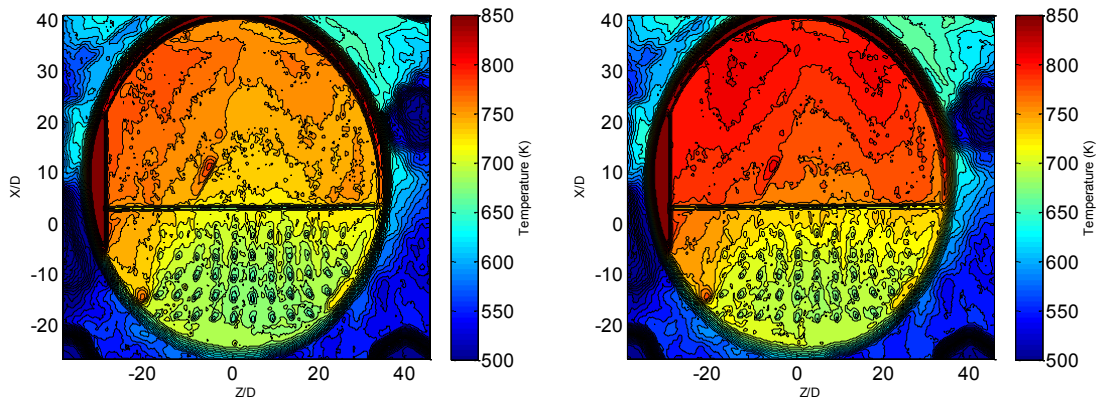


**Figure 0.60:** Swirler IR Image - Nitrogen Cooled (Left); Air Cooled (Right)

To examine the effects of the Swirler configuration on the downstream temperature distribution, spanwise variation of wall temperature was plotted at various downstream locations for both the Five Row and the Swirler configurations.  This comparison will show the difference between an evenly distributed scheme and the Swirler configuration.  Figure 4.61 shows the spanwise distribution for nitrogen cooling and Figure 4.62 shows the spanwise distribution for air cooling.

165
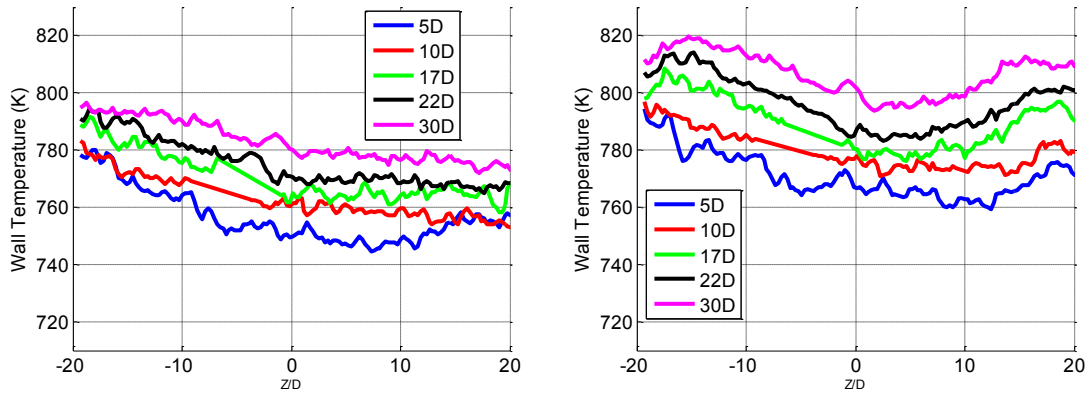
**Figure 0.61:** Spanwise Variation of Wall Temperature, Nitrogen Cooled;

Five Row (Left); Swirler (Right)

The Five Row configuration shows a decreasing wall temperature from left to right for both nitrogen and air cooling. This result matches the spanwise variation analysis performed in Section 4.2 and is expected. The Swirler on the other hand shows two peaks in wall temperature at $Z/D = $ -15 and $Z/D = 15$.
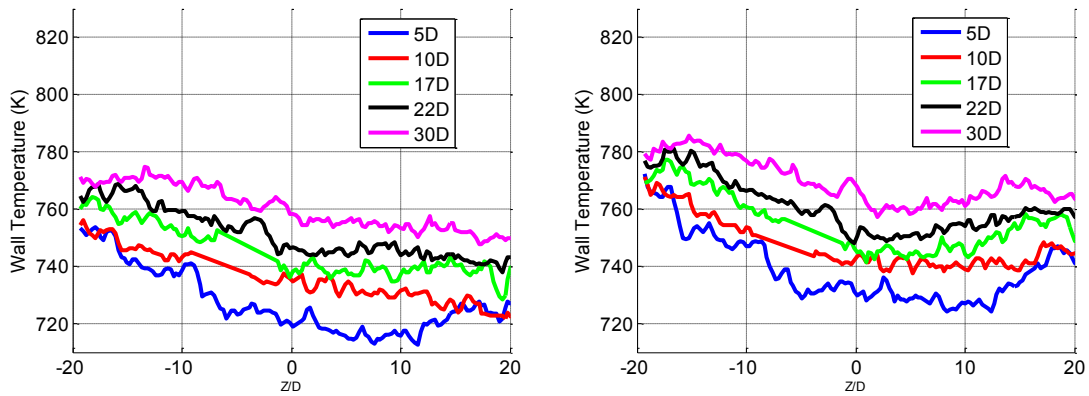


**Figure 0.62:** Spanwise Variation of Wall Temperature, Air Cooled; Five Row (Left);

Swirler (Right)

The additional cooling along the center of the Swirler lowers the wall temperature around $Z/D = 0$. This result is observed with and without secondary reactions. To continue comparison between the Five Row and the Swirler, the spanwise difference in temperature between air and nitrogen cooling was plotted at various downstream distances. The Five Row shows an even distribution across the width of the instrumentation block. The Five Row is meant to create an even distribution of coolant so this result is expected. The Swirler showed a different trend. At $Z/D = -20$, the Swirler showed a minimum in temperature. Wall temperature then levels outs between $Z/D = -10$ to $Z/D = 10$. For $Z/D > 10$, the wall temperature begins to increase once more. The reasoning for this trend is unknown but it indicates a modification of the distribution of coolant and secondary reactions for the Swirler configuration.
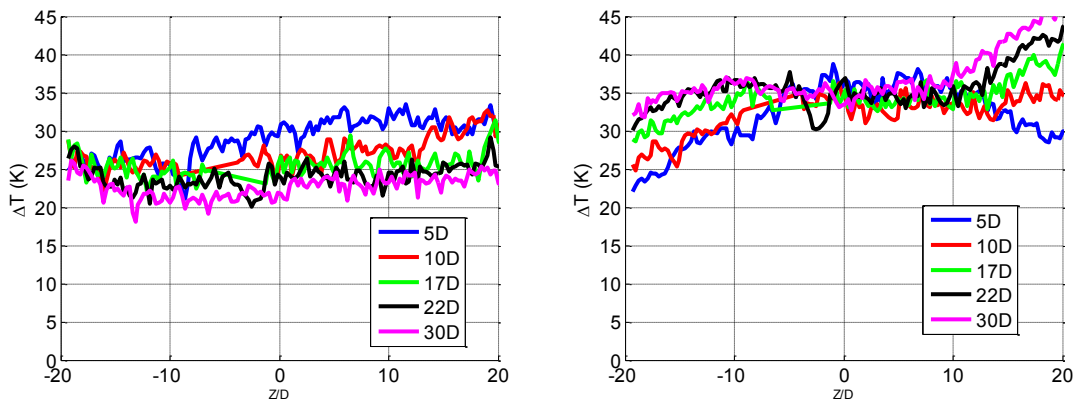


**Figure 0.63:** Spanwise Variation of Wall Temperature Difference; Five Row (Left); Swirler (Right)

167

# V. Conclusions and Recommendations

## 5.1    Overview

The first objective of this thesis was to confirm the results of the downstream effectiveness for a build-up of rows of coolant.  The second objective was the calibration and implementation of an infrared camera for use in creating a continuous measurement of wall temperature.  The final objective was to evaluate the downstream effectiveness of various film cooling hole configurations with the goal of creating a film cooling scheme to effectively operate in a fuel rich turbine environment.  To achieve the first goal, the Single Row, Three Row, and Five Row configurations were examined and compared with Robertson's results.  This study looked to determine the effects of a build-up of rows of coolant while searching for a viable method of protecting the wall.  To achieve the second goal, an IR window was installed and the wall temperature within the test rig was varied through the modification of backside cooling and film cooling techniques.  These variation of wall temperature where then compared to counts measured in the IR images and a calibration was formed allowing for conversion of voltage potential measured by the IR to wall temperature.  To achieve the final goal, two groups of cooling schemes were evaluated.  The first group, called the Wall Protection Configurations, aimed to create attached layers of coolant to protect the wall from increased heat release due to secondary reactions..  The second group, called the Enhanced Mixing Configurations, aimed to increase radical consumption so that cooling further downstream resulting in lower number of freestream radicals.

168

## 5.2    Major Findings

The row build-up test series found five rows of closely spaced injection holes to be adequate in minimizing heat flux to the wall in a fuel-rich environment.  The Five Row configuration reduced the heat flux to the wall below the no cooling case for 30 diameters downstream of injection.  However, by $X/D = 30$, the Five Row no longer protected the wall indicating that additional coolant must be applied to the flow to continue protecting the wall.

`    An IR camera was successfully implemented into the test rig.  The wall temperature was varied through various backside coolant temperature changes and through implementation of film cooling.  The result was a calibration for the IR camera converting voltage potential to wall temperature.  This result allows for continuous measurement of wall temperature within the IR cameras field of view.

The Wall Protection schemes showed that a Five Row Slot configuration could most effectively reduce the heat flux and wall temperature of the film-cooled wall most effectively.  The slot geometry is unfeasible for use within a turbine environment. To attempt to simulate the effects of the slot, a Five Row Trench scheme was created which showed slightly reduced downstream effectiveness compared to the Five Row Slot but greater performance than that of the Five Row configuration.  Because of these results and the ease of construction, the Five Row Trench is recommended for use to protect the wall in a fuel-rich turbine environment.

169

Of the Enhanced Mixing schemes, the Swirler consumed the highest amount of radicals while only producing slightly increased heat flux compared to the no cooling case. Implementation of this configuration would require increased internal cooling to maintain the temperature of the component below its critical value. The flame produced by the Swirler was also the shortest indicating a quick consumption of radicals which would be useful within a turbine environment.

## 5.3 Future Research

A new film cooling rig is in the process of being constructed. The details of this new rig are described in Appendix A. This new rig will examine the effects of curvature and Mach number on the downstream effectiveness of various cooling configurations. Also the new rig will have an internal cooling scheme similar to that of a turbine blade. Future researches should install thermocouples within the internal cooling passage to measure the internal coolant temperature as well as the backside temperature of the film cooled wall. This combination along with the implementation of an IR camera calibrated by a few wall temperature measurements will allow for the measurement of non-dimensional wall temperature. Future researchers should look to compare the overall effectiveness of various cooling schemes between low freestream temperature experiments and engine like freestream temperature experiments. This comparison would allow for the determination of the validity of scaling cold freestream film cooling experiments to engine like conditions.

170

Future researchers could improve upon the method used to hold the IR window in place. The current experiment experienced cracking of the IR window. These cracks did not affect the IR measurement but it removed sections of the data from potential use.. Also while Bohan [3] showed reactions occurring in the region around 25D downstream of injection, this thesis showed for various configurations with five rows of cooling holes, reactions continue as far downstream as 140D. Future researchers should implement heat flux measurements close to injection as well as some as far as 150D to see the overall effect of secondary reactions on cooling performance.

**Appendix A – New Test Rig**

A second test rig was designed and is being constructed at AFIT.  The test rig was designed to achieve a fuel-rich freestream coupled with a typical film cooling flow to enable the study of secondary reactions along a combustor liner or within a turbine. The rig accommodated a larger cooling insert then previous investigations enabling for modeling of curvature and internal cooling schemes similar to those experienced in a turbine.  Furthermore, this rig focused on the capability to take heat flux measurements along the surface of the cooling insert through the use of imbedded thermocouples and IR imagery.  These measurements coupled with visible spectrum imagery of the reactions above the wall provided for a more detailed understanding of the reaction front and the heat release to the wall over a range of equivalence ratios and blowing ratios.  This appendix will discuss the major features and objectives of the test rig.  This will include discussion of the supply and flow path of hot fully combusted gases, the various instrumentation and optical access features, and the internal film cooling assembly.

**A.1    New Experimental Rig**

The flow path of the new testing rig is shown in Figure A.1.  To simulate turbine entry conditions, the test rig was supplied with a controlled equivalence ratio of reacted fuel-to-air mixture supplied from a Well Stirred Reactor identical to the one discussed in Section 3.1.  The flow exits the top of the WSR and proceeds into the straightener and transition section.  The flow straightener removes the swirl from the flow due to the WSR and the transition section transitions the geometry from the circular area of the WSR to

172

the rectangular geometry at the inlet of the testing rig.  The flow straightener and

transition section are made of the same materials described in Section 3.2.
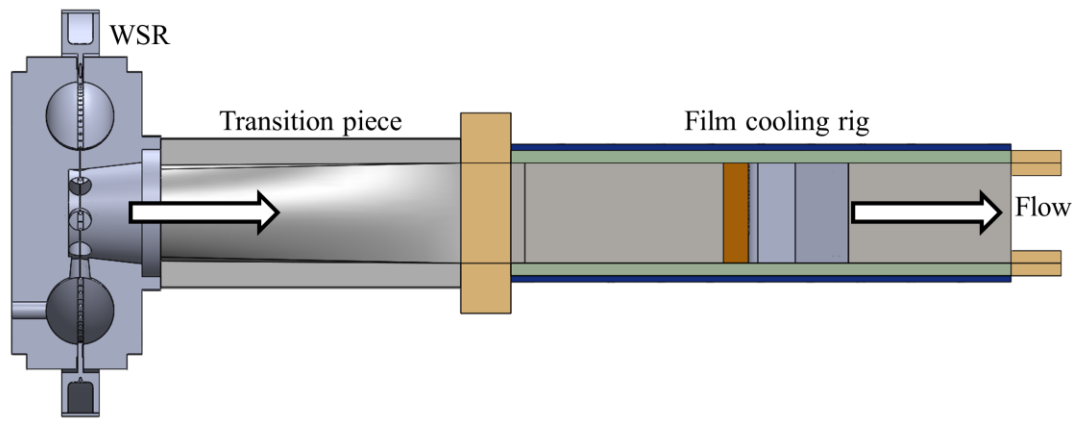


**Figure A.1:** Test Rig Flow Path

Proceeding downstream from the transition section, the flow entered the test rig.

The test is shown in Figure A.2. The walls that formed the flow area of the test section

were made up of two quartz side windows, the main Hastelloy-X cooling block, and the

moveable Hastelloy-X front block.  The two quartz side windows allow for optical access

across the entire downstream distance of the testing rig.  The main Hastelloy-X block

contained the interchangeable film cooling insert and was machined with a step designed

to trip the flow to ensure turbulence within the test section.  The step height was 7.01 mm

and was designed to ensure the flow was fully transitioned to turbulent flow before

reaching the cooling insert. The main block also contained cooling channels that were

designed similarly to the ones discussed in Section 3.2.  These cooling channels can be

supplied with nitrogen, water, or Mokon oil cooling to control the temperature of the wall.
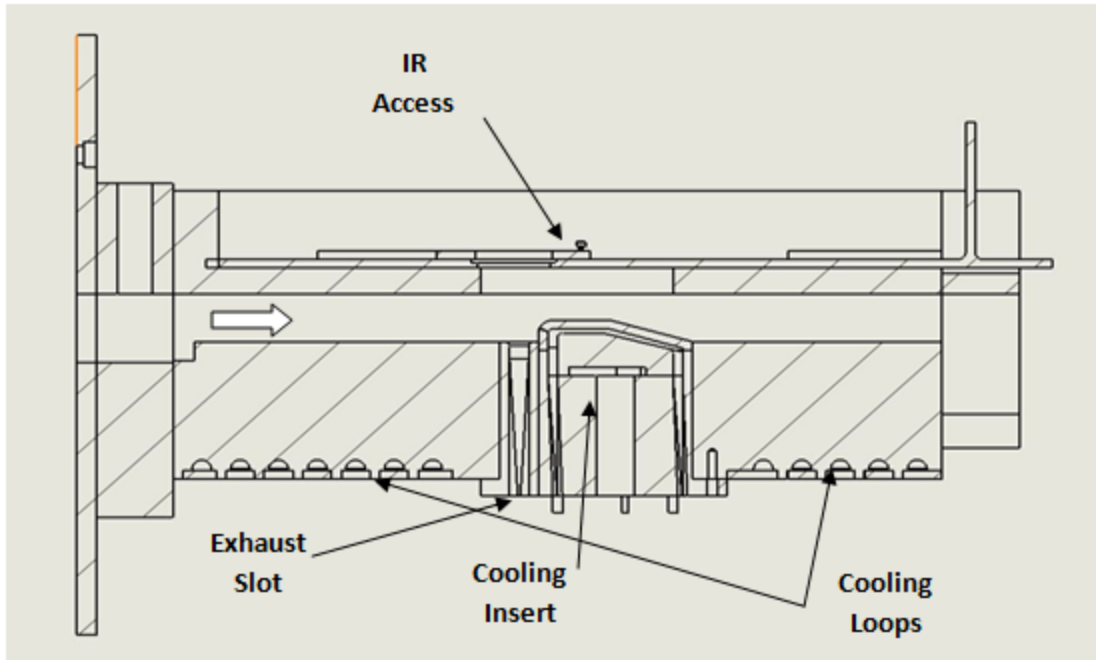


**Figure A.2:** Test Rig Side View

The front view of the test rig is shown in Figure A.3 and the front block is shown in red. The front block of the test rig served two major purposes. The first was to allow visual access normal to the film cooling insert in the main block. To enable this, the main block was designed to secure a IR window with a field-of-view that ranged from slightly upstream of the film cooling block to the end of the film cooling block. The second purpose was to enable variation of the Mach number. The plates that held the main block and the front block together were designed to have multiple screw holes to secure the front plate in place. This allowed for variation of the distance between the

174

front and main blocks from 0.7 inches to 0.25 inches and thus a Mach number change

from 0.1 to approximately 0.4.
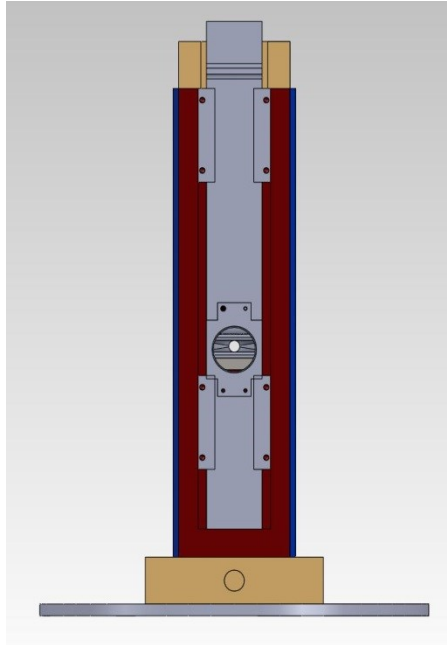


**Figure A.3:** Test Rig Front View

## A.2    Internal Cooling Scheme Insert

The internal cooling scheme insert is a combination of two modular cooling plates

and a universal air supply and exhaust.  The two modular cooling plates can be shaped to

model both flat plate configurations as well as various curvatures like Figure A.4.  The

two cooling plates form the two surfaces of an internal cooling scheme.  The internal

cooling area can be controlled by varying either of the cooling plates.  The flow rate

through the internal channel is controlled via two mass flow controllers on the inlet and

175

outlet of the internal cooling channel.  Control of the internal flow rate allows for matching of the internal convective heat transfer coefficient, $h_i$, with values seen in typical turbine blades.  By controlling the exit mass flow, the flow through the film cooling holes can be controlled to match blowing ratio or momentum ratio.  The coolant entering the inlet of the cooling scheme has a heater upstream allowing for a range of density ratios to be tested.

Thermocouples embedded into the wall will allow for measurement of the wall temperature and enable calibration of an IR camera.  Thermocouples within the internal cooling schemes allow for measurement of the internal coolant temperature, $T_{c,i}$.  By knowing the wall temperature, internal coolant temperature, and the freestream temperature, the non-dimensional wall temperature can be calculated (Equation 2.7). This parameter is widely used in film cooling literature and would allow for comparison to low temperature experiments to evaluate the scaling of various parameters between hot and cold experiments.
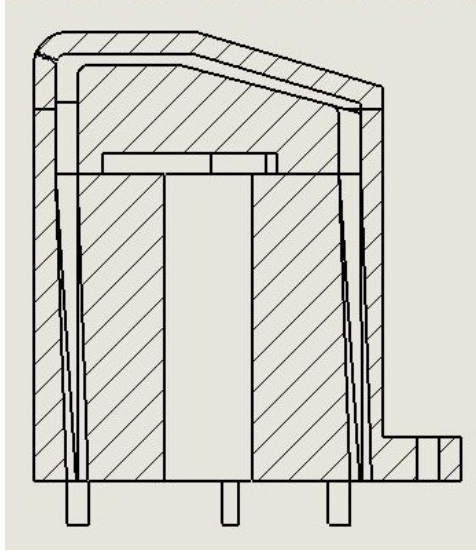
**Figure A.4:** Cooling Insert Cross-section

For the cooling scheme shown in Figure A.4 it is important to setup flow

conditions properly.   In Figure A.2, the cooling configuration sticks out a quarter of the

channel height into the flow and is meant to model only half of a turbine blade.  Because

the other half of the curvature is not there, the stagnation point will not be setup properly.

In order to model where the stagnation point will naturally occur with this curvature, a

slot was placed upstream of the cooling configuration.  The goal of this slot is to pull a

section of the flow out so that the stagnation region occurs at the proper location of the

leading edge of the cooling configuration.  The mass flow rate through the slot is

controlled with a mass flow controller far downstream of the slot.  Controlling how much

mass flow is taken out of the flow will allow for control of the stagnation region.

<center>**Appendix B – IR Camera Setup**</center>

The purpose of this appendix is to provide an overview of the operation of the FLIR SC6700 IR camera. The start-up procedure, various camera control features, and recording options for the SC6700 IR camera will be discussed in detail.

**B.1    Start-up**

The software that controls and collects data for the IR camera is ExaminIR. A copy of this program is provided on a CD within the carrying case of the FLIR SC6700 IR camera. The CD provided also contains the drivers for the 1 gigabit Ethernet cable used with the IR camera. Before opening ExaminIR, ensure the Ethernet cable is connected between the IR camera and the computer and ensure the power cable is plugged into the IR camera. Turn the IR camera on with the button labeled "POWER" on the back of the IR camera seen in Figure B.1. Wait until the three lights labeled "POWER", "Ready", and "COLD" light up green on the backside of the IR camera.



<center>**Figure B.1:** IR Camera Ports and Ready Lights</center>

<center>178</center>

After ensuring the IR camera is fully powered on, plug in the ExaminIR Pro Thumb Drive, seen in Figure B.2, into any USB drive on the computer the IR camera is plugged into. This thumb drive unlocks the Pro version of the ExaminIR software which contains many more control options for the IR camera.



**Figure B.2:** ExaminIR Pro Thumb Drive

To connect to the camera, open ExaminIR and click the camera option in the top left next to the edit option. A drop down menu will appear and click the connect option. Once done, a menu similar to the one shown in Figure B.3 will appear. If setup properly, the IR camera should appear on the left. If it does not appear hit the search tab at the bottom left corner of the menu. Once the IR camera appears, click the IR camera and hit connect in the bottom right corner of the menu. Once the camera is connected, a live feed should appear on the main screen of ExaminIR. In the top right of this main screen a drop down menu can be found that can change what measurement is being displayed. The drop down menu can change between built-in temperature conversions and raw counts.
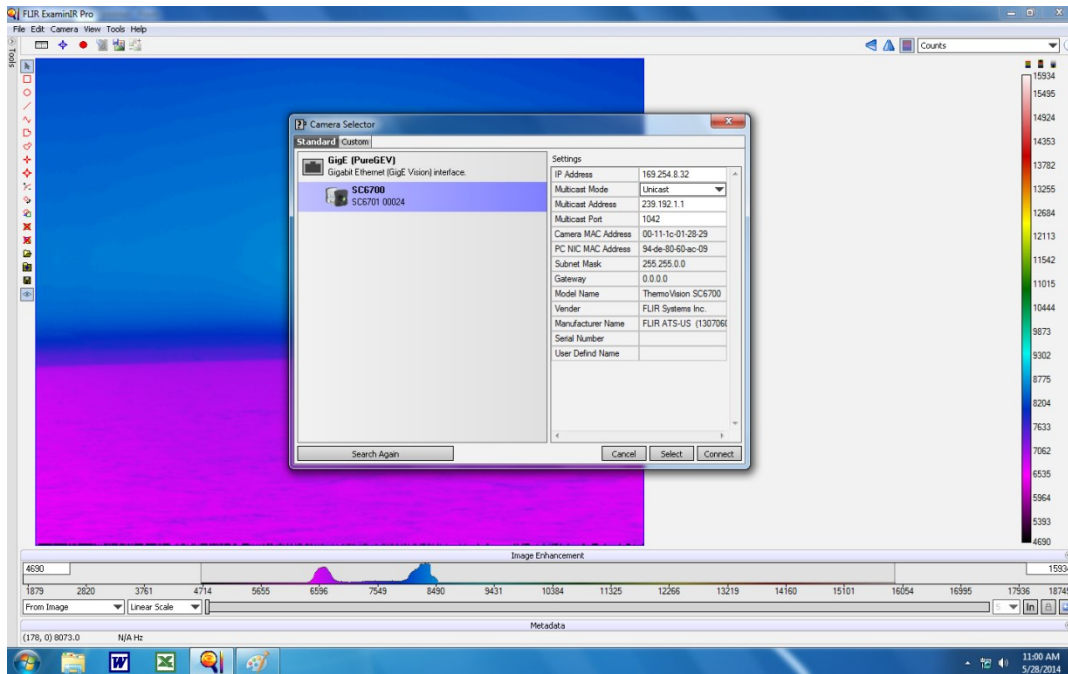
**Figure B.3:** Camera Connection Menu

## B.2    Camera Control

With the camera connected to the computer, the next step is to configure the

cameras settings.  On the main ExaminIR screen, hit the camera tab in the top left and a

drop down menu appears.  Hit "control" on the drop down and a menu will appear.  Hit

the tab labeled "Setup" and the menu should appear similar to Figure B.4.  If the menu is

different, hit the "Tools" option at the top left and change the user mode from "basic" to

"advanced".  On the initial setup tab there are various options for integration time and

frames per second.  Built-in integral times for the various filters installed in the camera

are found in the drop down menus and each time has a corresponding temperature range.

Selecting a built-in integration time will automatically switch the filter to the option

180

selected. For testing within this thesis, the Flame Filter was selected for the range of temperature from 700 C to 1200 C and the frames per second were set to 60.



**Figure B.4:** Camera Control Menu

Hitting the "Filter/Flag" tab will open up the menu shown in Figure B.5. This menu allows for the the filter in use to be changed and to view the four stowed filters. If a new filter is installed, an option labeled "Scan" will allow the IR camera to register and update the filter list. The drop down menu labeled "Current" shows the current filter and selecting any filter from the drop down menu will switch the current filter to the one selected.

181

**Figure B.5:** Filter Selection Menu

Opening the tab labeled "Window" allows for modification of the resolution and screen offset for the IR camera. The width and height menus control the cameras resolution and must be in standard resolution scales. The "X Offset" and "Y Offset" control the location of the viewing area of the IR camera. The location (0,0) for the offsets is located in the center of the image.



**Figure B.6:** Window Sizing Menu

**B.3     Recording Data**

Various data recording options are available in ExaminIR.  In the top left of the main screen where the IR image is presented, a red circle should appear beneath the "view" option.  Hover the mouse of this red circle and select the recording settings.  This should open up a menu similar to Figure B.7.  In this menu, the recording options for both images and videos are displayed.  The length of recording, file saving location, and file name are just a few of the options available here.  After setting this tab up, hit "Ok" at the bottom right.  Now to record data, hover over the same tab that open the recording setting and hit either record image or record video.
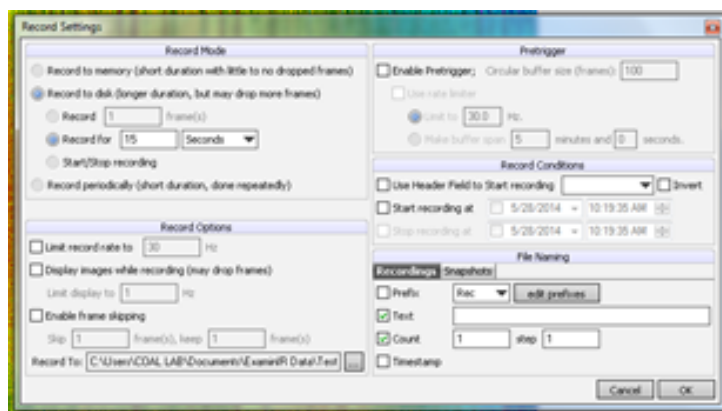


**Figure B.7:** Recording Settings Menu

## Bibliography

[1]     Bogard, D.G. and K. A. Thole. "Gas Turbine Film Cooling." *Journal of Propulsion and Power* (March-April 2006): 22(2).

[2]     Ballal, Dilip R and Joseph Zelina. "Progress in Aeroengine Technology (1939-2003)." *Journal of aircraft* (2004): 41(1):43-50.

[3]     Bohan, Brian. T., Polanka, Marc D. "Analysis of Flow Migration in an Ultra-Compact Combustor." ASME Turbo Expo 2011. Vancouver, 2011.

[4]     Kirk, D.R., G.R. Guenette, S.P. Lukachko, and I.A. Waitz. "Gas Turbine Engine Durability Impacts of High Fuel-Air Ratio Combustors Part 2: Near Wall Reaction Effects on Film-Cooled Heat Transfer." *GT-2002-30182* ASME Turbo Expo 2002: Land, Sea, & Air. Amsterdam, The Netherlands, 2002.

[5]     Lukachko, S., Kirk, D., and Waitz, I. "Gas Turbine Enginge Durability Impacts of high Fuel-Air Ratio Combustors-Part I: Potential for Secondary Combustion of Partially reacted Fuel." *Journal of Engineering for Gas Turbines and Power* (2003): 742-750.

[6]     DeLallo, M.R., Polanka, M.D., and Blunck, D.L. "Impact of Trench and Ramp Film Cooling Designs to Reduce Heat Release Effects in a Reacting Flow." *GT-2012-68311*. Copenhagen, Denmark, ASME Turbo Expo, 2012.

[7]     Bergman, T.L., A.S. Lavine, F.P. Incropera, and D.P. DeWitt. *Fundamentals of Heat and Mass Transfer*. n.d.

[8]     Balduaf, S., Schulz, A., and Wittig, S. "High-Resolution Measurements of Local Effectiveness From Discrete Hole Film Cooling." *Journal of Turbomachinery* 123 (2001): 758-765.

[9]     Oguntade, H.I. Andrews, G.E., Burns, A.D., Inham, D.B., and Pourkashanian, M. "Conjugate Heat Transfer Predictions of Effusion Cooling: The Influence of the Coolant Jet-flow Direction on the Cooling Effectiveness." *GT2012-68517*. Copenhagen Denmark, ASME Turbo Expo, 2012.

[10]     Saumweber, C., Schulz, A., and Wittig, S. "Free-Stream Turbulence Effects on Film Cooling With Shaped Holes." *Journal of Turbomachinery* 125 (1993): 65-73.

[11]     Hartnett, J. P., Birkebak, R. C., and Eckert, E. R. G. "Velocity Distributions, Temperature Distributions, Effectiveness and Heat Transfer for Air Injected Through a Tangential Slot into a Turbulent Boundary Layer." *Journal of Heat Transfer* (1961): 293-306.

[12]     Bunker, R. S. "Film Cooling Effectiveness Due to Discrete Holes Within a Transverse Surface Slot." *Proceedings of 2002 International Gas Turbine Conference and Exposition*. Amsterdam, 2002.

[13]     Mellor, A.M., D.W. Bahr, W.S. Derr, K. Depooter, W.J. Dodds, H.E. Eickhoff, L. Gardner, D.C. Hammond, J.E. Peters, R.B. Whyte, and G. Winterfield. "Design of Modern Turbine Combustors." San Diego, CA: Academic Press Inc., 1990.

[14]     Mongia, H.C. "A Synopsis of Gas Turbine Combustor Design Methodology Evolution of Last 25 Years." *ISABE, AIAA*. Cincinnati, Ohio, 2001.

[15]     Andrews, G.E., Asere,A.A., Gupta,M.L., and Mkpadi, M.C. "Effusion cooling: the influence of number of holes." *Journal of Power and Energy* (1990): 204.

[16]     Kakade, V.U., S.J. Thorpe, and M. Gerendas. "Effusion-Cooling Performance at Gas Turbine Combustor Representative Flow Conditions." *GT2012-68115 in ASME Turbo Expo.* Copenhagen, Denmark, June 2012.

[17]     Turns. *An Introduction to Combustion: Concepts and Applications*. McGraw-Hill Education, 2000.

[18]     Zelina, J., Sturgess, G. J., Shouse, D. T. "The Behavior of an Ultra-Compact Combustor (UCC) Based on Centrifugally-Enhanced Turbulent Burning Rates." 2004.

[19]     Bohan, Brian T., CPT USAF. *Analysis of Flow Migration in an Ultra-Compact Combustor*. Master Thesis. Air Force Institute of Technology. WPAFB, 2011.

[20]     Anderson, W., M.D. Polanka, J. Zelina, D. Evans, S.D. Stouffer, and G.R. Justinger. "Effects of a Reacting Cross-Stream on Turbine Film Cooling." *Journal of Engineering for Gas Turbines and Power* (May 2010): 132.

[21]     Lin, Cheng-Xian, Richard J Holder, Balu Sekar, Joseph Zelina, Marc D. Polanka, Hugh J. Thornberg, and Alejandro M. Briones.  "Heat Release in Turbine Cooling II: Numberical Details of Secondary Combustion Surrounding Shaped Holes". *Journal of Propulsion and Power*, 27(2):269-281, 2011.

[22]     DeLallo, M.R.  *Impact of Trench and Ramp Film Cooling Designs to Reduce Heat Release Effects in a Reacting Flow*, Master Thesis. Air Force Institute of Technology. WPAFB, 2011.

[23]     Robertson, Jacob J., CPT USAF. *Film Cooling in Fuel Rich Environments.* Master Thesis. Air Force Institute of Technology. WPAFC, 2013

[24]     Nenniger, J. E., Kridiotis, A., Chomiak, K., Longwell, J., P., and Sarofim, A. F. "Characterization of Toroidal Well Stirred Reactor." *Twentieth Symposium (International) on Combustion*. Combustion Institute, 1984. 473-479.

[25]     Stouffer, S., Pawlik, R., Justinger, G., Heyne, L., Zelina, J., and Ballal, D. "Combustion Performance and Emissions Characteristics for a Well-Stirred Reactor for Low Volatility Hydrocarbon Fuels." *AIAA Paper No. 2007-5663*. 2007.

[26]     Greiner, N.J., Polanka, M.D., Robertson, J.R., and Rutledge, J.L. "Effect of Variable Properties Within a Reacting Boundary Layer with Film Cooling." *Accepted to ASME Journal of Engineering for Gas Turbines and Power* (n.d.).

[27]     W. R. Wade, "Measurement of Total Hemispherical Emissivity of Several Stably Oxidized Metals and Some Refractory Oxide Coatings," National Aeronautics and Space Administration, NASA Memo 1-20-59L, January 1959.

[28]     Milanes, David W., Daniel R. Kirk, Krzysztof J. Fidkowski, and Ian A. Waitz. "Gas Turbine Engine Durability Impacts of High Fuel-Air Ratio Combustors: Near wall Reaction Effects of Film-Cooled Backward Facing Step Heat Transfer". *Proceedings of ASME Turbo Expo*, GT-2004-53259, 2004.

[29]     Evans, D.S. *The Impact of Heat Release in Turbine Film Cooling.* Unpublished, Air Force Institute of Technology, 2008.

| 1. REPORT DATE (DD-MM-YYYY) | 2. REPORT TYPE | 3. DATES COVERED (From – To) |
|---|---|---|
| 02-06-2014 | Master's Thesis | Jan 2013 – June 2014 |

| TITLE AND SUBTITLE | 5a. CONTRACT NUMBER |
|---|---|
| Minimization of the Effects of Secondary Reactions on Turbine Film Cooling in a Fuel Rich Environment | 5b. GRANT NUMBER |
| | 5c. PROGRAM ELEMENT NUMBER |

| 6. AUTHOR(S) | 5d. PROJECT NUMBER |
|---|---|
| Andrew T. Shewhart | 5e. TASK NUMBER |
| | 5f. WORK UNIT NUMBER |

| 7. PERFORMING ORGANIZATION NAMES(S) AND ADDRESS(S) | 8. PERFORMING ORGANIZATION REPORT NUMBER |
|---|---|
| Air Force Institute of Technology Graduate School of Engineering and Management (AFIT/ENY) 2950 Hobson Way, Building 640 WPAFB OH 45433-8865 | AFIT-ENY-14-J-37 |

| 9. SPONSORING/MONITORING AGENCY NAME(S) AND ADDRESS(ES) | 10. SPONSOR/MONITOR'S ACRONYM(S) |
|---|---|
| Air Force Research Laboratory 1790 Loop Road Building 490 WPAFB,OH 45433 Dr. Scott Stouffer | AFRL |
| | 11. SPONSOR/MONITOR'S REPORT NUMBER(S) |

**12. DISTRIBUTION/AVAILABILITY STATEMENT**
 DISTRUBTION STATEMENT A. APPROVED FOR PUBLIC RELEASE; DISTRIBUTION UNLIMITED.

**13. SUPPLEMENTARY NOTES**
This material is declared a work of the U.S. Government and is not subject to copyright protection in the United States.

**14. ABSTRACT**

The demand for increased thrust, higher engine efficiency, and reduced fuel consumption has increased the turbine inlet temperature and pressure in modern gas turbine engines. The outcome of these higher temperatures and pressures is the potential for unconsumed radical species to enter the turbine. Because modern cooling schemes for turbine blades involve injecting cool, oxygen rich air adjacent to the surface, the potential for reaction with radicals in the mainstream flow and augmented heat transfer to the blade arises. This study evaluated various configurations of multiple cylindrical rows of cooling holes in terms of both heat release and effective downstream cooling. It confirmed that a build-up of rows of coolant could be used to effectively protect the wall in a fuel-rich environment. It demonstrated slot and trench configurations to be effective in reducing the heat flux to the wall. Also, the Swirler and Two Row Upstream configurations were shown to highly increase radical consumption. Finally, this research developed infrared imaging as a technique for evaluating the wall temperature of the film cooled surface.

**15. SUBJECT TERMS**
 Ultra Compact Combustor, Combustion, Film Cooling

| 16. SECURITY CLASSIFICATION OF: | | | 17. LIMITATION OF ABSTRACT | 18. NUMBER OF PAGES | 19a. NAME OF RESPONSIBLE PERSON Dr. Marc D. Polanka, AFIT/ENY |
|---|---|---|---|---|---|
| a. REPORT | b. ABSTRACT | c. THIS PAGE | | | 19b. TELEPHONE NUMBER (Include area code) |
| U | U | U | UU | 208 | (937) 255-6565, 4714 |